Title
Constraining the Recent Star Formation History of the Galactic Center with High Precision Astrometry

Author
Yelda, Sylvana

Publication Date
2012

Peer reviewed|Thesis/dissertation

University of California

Los Angeles

Constraining the Recent Star Formation History of the Galactic Center with High Precision Astrometry

A dissertation submitted in partial satisfaction

of the requirements for the degree

Doctor of Philosophy in Astronomy

by

Sylvana Yelda

2012

Abstract of the Dissertation

Constraining the Recent Star Formation History of the Galactic Center with High Precision Astrometry

by

Sylvana Yelda

Doctor of Philosophy in Astronomy

University of California, Los Angeles, 2012

Professor Andrea M. Ghez, Chair

The proximity of the Galactic center has allowed for the detailed study of the environs of a supermassive black hole (SMBH). While the region is inhabited predominantly by old, late-type giants, there exists a population of $\sim$200 young (6 ± 2 Myr), massive (10-100 $M_\odot$) stars within the central parsec. Their presence here is puzzling since the standard mode of star formation cannot proceed in the face of the strong tidal forces from the SMBH. Given their youth, the dynamics of these stars can be used to understand their origin and lend insight into star formation processes in the hostile environment surrounding a supermassive black hole. In this thesis, I use high resolution infrared imaging from the W. M. Keck telescopes in order to determine precise orbital parameter estimates of the young stars and understand the Galactic center's most recent epoch of star formation.

First, we present a new optical distortion model for the Keck/NIRC2 narrow camera that is based upon on-sky measurements of a globular cluster. With an improved distortion model, we show that a stable astrometric reference frame for the GC can be established with Sgr A* at rest to within 0.09 mas yr^{-1} (3.4

km s^{-1} at a distance of 8 kpc), thereby improving the stability of the reference frame. Accurate proper motions of the central stellar cluster are presented and the stars are shown to have significant net rotation parallel to Galactic rotation. These stars can be used as astrometric standards for defining a reference frame without requiring the assumption of no net motion of the central stellar cluster, as has been done in earlier proper motion studies.

Second, we use high-precision astrometry, measured in the newly constructed reference frame, and radial velocities of ∼115 young stars at projected radii between $R = 0\farcs8$ - $13\farcs3$ in order to estimate their orbital properties. This constitutes the largest sample of stars used for this type of study to date. The median proper motion uncertainty for the stars within $R \sim 6''$, for which we have up to a 16-year baseline of measurements, is 0.03 mas yr^{-1} (∼1.2 km s^{-1}). Acceleration uncertainties are typically 10 μas yr^{-2} (∼0.4 km s^{-1} yr^{-1}), which has allowed for the detection of six significant accelerations in the plane of the sky outside the central arcsecond. Such measurements provide direct calculations of the line of sight distance and therefore precise orbital parameter estimates. We detect the clockwise stellar disk reported in previous studies, but find that the fraction of young stars within the disk is much smaller than once thought. We do not find evidence for the previously-claimed counter-rotating disk. The clockwise disk has an inclination of ∼130° and an angle to the ascending node of ∼96°, with an opening angle of 15.2°. The orientation of the disk plane does not change with radius, contrary to recent claims of a highly-warped disk. We identify a bias in the orbital solutions of disk stars near the line of nodes that stems from a previously adopted line-of-sight distance prior and show that this bias leads to an apparently-warped disk. The candidate disk members have orbital eccentricities of $e \sim 0.3$. This can be explained by dynamical relaxation in an initially circular disk with a moderately top-heavy mass function ($\Gamma \sim 1.6$), consistent with

the latest estimates of the young star population's IMF. This cannot, however, account for the high inclinations of the out-of-disk population, which makes up at least half of the central parsec's young stars. Thus, if all of the young stars formed in a single disk, an additional dynamical mechanism must be invoked to explain their orbits.

The dissertation of Sylvana Yelda is approved.

David Jewitt

Jonathan L. Mitchell

Brad M. S. Hansen

Mark R. Morris

Andrea M. Ghez, Committee Chair

University of California, Los Angeles

2012

Table of Contents

List of Figures

List of Tables

Acknowledgments

I could not have made it through graduate school without the support and encouragement from so many people. I must first thank my husband, Matt Smith, who has been my biggest supporter from the beginning of this long journey. You always put me and my education first. When I wanted to change fields completely and start over as an undergraduate in astrophysics (10 years ago!), you backed me up and gave me the encouragement I needed. And all the little things you have done, from driving me to and from campus every day, to cooking and cleaning, to making me laugh when I needed to most, have made my life as a graduate student as comfortable as it could have possibly been. I could not have pursued my dream of becoming an astronomer without you and I am so fortunate to have you by my side.

I thank my graduate school advisor, Andrea Ghez, whose passion and enthusiasm for astronomy were what first drew me to UCLA. And for the six years since, your excitement has continued, even when simply showing you a super good-looking Python plot! Your advice on everything from research, to careers, to even personal matters was always given with the highest level of thought and precision. You have taught me how to think and work like a scientist, and there isn't a better person to have learned this from.

I thank Mark Morris for his support and for the many informative discussions about star formation and all things Galactic center. Thank you also to Brad Hansen for always having your door open when I had random questions about stellar dynamics. Thank you, Rainer Schoedel, for your long-distance support and encouragement. Your enthusiasm is contagious and has made for such memorable visits with you at meetings around the world and here at UCLA. I would also like to thank my outside committee members, David Jewitt and Jonathan Mitchell,

for their support and encouragement.

Thank you to my undergraduate research advisor, Sally Oey, for your patience while teaching me the most basic concepts in both programming and astronomy. You always challenged me and made sure I had a fundamental understanding of what it was I was doing. You prepared me for graduate school and for a future career in research.

I thank Jessica Lu, my "mini-advisor", for not only being one of the most brilliant people I know, but also for the great friendship and laughs we have shared. From day one, you were always willing to help me with whatever I was struggling with, and I can't count the number of times I made you explain the direction some normal vector is pointing. I think I finally got it! Your mentoring and your friendship over the years have been invaluable. I thank my good friend, Quinn Konopacky for some of the best laughs I've had in graduate school, for the rides to campus, for answering all of my random (and sometimes silly) questions about life in and after graduate school, and of course, for pin the tail on the donkey. To Shelley Wright, thank you for allowing me the privilege of being your officemate for a month. You were the "older", wiser graduate student who helped me on my first day at UCLA, and since then you have become a great friend. I also thank Tuan Do for his friendship and his ability to answer questions about anything that even Google cannot answer. I thank my good friend and current officemate, Greg Mace, for almost never using the office. But thank you also for stopping in from time to time to catch up, to laugh at my dumb jokes, and to make me feel cool by saying I remind you of Liz Lemon (you don't know how big of a compliment that is to me!). Leo Meyer, thank you for being such a great friend, mentor, and most of all, the best barista at *Café Leo*. I could always bounce my crazy research ideas off of you without feeling silly, and you always

took the time to help me figure things out. And thank you for coming back to astronomy. What a major loss for the financial world. And thank you to Mike Fitzgerald for your friendship, the much-needed coffee breaks, the good times at CfAO events, and for your help with the simplest of Python questions.

I thank my parents for supporting me in my (many) educational pursuits all these years, and my sisters and brother for their love and support, and for still keeping me in the loop about *everything* going on back home, despite my being 2300 miles away. Thank you to my mother-in-law, Valerie Smith, for everything you've done for me over the past 14 years and making me feel at home every time we would visit. To Melvin and Colleen Smith, thank you for your love and encouragement and for moving out West!

I was lucky enough to have somewhat of a life outside of graduate school that I shared with many dear friends. Thank you to my best friend, Audrey Davey, for your support, encouragement, and all the laughs over the past decade. You were always there when I needed someone to vent to, and to help me with my number crunching. Thank you to Verena Niemeyer, Filmon Zerai, and Steph Gordziel for all the dinners, the parties, and especially our weekly beach volleyball ritual. To Julia Bischoff, thank you for all the good times and great laughs, especially during our road trip. Whenever I need to smile, I can just think back to your uncontrollable laughter as we sat on the train in Venice. Thank you, Janet Mace, for all the Draw Somethings; I'll be back in the game soon! Without all of you, I could not have maintained my sanity during this long and difficult road.

I have to also acknowledge my two cats, Phoebe, who we affectionately call "flea-be" and she knows why, and Mr. Bojangles, who never leaves my side and who is forcing me to type this with one hand as he lay sleeping on my arm.

I acknowledge that results presented in this thesis are based on published

works with additional co-authors. In particular, Chapter 2 is a version of Yelda et al. (2010) and Chapter 3 is a version of Yelda et al. (2012b), which includes some results first reported in Yelda et al. (2012a). Support for this work was provided by the NSF grant AST-0406816 and the NSF Science & Technology Center for Adaptive Optics, managed by UCSC (AST-9876783). Additional support for S.Y. was provided by a UCLA Dissertation Year Fellowship. The W. M. Keck Observatory is operated as a scientific partnership among the California Institute of Technology, the University of California and the National Aeronautics and Space Administration. The Observatory was made possible by the generous financial support of the W. M. Keck Foundation.

Vita

2002	B.A. (Psychology) University of Michigan, Dearborn
2006-2011	Research Assistant Department of Astronomy and Astrophysics University of California, Los Angeles
2007, 2009-2011	Teaching Assistant Department of Astronomy and Astrophysics University of California, Los Angeles
2008	M.S. (Astronomy) University of California, Los Angeles
2011-2012	Dissertation Year Fellowship University of California, Los Angeles

Publications

Yelda, S., Ghez, A. M., Lu, J. R., Do, T., Meyer, L., Morris, M. R., "Adaptive Optics Observations of the Galactic Center Young Stars" 2012, SPIE Conference Proceedings: Astronomical Telescopes & Instruments, in press.

Clarkson, W., Ghez, A. M., Morris, M. R., Lu, J. R., Stolte, A., McCrady, N., Do, T., Yelda, S., "Proper Motions of the Arches Cluster with Keck LGS-

Adaptive Optics: The First Kinematic Mass Measurement of the Arches", 2012, The Astrophysical Journal, 751, 132.

Yelda, S., Ghez, A. M., Lu, J. R., Do, T., Clarkson, W., Matthews, K., "Increasing the Scientific Return of Stellar Orbits at the Galactic Center", 2011, ASP Conference Proceedings: "The Galactic Center: A Window on the Nuclear Environment of Disk Galaxies", 439, 167.

Yelda, S., Lu, J. R., Ghez, A. M., Clarkson, W., Anderson, J., Do, T., Matthews, K., "Improving Galactic Center Astrometry by Reducing the Effects of Geometric Distortion", 2010, The Astrophysical Journal, 725, 331.

Do, T., Ghez, A. M., Morris, M. R., Lu, J. R., Matthews, K., Yelda, S., Larkin, J., "High angular resolution integral-field spectroscopy of the Galaxy's nuclear cluster: a missing stellar cusp?", 2009, The Astrophysical Journal, 703, 1323.

Do, T., Ghez, A. M., Morris, M. R., Yelda, S., Meyer, L., Lu, J. R., Hornstein, S. D., Matthews, K., "A Near-Infrared Variability Study of the Galactic Black Hole: A Red Noise Source with No Detected Periodicity", 2009, The Astrophysical Journal, 691, 1021.

Ghez, A. M., Salim, S., Weinberg, N. N., Lu, J. R., Do, T., Dunn, J. K., Matthews, K., Morris, M. R., Yelda, S., Becklin, E. E., Kremenek, T., Milosavljevic, M., Naiman, J., "Measuring Distance and Properties of the Milky Way's Central Supermassive Black Hole with Stellar Orbits", 2008, The Astrophysical Journal, 689, 1044.

CHAPTER 1

Introduction

As the closest galactic nucleus, the center of our Milky Way offers a unique opportunity to understand both star formation and stellar dynamics near a supermassive black hole (SMBH). At a distance of 8 kpc, the Galactic center (GC) is the only nucleus in which individual stars are resolved and their orbits precisely measured (Figure 1.1). With such orbital measurements, it has become well established that the center of our Galaxy is anchored by a central black hole of mass 4×10^6 $M_\odot$ and is at a distance of 8 kpc (Eckart & Genzel, 1996, 1997; Genzel et al., 1996; Ghez et al., 1998, 2000, 2003, 2005b, 2008; Schödel et al., 2002, 2003; Eisenhauer et al., 2003, 2005; Gillessen et al., 2009b). While the SMBH is surrounded by a nuclear stellar cluster made up of predominantly late-type giants (age >1 Gyr), there also exists an enigmatic population of young, massive stars in the central parsec that have been spectroscopically identified as main sequence, giant, and supergiant stars of O and B type, as well as evolved Wolf-Rayet (WR) stars (Allen et al., 1990; Krabbe et al., 1991, 1995; Blum et al., 1995; Tamblyn et al., 1996; Najarro et al., 1997; Ghez et al., 2003; Paumard et al., 2006; Do et al., 2009a; Bartko et al., 2010). The more massive of these stars ($M > 20$ $M_\odot$) have an inner edge at $R \sim 0\farcs8$ (0.032 pc at the distance to the Galactic center) and are estimated to have an age of 6 ± 2 Myr (Paumard et al., 2006). The central $1''$, however, contains a population of lighter ($\sim$3 - 20 $M_\odot$) B-type main sequence stars, known as the "S-stars" and seven of which are

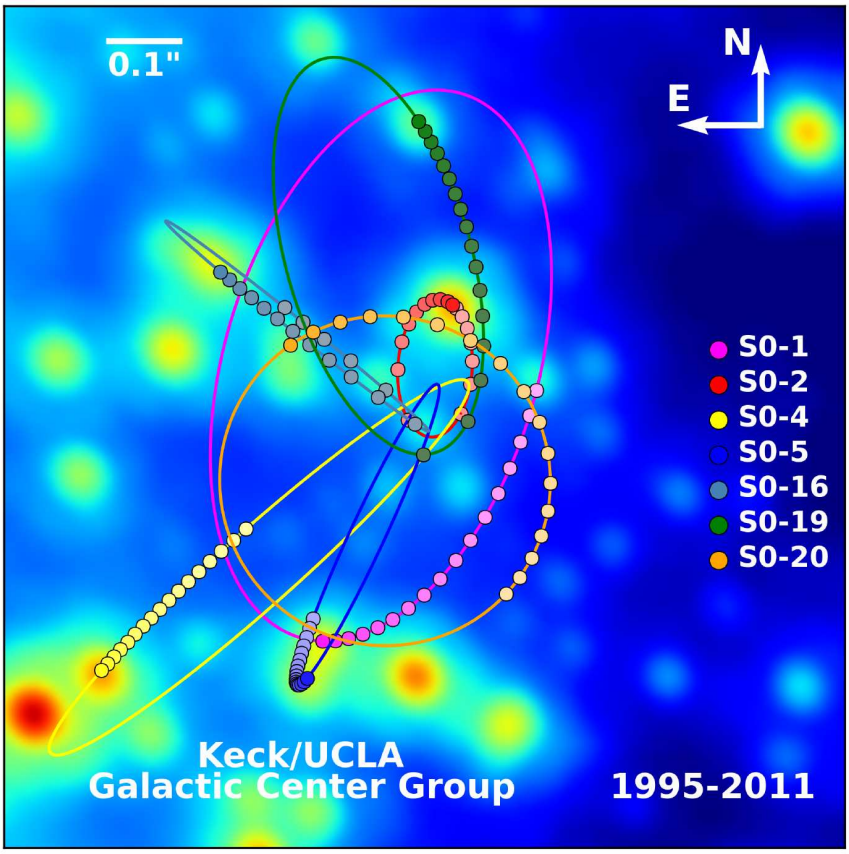

Figure 1.1 Stellar orbits in the central 1″ (∼0.04 pc) of the Galaxy for seven short-period stars based on data obtained with the Keck telescopes. These orbits have been used to constrain the properties of the Milky Way's central supermassive black hole.

identified in Figure 1.1. It is unclear whether or not the S-stars are related to the more massive stars outside the central arcsecond, as their main sequence lifetime allows for an age of up to 400 Myr.

The presence of young stars near a supermassive black hole is puzzling given that such a region seems inhospitable to star formation. To withstand the tidal force of the SMBH, molecular clouds in the region must have densities greater than $6{\times}10^{10}$ $(R$ / 0.1 pc$)^{-3}$cm^{-3}. However, the observed densities throughout the GC range from $\sim 10^3$ - 10^8 cm^{-3}, with the highest densities measured in the

circumnuclear disk (CND) located at ∼2 - 5 pc (Morris, 1993; Jackson et al., 1993; Christopher et al., 2005; Montero-Castaño et al., 2009). While the presence of the young stars in the GC was once suggested as evidence against the existence of a supermassive black hole (Sanders, 1992), we are now faced with the challenge of understanding how they can exist in its vicinity.

Given the age of the population and the relaxation timescale in the Galactic center (∼1 Gyr; Hopman & Alexander, 2006), the dynamical properties of the young stars hold important clues to their formation. Perhaps the most telling kinematic feature is the presence of a clockwise (CW) stellar disk, which may contain up to ∼50% of the young stars in the central parsec and has an inner edge at a projected radius of $R \sim 0\farcs8$ (0.032 pc at the distance to the Galactic center; Levin & Beloborodov, 2003; Genzel et al., 2003; Paumard et al., 2006; Lu et al., 2009; Bartko et al., 2009). Interior to this disk lies the S-stars, which have randomly-oriented orbital planes (Schödel et al., 2003; Ghez et al., 2005b; Eisenhauer et al., 2005; Gillessen et al., 2009b), as expected from vector resonant relaxation arguments (Rauch & Tremaine, 1996; Hopman & Alexander, 2006; Alexander et al., 2007; Perets et al., 2009).

A second, counterclockwise disk of O and WR stars was also proposed to exist just outside the CW structure (Genzel et al., 2003; Paumard et al., 2006), but with more data, and higher precision measurements, the coherent nature of this structure has been brought into question. While Bartko et al. (2009) claim that this is instead a dissolving disk or a streamer, Lu et al. (2009) observe these stars to have randomly-oriented orbital planes. The suggested reasons for the discrepant observations included the smaller field of view and relatively low astrometric precision in the Lu et al. (2009) observations as compared to those used in Bartko et al. (2009). Expanding on the measurements from these previous

studies with higher precision data and an increased time baseline over a large field of view will help to resolve this issue and shed light on these stars' connection to the clockwise disk.

With advancements in telescope and instrument technologies, we are now in a position to make precision measurements of the individual stars throughout the central parsec of the Galaxy. In particular, the advent of laser guide star adaptive optics has made it possible to obtain spectra in this crowded field, measurements which provide spectral identification and velocities along the line of sight. With LGS AO, high-precision astrometry can be obtained over a much larger field of view than the previously used speckle imaging technique. Such data can be used to estimate the orbits of the young stars in the GC. In this thesis, I use high-angular-resolution imaging and spectroscopy obtained with the W. M. Keck telescopes over a time baseline of 16 years to understand the origin and dynamical evolution of the Galactic center young star population.

1.1 Adaptive Optics Observations of the Galactic Center

The extreme stellar density of the Galactic center region requires the use of high angular resolution imaging and spectroscopy. However, the turbulent atmosphere prevents even the largest telescopes from achieving their theoretical diffraction limit. To partially overcome the atmospheric effects, early astrometric programs on the Galactic center made use of speckle imaging techniques, which reached an angular resolution of $0\farcs15$ and provided 1-10 mas astrometry for stars down to $K = 16$ mag (Eckart & Genzel, 1996, 1997; Genzel et al., 1996; Ghez et al., 1998). A huge leap in our knowledge of the Galactic center environment came nearly a decade ago with the advent of adaptive optics (AO), systems which are now commonly found on large 8-10 m class telescopes. Adaptive optics systems

correct for the distorting effects of the atmosphere in real time by measuring the aberrations in the wavefront of a bright guide star and subsequently adjusting the shape of a deformable mirror, which acts to flatten the wavefront of the science image. These corrections can be made on either a bright natural guide star (NGS) near the science target, or a laser guide star (LGS) in the case that there is no NGS nearby. In LGS mode, the laser does not provide information on the low-order tip-tilt (TT) term, thereby requiring observations of a natural reference star near the science target. The TT star, however, can be fainter and further than the reference star required by NGS AO. For Galactic center observations made with the Keck AO system, which requires an optically-bright natural guide star, LGS mode is typically used, as the closest guide star that is sufficiently bright in the optical ($R = 13.7$) is located $\delta r_{SgrA*} = 19''$ away. This star is instead used as the TT star for LGS AO observations of the Galactic center.

Adaptive optics systems have proven to be extremely powerful tools for studies of the Galactic center. The technology has dramatically improved the quality of Galactic center observations in many aspects, including an order of magnitude improvement in (1) the angular resolution, (2) the number of detected stars, and (3) the astrometric precision. In fact, the astrometric precision obtained with LGS AO (0.1 mas) is such that positional measurements are now limited by systematics from geometric optical distortion and differential atmospheric refraction (Chapter 2). AO has also allowed for spectroscopic observations of individual stars in the high-density environment of the GC, providing spectral identifications and radial velocity measurements (Ghez et al., 2003; Paumard et al., 2006; Do et al., 2009a; Bartko et al., 2010). This thesis takes advantage of a rich data set containing LGS AO imaging from 2004-2011 and LGS AO spectroscopy from 2007-2011 of the Galactic center. Combined with speckle imaging data taken between 1995 and 2005 at Keck, this results in the longest time baseline used for

studying the kinematics of the young stars at the Galactic center to date.

1.2 Observational Constraints on Young Star Origin Scenarios

Early kinematic work on the young stars located at $R = 1''$ - $10''$ revealed coherent rotation that was nearly perpendicular to the general rotation of the Galaxy and appeared as a clockwise pattern on the sky (Genzel et al., 2000). The velocities were later shown to be consistent with motion in a thin disk-like structure with an opening angle of $<10^{\circ}$ (Levin & Beloborodov, 2003). As these stars have not yet had time to dynamically relax, it was immediately suggested that this orbital motion likely contains clues to the origin of the population (Genzel et al., 2000; Levin & Beloborodov, 2003). Since then, several kinematic studies have been undertaken in an effort to understand the detailed orbital properties of the population and compare them to theoretical predictions.

Many scenarios have been put forth to explain the presence of this population in the Galactic center (for a review, see Genzel et al., 2010). Rejuvenation scenarios, in which old stars collide with one another or are tidally stripped of their outer envelopes as they approach the SMBH and now appear to be young (Lee, 1996; Genzel et al., 2003; Davies et al., 1998; Davies & King, 2005), have been challenged by observations (Martins et al., 2008) as well as the theoretically low collision rates (Dale et al., 2009). The most promising origin scenarios, however, include (1) the formation of a massive, compact stellar cluster several parsecs from the GC, which migrated inward under dynamical friction with the surrounding stellar population (Gerhard, 2001), and (2) *in situ* star formation in a dense, gaseous disk surrounding the SMBH (Levin & Beloborodov, 2003), a process

that has been suggested to occur at the centers of other galaxies (Kolykhalov & Syunyaev, 1980; Shlosman & Begelman, 1987; Morris & Serabyn, 1996; Sanders, 1998; Goodman, 2003; Nayakshin, 2006). Each of these scenarios could produce a thin, disk-like structure of stars in the Galactic center, as is currently observed.

An infalling cluster that formed several parsecs away can migrate into the Galactic center by dynamical friction with the background stellar population. The dynamical friction timescale must be shorter than the lifetime of an O star ($\sim$ 6 Myr) and depends on the cluster's mass, initial radius, and initial velocity (Gerhard, 2001; Binney & Tremaine, 2008). For a cluster with properties similar to the Arches and Quintuplet, with masses on order of $\sim 10^4$ $M_\odot$ (Figer, 2008), the dynamical friction timescale is only short enough for the cluster to migrate into the GC in <6 Myr, if it formed no more than a few pc away (Gerhard, 2001). At larger initial distances, much more massive clusters are required. Furthermore, the observed location of the massive stars in the GC ($r = 0.04 \sim 1$ pc) requires that the cluster be extremely dense to prevent tidal disruption at larger radii. In fact, such small galactocentric radii can only be reached if an intermediate mass black hole (IMBH) with an unrealistically-high mass is embedded in the center of the cluster (Hansen & Milosavljević, 2003; Kim et al., 2004; Gürkan & Rasio, 2005). Other observational challenges to a cluster infall origin include the surface density profile, which has been measured to fall off as r^{-2} (Paumard et al., 2006; Lu et al., 2009; Bartko et al., 2009), much steeper than that predicted by this model, $r^{-0.75}$ (Berukoff & Hansen, 2006). It is unclear, however, whether the steep surface density profile is a result of mass segregation in the cluster itself. If mass segregation has occurred within the cluster, the lower-mass stars will be tidally stripped at larger radii, while the more massive stars will survive the migration longer and end up closer to the GC (Berukoff & Hansen, 2006). This would also produce a mass function that varies with radius. Obtaining orbits of

stars at larger radii and stars less massive than the W-R/O stars will allow for direct tests of this prediction.

The currently favored origin scenario for the young star population in the GC is *in situ* star formation around the black hole. Star formation in a self-gravitating gas disk surrounding the central black hole can explain the presence of the young stars if the disk was massive and dense enough to overcome the tidal shear from the black hole and undergo turbulent fragmentation to form stars (Levin & Beloborodov, 2003). Levin (2007) argued that the resulting surface number density of stars should scale as $r^{-2.25}$, which is consistent with observations of stars in the clockwise disk (Paumard et al., 2006; Lu et al., 2009; Bartko et al., 2009).

Most scenarios of star formation in an accretion disk around a SMBH suggest that the stars should have circular orbits. Lu et al. (2009) estimate that ∼30% of the candidate disk stars have eccentricity lower limits of $e > 0.2$. Bartko et al. (2009) found a bimodal eccentricity distribution and reported an average eccentricity of $< e > = 0.51$. This bimodality has proven difficult to explain for a relatively thin stellar disk (A. M. Madigan, private communication). With an initially circular disk, however, the eccentricities can be excited to values of $e > 0.2$ through dynamical relaxation over the stars' lifetimes if the IMF were top-heavy (Alexander et al., 2007). Alternatively, the stars may have formed in an initially eccentric disk which was the result of an infalling giant molecular cloud or possibly built up through collisions of clouds (Mapelli et al., 2008; Yusef-Zadeh & Wardle, 2008; Wardle & Yusef-Zadeh, 2008; Bonnell & Rice, 2008) that were initially on eccentric orbits.

While roughly half of the central parsec's young stars do not orbit within the plane of the clockwise disk, the fact that all of the stars appear to have the same age implies that they likely formed together. In this case, some mechanism(s)

leading to the observed dynamical properties must be invoked. Under the assumption that all of the stars formed in the clockwise disk, it is theoretically possible to excite the orbits to such high inclinations that they are no longer kinematically associated with the original disk. Disruption by an intermediate mass black hole or by the circumnuclear disk, which is located at R = 1.8 pc (Christopher et al., 2005), for example, are two such mechanisms that have been suggested for scattering stars off of the disk plane (Yu et al., 2007; Šubr et al., 2009; Haas et al., 2011a).

While the existence of the CW disk is well-established, many of the orbital properties of the disk stars have yet to be constrained. Orbital parameter estimates can be determined from a single measurement of a star's radius and velocity vectors. While the stars' 2D positions and 3D velocities are obtained directly from observations, the line-of-sight distances (z) relative to the black hole are not. This missing piece of information limits our ability to assign disk membership and therefore characterize the structure of the disk. A star's acceleration in the plane of the sky can provide its line-of-sight distance, and lack of an acceleration can constrain the star's position to $|z| > 0$. Lu et al. (2009) measured a significant acceleration for one star at a projected radius of $R \sim 1''$ and found acceleration upper limits for a handful of other young stars. Without any constraints from accelerations, one must resort to a statistical approach in estimating orbits by adopting a prior. This requires full understanding of the impact the prior has on the resulting orbital estimates. For example, assuming a uniform prior in z has been shown to result in orbital solutions that are biased toward periapse (Lu et al., 2009; Bartko et al., 2009). To avoid this particular bias, Lu et al. (2009) assumed a uniform acceleration prior in order to sample the line-of-sight distance, with the minimum acceleration set by assuming bound orbits, and a maximum acceleration set by the stars' projected radii (which trans-

lates to a minimum z of zero). In addition to the biases introduced by priors, the impact of measurement errors in such an analysis has yet to be investigated thoroughly.

Both star formation and dynamical evolution scenarios can be constrained further by obtaining high-precision measurements of stars throughout the central parsec. Currently, there are at least three challenges we face: 1) understanding the sources of systematic error in astrometric measurements (Chapter 2), 2) detecting accelerations in the plane of the sky, which are critical for constraining stellar orbits (Chapter 3), and 3) understanding the impacts of measurement error and *a priori* assumptions on the orbital estimates (Chapter 3). In this thesis, I address each of these issues in an attempt to explore the detailed dynamical properties of the young star population in the Galactic center and shed light on the so-called "paradox of youth".

CHAPTER 2

Improving Galactic Center Astrometry by Reducing the Effects of Geometric Distortion

High angular resolution astrometry has been a powerful technique for studies of the Galactic center (GC). Over the last decade, it has revealed a supermassive black hole (Eckart & Genzel, 1997; Ghez et al., 1998), a disk of young stars surrounding the central supermassive black hole (Levin & Beloborodov, 2003; Genzel et al., 2003; Paumard et al., 2006; Lu et al., 2009), and allowed for measurements of the orbit about the GC of the Arches, a massive young star cluster located at a projected galacto-centric distance of 30 pc (Stolte et al., 2008; Clarkson et al., 2012). While the speckle imaging work carried out on the Galactic center in the 1990's had typical centroiding uncertainties of $\sim$1 mas, recent deep, adaptive optics (AO) images have improved the precision of stellar centroiding by a factor of $\sim$6-7, significantly increasing the scientific potential of astrometry at the Galactic center (Ghez et al., 2008; Gillessen et al., 2009b). Further gains in astrometric precision would allow ultra-precise measurements of the distance to the Galactic center (R_o), measurements of individual stellar orbits at larger galacto-centric radii, and, more ambitiously, measurements of post-Newtonian effects in the orbits of short-period stars (e.g., Jaroszyński, 1998, 1999; Salim & Gould, 1999; Fragile & Mathews, 2000; Rubilar & Eckart, 2001; Weinberg et al., 2005; Zucker & Alexander, 2007; Kraniotis, 2007; Nucita et al., 2007; Will, 2008). Such gains

will also probe the possibility that the supermassive black hole is moving with respect to the central stellar cluster, due either to the gravitational influence of a massive companion or from a systematic effect produced by improper alignment of images.

Two factors that currently limit astrometric measurements of stars at the Galactic center are (1) the level to which AO cameras' geometric distortions are known and (2) differential atmospheric refraction (DAR), which has not yet been explicitly corrected for in any Galactic center proper motion study (Ghez et al., 2008; Gillessen et al., 2009b). While optical distortion from an infrared camera is expected to be static, distortion from the AO system and the atmosphere not corrected by AO, is not. Initial estimates of the optical distortions for AO cameras are generally based on either the optical design or laboratory test, which do not perfectly match the actual optical distortion of the system. Both uncorrected camera distortions and DAR leave $\sim$1-5 mas scale distortions over the spatial scales of the SiO masers that are used to define the Sgr A*-radio rest frame for proper motions of stars at the Galactic center (see e.g., Reid et al., 2007). These are significantly larger than the $\sim$0.2-0.3 mas precision achieved in the relative astrometry of Ghez et al. (2008) and Gillessen et al. (2009b). The impact of all these effects on relative astrometry has been minimized by mapping the coordinate systems of different epochs of observations to a reference frame using high order transformations, allowing $\sim$0.2-0.3 mas precision in the relative astrometry to be achieved. However, the full impact of these effects is imposed on astrometric measurements in a reference frame that is known to be at rest with respect to Sgr A*-radio (henceforth, the Sgr A*-radio rest frame). Therefore, correcting these effects would have the greatest improvement on astrometric measurements in the maser frame. Relative astrometry would also be improved by eliminating these effects before the images, which are obtained at different times and occasionally

different orientations, are combined.

In this chapter, we improve the astrometric accuracy and precision of Keck AO measurements of the Galactic center by (1) deriving a new, publicly-available distortion solution for the infrared imaging camera behind the Keck AO system (NIRC2) and (2) correcting for DAR. Furthermore, having corrected for these effects, we show that an astrometric reference frame for the Galactic center can now be established with Sgr A* at rest to within 0.09 mas yr^{-1} (3.4 km s^{-1} at the distance to the GC), thereby improving the stability of the reference frame. Section 2.1 presents observations and analysis of the globular cluster, M92, that were used to derive the first distortion solution for NIRC2 that is based upon on-sky measurements, as opposed to NIRC2's internal pinhole mask. We also discuss the observations and analysis of Galactic center data used to illustrate the impact of our technical work here. We present the results and tests of the distortion solution in §2.2.1. In §2.3.1 we apply this solution, along with corrections for DAR, to observations of the GC and report the positions and proper motions of a set of infrared astrometric standards (N$\sim 10^3$) in a Sgr A*-radio rest frame. In §2.3.3, we measure the motion of the stellar cluster in this reference frame and show that these stars exhibit significant net motion in the plane of the Galaxy. Finally, we consider the implications of this work for measuring relativistic and extended mass effects on short period stars. While this work has been carried out in the context of the Galactic center, the new distortion solution also benefits a wide array of other science that is currently being carried out with NIRC2, including astrometric studies of extrasolar planets (Marois et al., 2008), brown dwarf binaries (Konopacky et al., 2007; Liu et al., 2008; Dupuy et al., 2008), compact objects (Cameron & Kulkarni, 2007), and external galaxies (e.g., Max et al., 2005).

2.1 Observations & Analysis

In this section, we report all the new observations and analysis carried out for this chapter. Section 2.1.1 discusses the observations of M92 that are used to create a new NIRC2 distortion model presented in §2.2.1. Section 2.1.2 describes the observations of the Galactic center that are used to test the new distortion model in §2.2.2 and to generate a new IR astrometric reference frame at the Galactic center in §2.3.1.

2.1.1 M92

To characterize the optical distortion in the NIRC2 camera, it is ideal to compare the measured set of stellar positions to those in a distortion-free reference frame. As this idealized reference frame does not exist, we choose observations of M92 (NGC 6341; α = 17 17 07.27, δ = +43 08 11.5) made with the well-characterized Advanced Camera for Surveys Wide Field Channel (ACS/WFC) on the Hubble Space Telescope (HST), which has a plate scale $\sim$49.9933 $\pm$ 0.0005 mas pix^{-1} and position angle offset = -0.0006^o $\pm$ 0.0023^o (van der Marel et al., 2007), as our reference frame. The static distortion in this camera has been corrected down to the $\sim$0.01 pix ($\sim$0.5 mas) level (Anderson, 2005; Anderson & King, 2006; Anderson, 2007) and is therefore a useful reference for our purposes given the level of distortion in the NIRC2 camera. While several clusters were considered during the planning phase of this project, M92 was chosen because it had been extensively observed with ACS/WFC, was observable in the northern hemisphere during the summer, was sufficiently crowded, and had an isolated natural guide star (NGS) available. The HST observations of M92 used for this analysis were made on 2006 April 11 with both the F814W (I) and F606W (V) filters as part of the ACS Survey of Globular Clusters (GO-10775, PI: A. Sarajedini). The

details of the observations and data reduction can be found in Anderson et al. (2008), and the catalog of positions were provided in advance of publication by J. Anderson. We used the Anderson (2007) correction for the linear skew in ACS to ensure that our reference frame was free of skew.

Observations of M92 were made from 2007 June to 2009 May using the AO system on the W. M. Keck II 10 m telescope with the facility near-infrared camera NIRC2 (PI: K. Matthews). Aside from the 2007 July data set, these observations were obtained upon completion of our primary science program for the night (Galactic center astrometry), or when conditions were not optimal for the primary science program (e.g., clouds were present or seeing was relatively poor). All images were taken with the narrow field camera, which maps the 1024×1024 pix array into $\sim 10'' \times 10''$ field of view, and through the K' (λ_0=2.12 μm, $\Delta\lambda$=0.35 μm) band-pass filter. While the Natural Guide Star adaptive optics (NGSAO) system was used to obtain the majority of the data, the Laser Guide Star (LGS) AO system was used for one run in 2008 June. The NGSAO atmospheric corrections and the LGSAO low-order, tip-tilt corrections were made using visible observations of USNO-B1.0 1331-0325486 (R = 8.5 mag). The resulting image point spread functions (PSFs) had Strehl ratios of $\sim$0.55 and FWHM of $\sim$50 mas, on average.

M92 was observed at 79 different combinations of position angles (PAs) and offsets (see Figure 2.1), with three identical exposures taken at each pointing. This allowed for a given star to fall on several different parts of the detector over the course of the observations. We note for clarity that the reported PA value is the angle (eastward) of the camera's columns with respect to North. The field of view of NIRC2's narrow camera contained the Natural Guide Star (NGS) in each pointing, and in most cases two other nearby stars, which are circled in

Figure 2.2; this facilitated the process of combining the positional information from all of the different pointings. Table 2.1 provides the details of the NIRC2 M92 observations.

The M92 images are calibrated and stellar positions are measured from these images using standard techniques. Specifically, the images are first dark- and sky-subtracted, flat-fielded, and bad-pixel and cosmic ray corrected. The images are then run through the point spread function (PSF) fitting program *StarFinder* (Diolaiti et al., 2000), which is optimized for adaptive optics observations of crowded stellar fields to identify and characterize stars in the field of view. *StarFinder* iteratively constructs a PSF from a set of bright stars in the field, which have been pre-selected by the user. For M92, a total of 16 stars spread out across the detector are used to obtain a PSF that is representative of the entire field. The resulting PSF is then cross-correlated with the image and detections with a correlation peak of at least 0.7 are considered candidate stars. Relative astrometry and photometry are extracted by fitting the PSF to each candidate star. This results in a star list, containing the NIRC2 pixel coordinates for the detected stars for each of the 237 images.

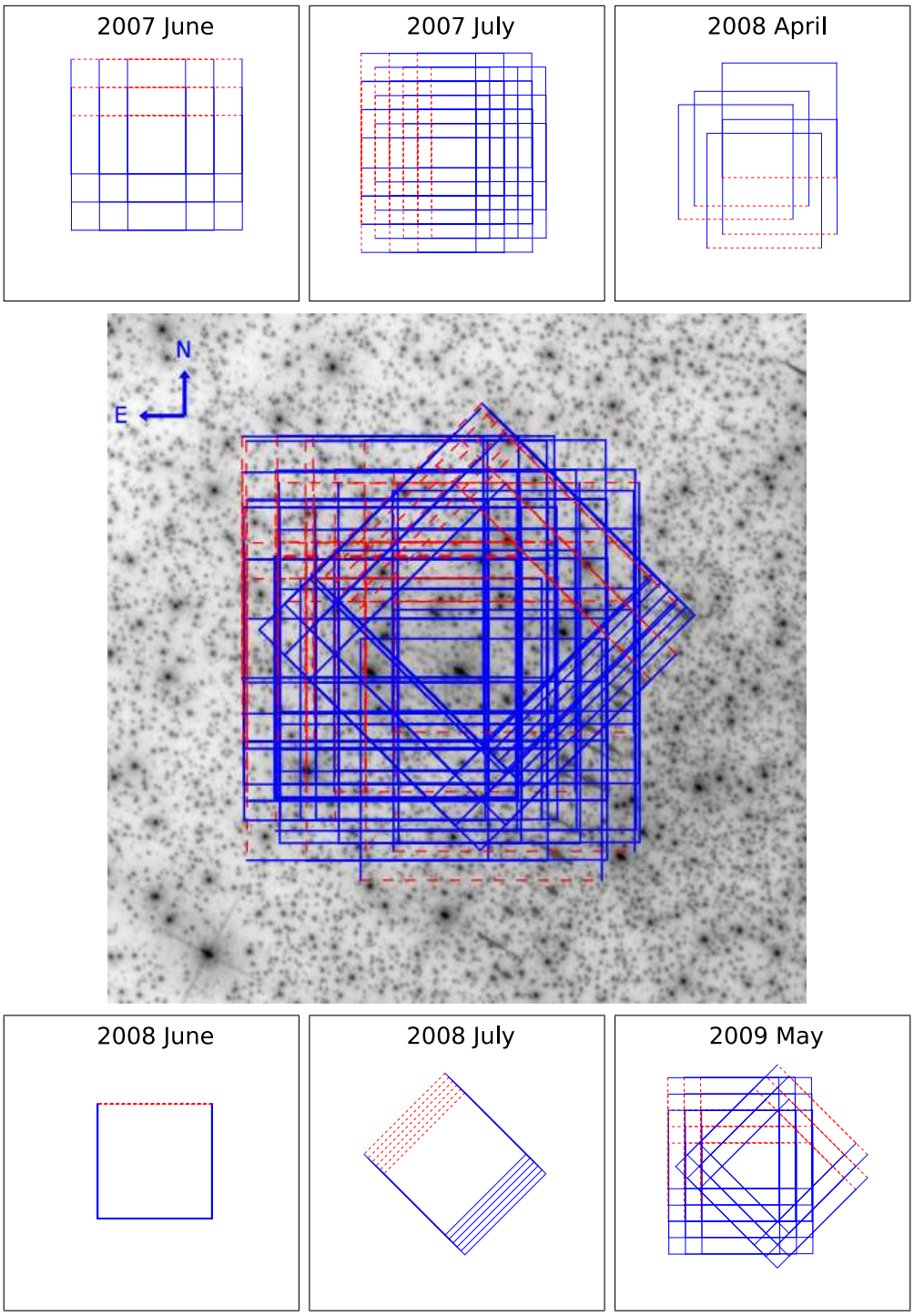

Figure 2.1 ACS/WFC image of M92 with the 79 NIRC2 pointings. The red dashed side of each NIRC2 box denotes the top of the detector's field of view. Each NIRC2 field is $10''\times10''$, while the ACS image shown is $\sim30''\times30''$. The patterns for the individual epochs' exposures are shown in the insets.

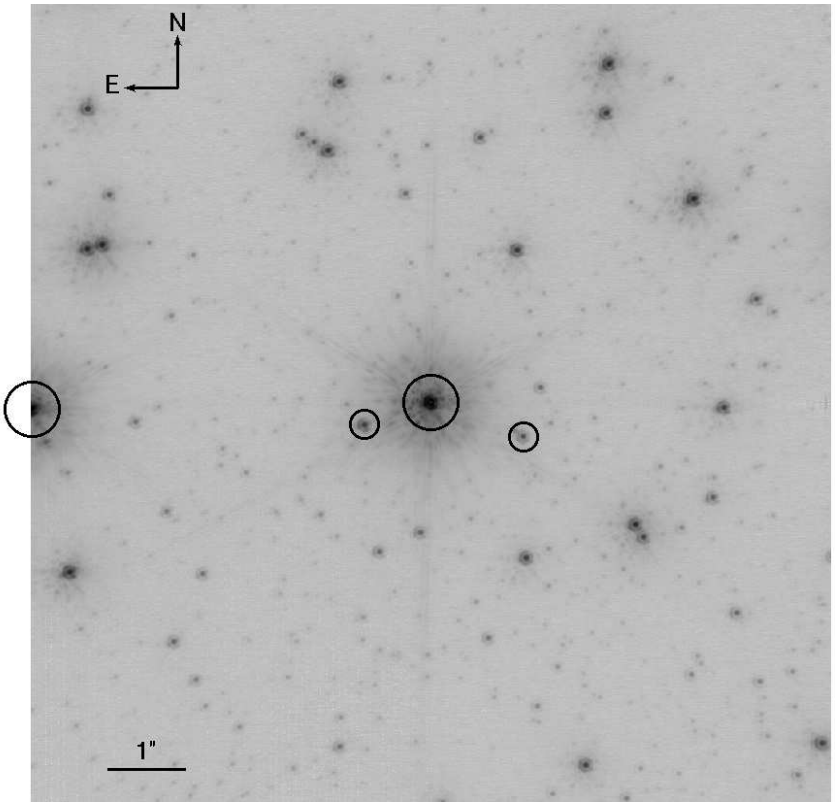

Figure 2.2 Diffraction-limited NGSAO NIRC2 image of one of the M92 fields used to characterize the optical distortion in the NIRC2 camera. The circled stars at the center of the image, the NGS and two fainter stars, are present in most of the M92 NIRC2 observations and are used to register the images, each of which had a different position/orientation on the sky. The NGS and the circled star $\sim 5''$ to its east were almost always (i.e., when clouds weren't present) detected at levels that saturated the detector and were therefore removed from the analysis (see §2.1).

Table 2.1. Summary of M92 Images

Date[a] (UT)	PA (deg)	$(X,Y)_{GS}$[b] (pix)	$\Delta(X,Y)$[c] (pix)	El (deg)	Temp (K)	Pressure (mbar)	RH[d] %	ΔR[e] (mas)	t×coadd (sec)	⟨FWHM⟩ (mas)	⟨Strehl⟩	N stars detected	N stars used	$\langle\sigma_{pos}\rangle$[f] (pix)
2007.47	0	508, 512	0, 0	53	271.2	616.8	92	2.74	3.0×10	49	0.55	105	69	0.037
			254, -252	53	271.1	616.7	89	2.77		48	0.55	145	58	0.035
			251, 252	52	271.1	616.7	89	2.81		48	0.57	112	46	0.045
			-251, -252	52	271.3	616.7	93	2.84		48	0.59	176	56	0.034
			-253, 250	51	271.3	616.7	93	2.89		49	0.54	110	57	0.037
			251, 0	51	271.2	616.7	95	2.93		48	0.60	124	58	0.044
			-251, -1	50	271.2	616.7	95	2.97		47	0.59	115	64	0.049
			2, -250	50	271.1	616.7	96	3.02		47	0.58	124	47	0.063
			0, 253	49	271.0	616.6	97	3.07		46	0.61	94	51	0.058
2007.57	90	457, 499	0, 0	67	272.9	615.3	11	2.07	0.8×60	45	0.64	73	47	0.031
			255, -251	67	272.9	615.3	11	2.07		45	0.72	53	38	0.048
			251, 255	67	272.9	615.3	12	2.07		45	0.68	84	41	0.042
			-249, -251	67	272.9	615.2	12	2.07		46	0.66	65	40	0.052
			-252, 251	67	272.9	615.2	13	2.07		45	0.69	132	52	0.031
			254, 2	67	272.9	615.3	13	2.07		45	0.71	72	44	0.021
			-252, 0	66	272.9	615.2	13	2.08		45	0.72	93	48	0.037
			3, -250	66	272.8	615.2	12	2.09		44	0.73	69	47	0.029
			-2, 253	66	272.8	615.2	12	2.10		45	0.72	92	51	0.024
			-125, -124	65	272.8	615.2	12	2.11		45	0.72	85	50	0.026
			128, -375	65	272.8	615.2	13	2.12		45	0.73	89	48	0.030

Table 2.1—Continued

Date[a] (UT)	PA (deg)	$(X,Y)_{GS}$[b] (pix)	$\Delta(X,Y)$[c] (pix)	El (deg)	Temp (K)	Pressure (mbar)	RH[d] %	ΔR[e] (mas)	t×coadd (sec)	⟨FWHM⟩ (mas)	⟨Strehl⟩	N stars detected	N stars used	$\langle\sigma_{pos}\rangle$[f] (pix)
			126, 129	65	272.8	615.2	12	2.14		45	0.70	84	54	0.030
			-374, -376	64	272.8	615.2	13	2.16		46	0.69	47	33	0.033
			-378, 126	64	272.8	615.2	12	2.18		46	0.68	74	39	0.067
			128, -123	63	272.9	615.2	12	2.20		46	0.67	77	49	0.038
			-374, -125	62	272.9	615.2	12	2.22		46	0.67	72	38	0.032
			-121, -374	62	272.9	615.2	12	2.25		46	0.67	51	38	0.028
			-127, 129	61	273.0	615.2	11	2.27		46	0.66	87	45	0.045
			127, -121	60	273.1	615.1	11	2.31		46	0.65	81	47	0.045
			380, -373	60	273.2	615.1	12	2.34		47	0.63	52	33	0.071
			378, 132	59	273.1	615.1	12	2.38		46	0.65	51	39	0.025
			-126, -373	58	273.3	615.1	12	2.41		46	0.66	54	36	0.032
			-128, 130	57	273.3	615.1	11	2.46		47	0.65	76	45	0.031
			381, -120	56	273.3	615.0	11	2.50		47	0.64	43	35	0.040
			-127, -120	56	273.4	615.0	10	2.55		47	0.61	64	43	0.022
			129, -371	55	273.3	615.0	12	2.60		47	0.63	54	39	0.040
			124, 133	54	273.3	614.9	11	2.66		48	0.60	79	47	0.036
2008.32	180	496, 477	0, 0	67	271.0	615.8	82	2.08	0.8×60	47	0.56	31	20	0.022
			252, -252	67	271.0	615.7	81	2.08		48	0.53	32	0	-1.000
			248, 253	67	271.0	615.8	83	2.08		48	0.55	55	15	0.061
			113, -375	63	271.5	616.0	70	2.23		48	0.54	12	0	-1.000

Table 2.1—Continued

Date[a] (UT)	PA (deg)	$(X,Y)_{GS}$[b] (pix)	$\Delta(X,Y)$[c] (pix)	El (deg)	Temp (K)	Pressure (mbar)	RH[d] %	ΔR[e] (mas)	t×coadd (sec)	⟨FWHM⟩ (mas)	⟨Strehl⟩	N stars detected	N stars used	$\langle\sigma_{pos}\rangle$[f] (pix)
			-143, -120	59	271.0	616.0	77	2.39		51	0.44	13	9	0.022
2008.42	0	776, 573	0, 0	42	273.3	616.0	64	3.85	1.5×6	50	0.47	30	0	-1.000
			4, 4	42	273.2	616.1	65	3.89		51	0.48	32	0	-1.000
			-4, 0	42	273.2	616.1	65	3.93		58	0.29	29	0	-1.000
			4, 0	41	273.2	616.1	65	3.97		54	0.38	32	0	-1.000
			-4, 3	41	273.2	616.1	65	4.01		54	0.38	25	0	-1.000
			-5, -4	41	273.2	616.1	65	4.05		54	0.40	26	0	-1.000
2008.56	45	173, 565	0, 0	50	271.6	617.2	39	3.03	2.8×10	66	0.35	128	32	0.077
			0, -49	49	271.6	617.2	39	3.07		63	0.35	110	35	0.068
			0, -100	49	271.6	617.1	39	3.11		72	0.30	88	30	0.065
			1, -149	48	271.6	617.1	39	3.16		72	0.29	89	30	0.089
			3, -199	48	271.6	616.9	39	3.21		51	0.46	131	45	0.065
			2, -249	47	271.6	616.9	39	3.26		86	0.22	89	21	0.067
2009.35	0	910, 668	0, 0	66	270.6	614.6	36	2.11	0.8×60	52	0.45	18	10	0.072
			1, -153	66	270.6	614.6	36	2.12		49	0.50	19	15	0.031
			3, -304	65	270.6	614.6	36	2.13		49	0.47	19	16	0.026
			-154, -2	65	270.5	614.6	36	2.14		51	0.48	25	17	0.036
			-153, -154	65	270.5	614.7	36	2.15		47	0.58	30	25	0.036

Table 2.1—Continued

Date[a] (UT)	PA (deg)	$(X,Y)_{GS}$[b] (pix)	$\Delta(X,Y)$[c] (pix)	El (deg)	Temp (K)	Pressure (mbar)	RH[d] %	ΔR[e] (mas)	t×coadd (sec)	⟨FWHM⟩ (mas)	⟨Strehl⟩	N stars detected	N stars used	$\langle\sigma_{pos}\rangle$[f] (pix)
			-152, -305	64	270.5	614.7	36	2.16		50	0.47	27	22	0.038
			-305, -4	64	270.8	614.7	35	2.17		50	0.51	23	19	0.034
			-305, -155	64	271.0	614.7	35	2.18		56	0.38	26	12	0.041
			-302, -306	63	271.0	614.7	35	2.20		63	0.30	22	13	0.033
2009.35	90	365, 411	0, 0	62	270.8	614.6	35	2.27	0.8×60	49	0.49	25	19	0.025
			2, -153	61	270.8	614.6	35	2.29		50	0.48	24	17	0.028
			0, -302	61	270.8	614.5	35	2.31		50	0.47	10	8	0.031
			-151, -1	60	270.8	614.5	35	2.33		50	0.48	28	19	0.061
			-152, -154	60	270.8	614.5	36	2.35		47	0.56	29	22	0.035
			-149, -304	59	270.8	614.5	36	2.37		46	0.67	26	20	0.020
			-302, -4	59	270.6	614.5	36	2.40		46	0.61	35	24	0.023
			-304, -156	58	270.7	614.5	34	2.42		46	0.64	29	26	0.025
			-301, -305	58	270.7	614.5	34	2.45		48	0.53	18	15	0.030
2009.35	315	697, 499	0, 0	56	271.1	614.5	33	2.55	0.8×60	45	0.67	38	27	0.055
			2, -152	55	271.1	614.5	33	2.58		45	0.68	48	29	0.055
			0, -304	55	271.0	614.4	34	2.62		45	0.67	58	30	0.060
			-152, 0	54	270.7	614.3	35	2.66		47	0.56	35	22	0.044
			-148, -154	54	270.7	614.3	35	2.69		56	0.32	21	13	0.085
			-149, -305	53	270.7	614.3	35	2.74		50	0.45	43	18	0.078

Table 2.1—Continued

Date[a] (UT)	PA (deg)	$(X,Y)_{GS}$[b] (pix)	$\Delta(X,Y)$[c] (pix)	El (deg)	Temp (K)	Pressure (mbar)	RH[d] %	ΔR[e] (mas)	t×coadd (sec)	⟨FWHM⟩ (mas)	⟨Strehl⟩	N stars detected	N stars used	$\langle\sigma_{pos}\rangle$[f] (pix)
			-300, -2	53	270.6	614.4	35	2.78		50	0.45	25	18	0.044
			-301, -154	52	270.6	614.5	35	2.82		59	0.29	21	13	0.063

[a]2008 June 3 data set taken in LGS-AO mode. All other data sets taken with NGS-AO.

[b]Position of guide star in first image of a given epoch.

[c]Positional offset of guide star in NIRC2 pixels relative to first pointing of epoch.

[d]Relative Humidity.

[e]Model of differential atmospheric refraction relative to center of image.

[f]Images thrown out are given a value of -1.0 for the average positional uncertainty (see text for details).

Final star lists for each pointing are produced by combining each set of three star lists from images with the same observational setup. Positions are taken from the first of the three images and the centroiding uncertainties are estimated empirically using the three images at each pointing and computing the RMS error of each star's position[1]. The median centroiding uncertainty is ∼0.035 pix (∼0.35 mas; see Figure 2.3). Two initial criteria are used to trim out false or problematic source detections. First, only stars detected in all three images are kept. Second, we remove the two brightest stars (the NGS and a comparably bright star ∼5.″1 to the east that appears in the images of 147 out of 237 pointings) and any other source identified within a 60-pixel (∼ 0.″6) radius of these stars (see Figure 2.2). These two sources are ∼1 mag brighter than any other detected star and are often detected at levels that saturate the detector. Saturation leads to poor PSF matching with the empirical PSF estimate, and consequently poor positional estimates for these two stars, as well as ∼20-50 false detections in their halos. With these selection criteria, the 79 final star lists contain a combined total of 3846 stellar position measurements of more than 150 independent stars.

2.1.2 Galactic Center

Two types of Galactic center observations were obtained with the NIRC2 narrow camera and the LGSAO system at Keck. First, two sets of deep Galactic center observations centered roughly on Sgr A* offer a test of the new distortion model because something is changed in each. In a data set from 2007 May, previously reported in Ghez et al. (2008), 103 frames were obtained with a camera orientation of PA=0^o (May 17) and another 20 frames were collected at PA=200^o (May 20).

[1]Choosing positions from the first of the three images was unintentional, but should not affect the results since the centroiding uncertainties are smaller than the level of distortion in the images.

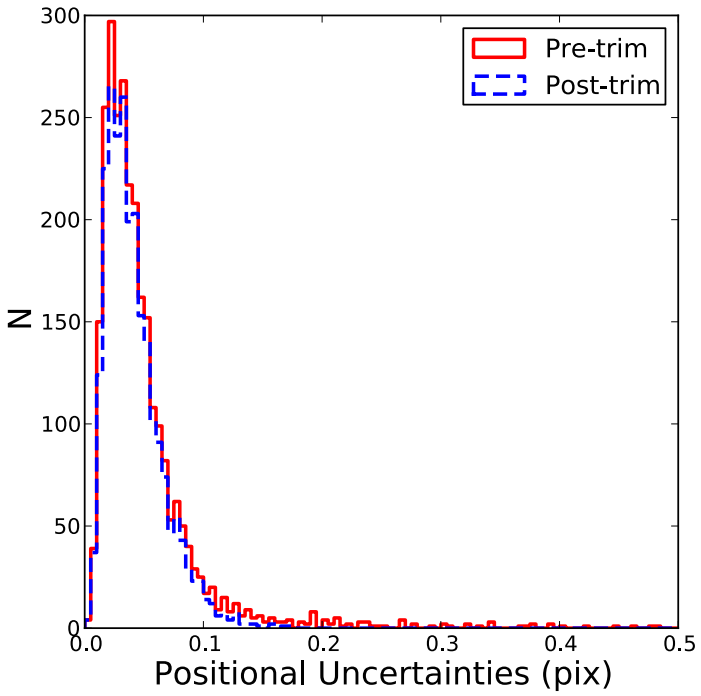

Figure 2.3 Histogram of NIRC2 (plate scale $\sim$10 mas pix^{-1}) positional uncertainties for stars matched to the ACS/WFC star list before (*solid red*) and after (*dashed blue*) removing all outliers (see text). The uncertainties are calculated from the RMS error of the positions obtained from three images taken at the same position on the sky. The distributions peak at $\sim$0.02 pix.

In a new data set collected on 2008 May 15, the first 22 images were obtained with the LGSAO system and the remaining 112 images were taken with the NGSAO system; the Strehl ratio was 31% and 22% for the LGSAO and NGSAO data that evening, respectively. Second, three new epochs of observations, designed to measure the relative positions of seven IR-bright SiO masers, were carried out in 2008 May, 2009 June, and 2010 May, bringing the total number of such observations to six. These observations are primarily to generate an astrometric reference frame in which Sgr A* is at rest, but are also used as an additional test of the new distortion solution. The 2008 May data set is identical to those reported in detail in Ghez et al. (2008, Appendix C) and consists of a total of 27 images, which were obtained in a widely dithered ($6'' \times 6''$) 9-point box pattern with three images at each of the nine pointing positions. The 2009 June data set differed in that we repeated the box pattern three times, resulting in a deeper image by $\sim$0.5 magnitude, and the 2010 May data set was similar in total exposure time to the initial mode, but made a trade of less coadds for more recorded images in an attempt to compensate for the shorter atmospheric coherence times that evening. We note that these observations were generally carried out under poorer seeing conditions than our other GC observations (see below), since the quality of the seeing is not the limiting factor in measuring the positions of the SiO masers. These observations are summarized in Table 2.2. USNO 0600-28577051, which is offset by $9.4''$ E and $16.9''$ N from Sgr A*, served as the tip-tilt star for all of the LGSAO observations and as the natural guide star for the NGSAO observation.

Table 2.2. Summary of GC Maser Mosaic Images

Date (UT)	Start Pos[a] (pix)	$t_{exp,i}$×coadd (sec)	N_{exp}[b]	K'_{lim}[c] (mag)	FWHM (mas)	Strehl	N_{stars}	σ_{pos} mas
2005 June 30	851, 426	0.181×60	2	15.6	62	0.25	1306	1.14
2006 May 3	852, 426	0.181×60	3	15.7	60	0.21	1372	1.13
2007 Aug 12	852, 425	0.181×60	3	15.7	58	0.23	1626	1.06
2008 May 15	856, 427	0.181×60	3	15.9	52	0.31	2017	1.04
2009 June 28	855, 426	0.181×60	9	16.2	63	0.20	2354	1.04
2010 May 4	858, 428	0.181×60	3	15.5	69	0.17	1174	1.08

Note. — All images taken at PA=0^o.

[a]The X,Y position of IRS16C in the first image of a given epoch.

[b]The number of exposures per dither position.

[c]K'_{lim} is the magnitude at which the cumulative distribution function of the observed K' magnitudes reaches 90% of the total sample size.

All the GC images are calibrated in a similar manner to what was carried out with the M92 data sets, with a few exceptions. First, all images are corrected for differential atmospheric refraction (see §2.2.1) and the geometric optical distortion using the new model derived in §2.2.1. Second, all the images from each epoch (and each configuration in the case of the deep central $10'' \times 10''$ observations) are combined into a final average map as described in Ghez et al. (2008). In addition, three subset images, each containing 1/3 of the data, are created for estimating centroiding uncertainties.

Astrometry was extracted using *StarFinder* (Diolaiti et al., 2000) in a similar manner as in Ghez et al. (2008), with a few minor modifications. Images from the individual pointings were analyzed with a correlation threshold of 0.9 in order to minimize spurious detections. The maser mosaics and the deep central $10'' \times 10''$ average maps were run at a correlation threshold of 0.8, but used an improved algorithm to minimize spurious detections, which is described in §2.5.

2.2 A New Distortion Model for NIRC2's Narrow Camera

Ground-based astrometric observations are subject to rapidly varying effects (such as instantaneous changes in the spatial pattern of PSF variation around the detector), which lead to measurable nonlinear residuals between positions even when comparing frames within a night (e.g., Lu, 2008). In this work, we seek to characterize the static component of the distortion, which may be dominated by distortion within NIRC2 itself. Residuals between observed stellar positions in NIRC2 and their counterparts in a nominally distortion-free frame are represented as a single residual surface, which when smoothed, forms our distortion model. The result is a model for the time-averaged distortion felt by the telescope and detector system.

2.2.1 Constructing the Model

To find the best fit model for NIRC2's geometric optical distortion from the M92 observations, one must account for the fact that the ACS/WFC data do not suffer from differential atmospheric refraction (DAR), while the NIRC2 data come from ground-based observations and therefore will be affected by the earth's atmosphere (see Figure 2.4).

Differential atmospheric refraction will compress an image along the zenith direction, causing the apparent separation between a pair of stars to be smaller than their true separation. Since the stellar positions are first geometrically distorted by the atmosphere and then the telescope/instrument, it is best to "undo" these effects in the reverse direction. Assuming one has a distortion solution for NIRC2 at hand, to convert observed positions to their counterparts in rectilinear space, the distortion solution should first be applied to the observed positions, and then corrected for DAR. When attempting to find the distortion solution, however, the positions observed at NIRC2 cannot be corrected for DAR to compare with HST because we do not know the distortion-corrected positions this process requires. Instead, DAR is applied to the HST positions to produce a set of reference positions that should correspond to distortion-free positions as observed through the atmosphere. Because the effects of DAR depend on the elevation and, to a much lesser extent, the atmospheric conditions of the observations, it is necessary to create a separate DAR-transformed ACS/WFC star list for each NIRC2 image and associated star list. To account for DAR, we follow the prescription for DAR given in Gubler & Tytler (1998). The stellar positions are only corrected for achromatic DAR, as the error from chromatic DAR is negligible ($<$0.2 mas) relative to the residual distortion in ACS/WFC ($\sim$0.5 mas). Neglecting chromatic effects, the DAR term (ΔR) depends on (1)

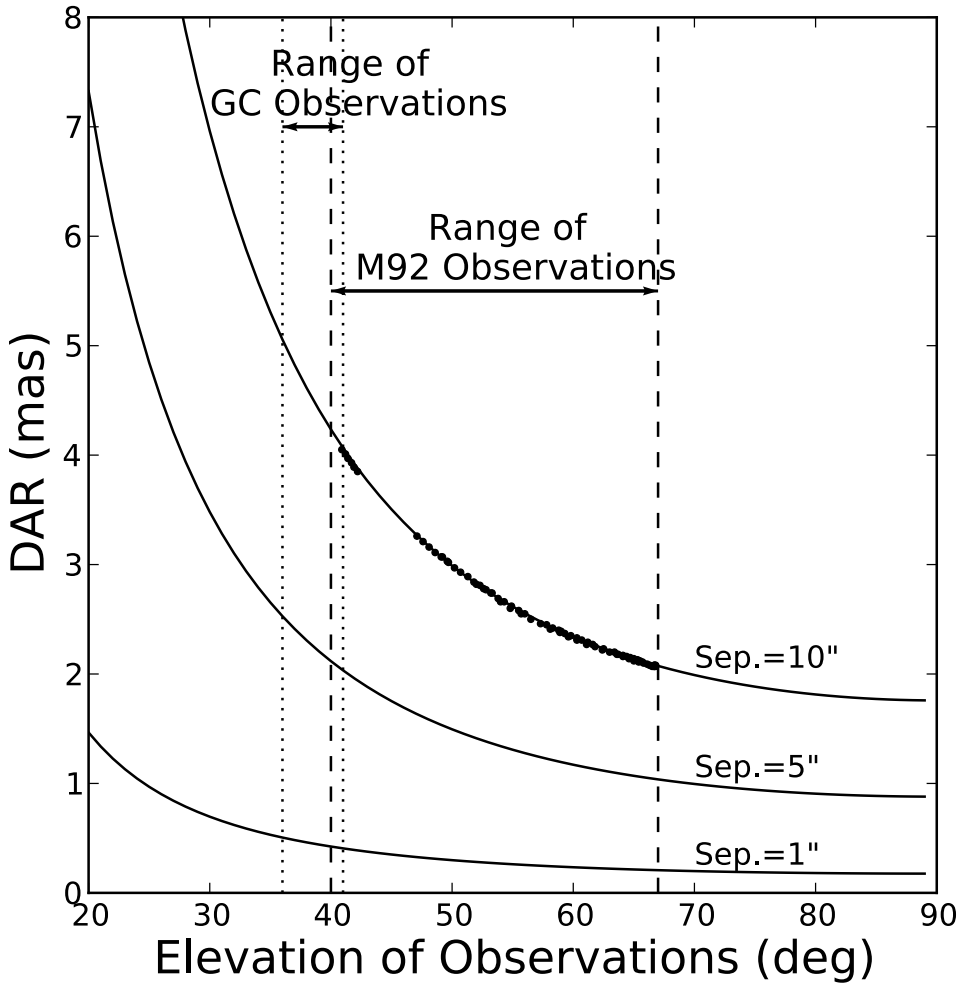

Figure 2.4 The predicted achromatic differential atmospheric refraction at a range of elevation angles for *typical* observing conditions at Keck. DAR causes the separation of two stars to appear smaller along the zenith direction and the change in the separation is shown for three pairs of stars separated by 1", 5", and 10". The black dots show the amount of DAR over the 10" field for each of the M92 observations used in the distortion solution. These are slightly offset from the predicted curve because the atmospheric conditions differed slightly from the reference conditions used to generate the curves. The ranges of our GC and M92 observations are also shown. In all of our analyses, we apply DAR corrections to each individual image based on the conditions at the time.

the observed zenith angle of star 1, (2) the wavelength of the observations, (3) the observed zenith separation of star 1 and star 2, (4) the temperature at the observatory, (5) the pressure at the observatory, and (6) the relative humidity at the observatory. The atmospheric parameters of interest are downloaded from an archive maintained at the Canada-France-Hawaii Telescope (CFHT)[2] for the night of each observation. These values are recorded every five minutes, allowing us to find the appropriate atmospheric conditions on Mauna Kea within three minutes of the observation (Lu, 2008). As shown in Figure 2.4, the magnitude of the achromatic effect over the range of elevations for the M92 observations is expected to be ∼2-4 mas across NIRC2's 10″ field of view, along the elevation axis.

Each of the NIRC2 star lists described in §2.1.1 is then used as a reference coordinate system into which the ACS/WFC star list of positions is transformed. In this process, the ACS/WFC star list is transformed by minimizing the error-weighted (NIRC2 positional errors) net displacement for all the stars, allowing for translation, rotation, and a global plate scale (i.e., a four-parameter transformation model). This process is described in greater detail in Ghez et al. (2008) and Lu et al. (2009). Only sources that are cross-identified in both the NIRC2 and ACS star lists are used in the remaining analysis. From the 79 separate alignments, a total of 2743 matches in stellar positions are obtained for a total of 150 independent stars. The differences in the matched positions, or deltas, are a result of the optical distortion in NIRC2.

The mapping of ACS positions to NIRC2 positions shows clear spatial structure across the detector, as expected from optical distortion (see Figure 2.5). However, some deltas are inconsistent with those in their immediate surround-

[2] `http://kiloaoloa.soest.hawaii.edu/archive/wx/cfht/`

ings. These outliers are found by examining the vector deviations in 205×205 pixel bins and determining the average and standard deviation. Any 3σ outliers in either the X or Y direction are removed. A total of 75 deltas are removed based on this criterion. An additional cut ($>3\sigma$) in each of these bins is made on NIRC2 positional uncertainties, as they may vary with respect to detector position. This cut removes 73 data points, four of which were also eliminated by the first cut. These bins are examined a second time for vector outliers, as they often show a rather wide distribution. The average and standard deviation in each bin are recalculated and the vector outliers ($>3\sigma$) are removed once again. This resulted in an additional loss of 26 deltas.

Many of the eliminated measurements come from common stars or images. We therefore remove all measurements of the 9 out of 150 stars and of the 8 out of 79 images that were eliminated more than 20% of the time by the sigma-clipping process. Many of these problematic stars have close neighbors ($< 0\farcs2$) that are not resolved or not well measured in the lower-resolution ACS observations (FWHM∼70 mas for the F814W observations). The majority of the rejected frames have exposure times less than 10 sec, while the remaining frames are at least 30 sec. This results in significantly higher centroiding uncertainties, residual atmospheric effects, and fewer stars detected. We note that our trimming criteria mentioned above also result in the exclusion of all data from the 2008 June epoch (t_{int} = 9 sec), which coincidentally was the only M92 data set taken in LGSAO mode. Although the 2008 April data set had relatively long exposure times (t_{int} = 48 sec), the observations were heavily impacted by clouds and the AO system was often unable to remain locked on the NGS. These rejected frames show a value of -1.0 in the last column of Table 2.1. Our final data set consists of 2398 positional deviations between ACS and NIRC2, with median centroiding uncertainty for the NIRC2 images of 0.035 pix (∼0.35 mas). The vector plot for this cleaned sample

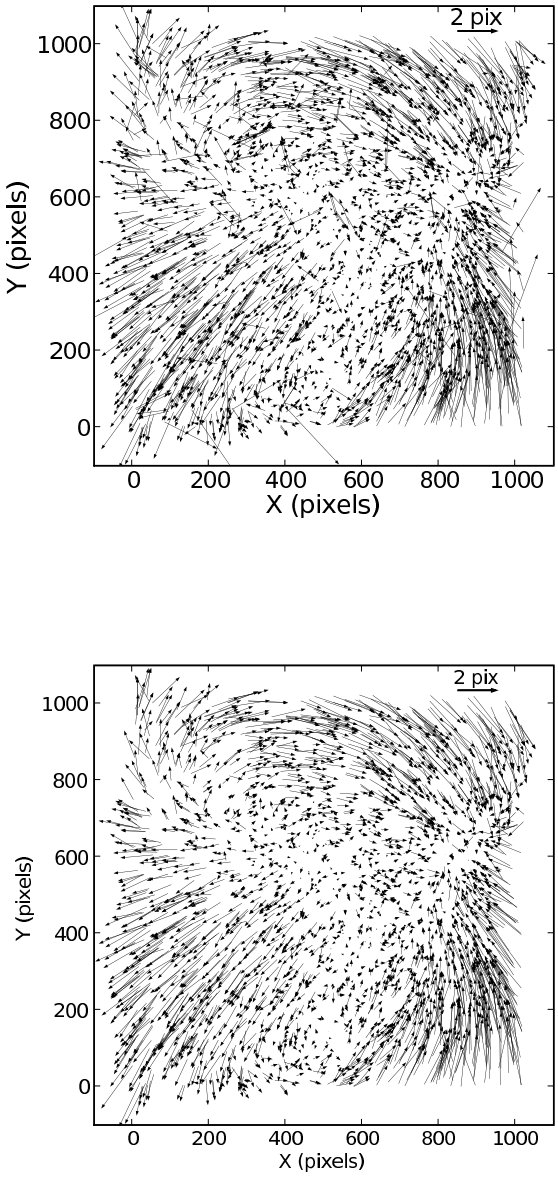

Figure 2.5 Optical distortion in the NIRC2 camera obtained from positional measurements of stars in the globular cluster M92. Arrows indicate the difference between measurements made with NIRC2 (*arrow tail*) and ACS/WFC (*arrow head*), which has a well characterized distortion solution to the ∼0.5 mas level (Anderson & King, 2006; Anderson, 2007). The two figures show pre- (*top*) and post- (*bottom*) trimming.

is shown in the bottom of Figure 2.5.

A bivariate B-spline is fit to the distortion map (Figure 2.5) using the SciPy package *interpolate*, and a look-up table sampled at each of the 1024×1024 NIRC2 pixels is subsequently produced. The effect of the smoothing factor (f; which is related to the number of nearest-neighbor measurements used to calculate the smoothing) used in the interpolation routine was investigated extensively in order to find a good compromise between the closeness of fit and the smoothness of fit. The residuals between the original distortion vectors in the bottom panel of Figure 2.5 and the computed shift at the nearest pixel (from the smoothed look-up table) were measured. The median deviation is found to increase until $f \sim 150$, where it plateaus at a value of $\sim$0.27 pix. We choose for our interpolation the smoothing factor that gave nearly the lowest median deviation, $f = 135$. Although the deviations were lower for distortion solutions created with smaller smoothing factors, the edge effects were prominent in the look-up tables and the distribution of deviations was much larger (for details on surface fitting and the choice of smoothing factors, see Dierckx, 1995). The resulting look-up tables for shifts in X and Y are shown in Figure 2.6, and are produced in the form of FITS files that may be fed into the IRAF routine, *Drizzle* (Fruchter & Hook, 2002), to correct for the optical distortion. Figure 2.7 (left) shows a histogram of these values.

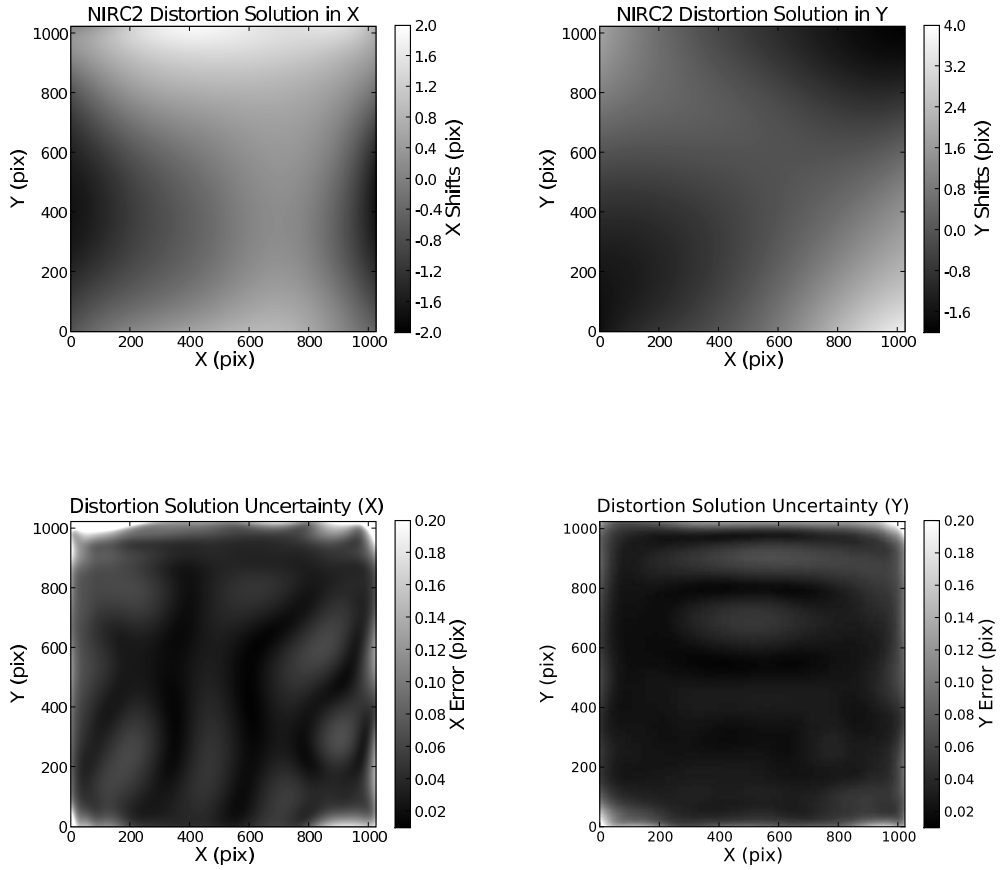

Figure 2.6 (*Top*) Distortion solution in the form of a look-up table for X (*left*) and Y (*right*). The tables give the X and Y values for each pixel required to remove the optical distortion from NIRC2 images. This was generated by fitting a surface to the distortion map in the bottom of Figure 2.5. (*Bottom*) RMS error of the 1000 simulations of the distortion solution based on M92 data (§2.2.1) for X (*left*) and Y (*right*). The images are shown in linear stretch. The average errors in X and Y are $(\sigma_X, \sigma_Y) = (0.05, 0.04)$ pix $\sim$ ($\sim$0.5, $\sim$0.4 mas), respectively. Note an additional error of 0.1 pix is required to fully describe the uncertainty in the optical distortion (see §2.2.3).

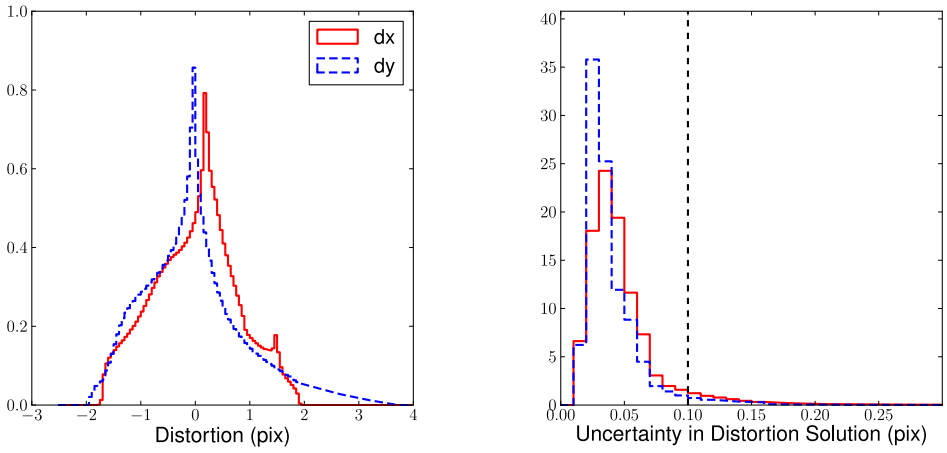

Figure 2.7 (*Left*) Distribution of the shifts in the distortion solution look-up table over all NIRC2 pixels for X (*solid red*) and Y (*dashed blue*). (*Right*) Distribution of the RMS uncertainties from the 1000 simulations of the distortion solution. The average errors in X and Y are 0.05±0.04 pix and 0.04±0.02 pix, respectively. The vertical dashed line represents the additive error that is found when the models are tested with Galactic center data (see §2.2.2).

Statistical uncertainties in the distortion solution were computed by running a bootstrap analysis with 1000 trials. In each trial, we generated a random set of data pulled from the observed data, allowing for replacement after each data point was sampled, and then derived a distortion model from this resampled data set. The RMS error with respect to the distortion solution (i.e., the actual distortion solution was taken as the average) was calculated at each pixel and the results are shown in the bottom of Figure 2.6. The average errors in X and Y are $(\sigma_X, \sigma_Y) = (0.05, 0.04)$ pix $\sim$ (0.5, 0.4 mas), respectively. We can see the uncertainties are highest near the edge of the detector, where the spline algorithm is least robust. The uncertainties are also shown in the form of a histogram in Figure 2.7 along with a histogram of the distortion solution itself.

To solve for the global plate scale and orientation that result from this new

solution, we re-reduce the raw NIRC2 observations of M92 from all epochs, and apply corrections for distortion and DAR to these images. The distortion correction and DAR correction are applied to each image at the same time in the form of look-up tables using the *Drizzle* algorithm as implemented in IRAF (Fruchter & Hook, 2002). The look-up tables are specified in *Drizzle* using the *xgeoim* and *ygeoim* keywords and are FITS files of the same dimensions as the science image. Because DAR depends on the zenith angle and atmospheric conditions, both of which vary in time, the look-up tables are created by first including the distortion solution and then applying the necessary DAR correction. Two FITS files, one for shifts in X and one for shifts in Y, are created for each NIRC2 observation and contain the shifts to be applied to each pixel in the image. From these distortion- and DAR-corrected NIRC2 images, star lists were generated and aligned with the original ACS starlist (without DAR) as described above. The weighted average of the plate scale is $\langle s \rangle = 9.950 \pm 0.003_{stat} \pm 0.001_{abs}$ mas pix^{-1}. The difference between the orientation given in the header of the NIRC2 images[3] and the measured orientation is on average (weighted) $0.254^o \pm 0.014^o_{stat} \pm 0.002^o_{abs}$. We use the RMS errors of the average values from each epoch as the statistical uncertainties, and the absolute errors are the RMS errors in the ACS/WFC plate scale and orientation angle (van der Marel et al., 2007). The results from each epoch of M92 data are shown in Table 2.4.

The new distortion solution and its errors are made public and may be obtained in the form of FITS files at `http://www.astro.ucla.edu/~ghezgroup/distortion`.

[3]The NIRC2 FITS header keyword for the position angle, ROTPOSN, includes a $+0.7^o$ offset (given by header keyword INSTANGL), the observatory value for the angle offset of NIRC2. The nominal position angle for NIRC2 in our analysis is taken as (ROTPOSN - INSTANGL).

2.2.2 Testing the Model

There are two parts to the error in the distortion model when applied to a real data set: static distortion error (hereafter "residual distortion", discussed here) and time-varying effective distortion (discussed in §2.2.3). The residual distortion map on the detector is unknown, but is likely to be highly spatially correlated. The spurious position-shift due to residual distortion when comparing two measurements is a function both of the size of the residual distortion itself, and the difference ΔR in location on the detector between the two measurements.

To estimate the size of the residual distortion from our model, we consider two cases. In the first, sets of images are taken at two very different position angles so that the distance ΔR between two measurements of the same object (and therefore the degree to which the residual distortion varies between measurements) is a strong function of position on the detector. In the second, images are taken at the same position angle, so that ΔR is constant over the image, but are widely dithered (60% of the detector side-length) so that the residual distortion is sampled at widely separated detector locations for all objects.

In both cases, we compare our new distortion model with two previous solutions, which we refer to as "pre-ship" and "PBC". The pre-ship solution[4], which is known to $\sim$4 mas, was found using a pinhole mask, and is in the form of a 3rd-order polynomial. The more recent solution by P. B. Cameron, also from a pinhole mask, is a 4th-order polynomial and improves upon the former solution mainly along the X axis[5].

First, we use the two high precision data sets taken of the central $10'' \times 10''$ on 2007 May 17 and May 20 at two different PAs (0^o and 200^o) with roughly

[4] `http://www2.keck.hawaii.edu/inst/nirc2/preship_testing.pdf`
[5] `http://www.astro.caltech.edu/~pbc/AO/distortion.pdf`

the same central position (§2.1.2). The typical NIRC2 positional uncertainties (the standard deviation, δ_{pos}) for the PA=0^o and PA=200^o images are ∼0.013 pix and ∼0.018 pix, respectively. The PA=200^o image was transformed into the PA=0^o image's coordinate system, again allowing for translation, rotation, and global plate scale. The differences in the aligned positions of stars with K<14.5 are shown in Figure 2.8. This analysis gives an average residual distortion by comparing the positions of a star at two distinct locations on the detector. Our new solution shows significantly less residual structure than the previous solutions. To estimate the magnitude of the residual distortion (σ), we compute the RMS error of the offsets (Δ) between the positions in the two images in the X and Y directions separately[6], and correct for the positional measurement error from both images (δ):

$$\sigma_x = \sqrt{\frac{1}{2}\sum_{i}^{N_{stars}} \frac{(\Delta_{x,i} - \langle\Delta_x\rangle)^2}{(N_{stars}-1)} - \frac{1}{2}(\delta^2_{pos,0^o} + \delta^2_{pos,200^o})} \tag{2.1}$$

where N_{stars} is the number of stars matched across the two images, and $\delta_{pos,0^o}$ and $\delta_{pos,200^o}$ are the positional uncertainties (quoted above) for stars brighter than K=14.5 in the PA=0^o and PA=200^o images, respectively. Average positional uncertainties are subtracted, as opposed to each star's individual uncertainty since most stars brighter than K=14.5 have similar centroiding uncertainties. We compute σ_y similarly. We note that the division by 2 is necessary to determine the residual distortion incurred *per* NIRC2 image. This results in estimates of the residual distortion of ($\sigma_{x,0}$, $\sigma_{y,0}$) = (0.12, 0.11) pix, (0.17, 0.28) pix, and (0.27, 0.22) pix for the new, PBC, and pre-ship solutions, respectively. Thus, the new solution results in smaller residuals by a factor of ∼2-2.5 over both of the previous

[6]These residuals are measured in the PA=0^o image's coordinate system, as this was the reference onto which the PA=200^o image was transformed.

solutions. The uncertainty in the distortion models has not been removed from these values, as the uncertainty in the PBC and pre-ship solutions are unknown. We can, however, remove the average uncertainty in our new model in quadrature (Figure 2.6, bottom) to obtain a final measure of the residual distortion: ($\sigma_{x,0}$, $\sigma_{y,0}$) = (0.11, 0.10) pix.

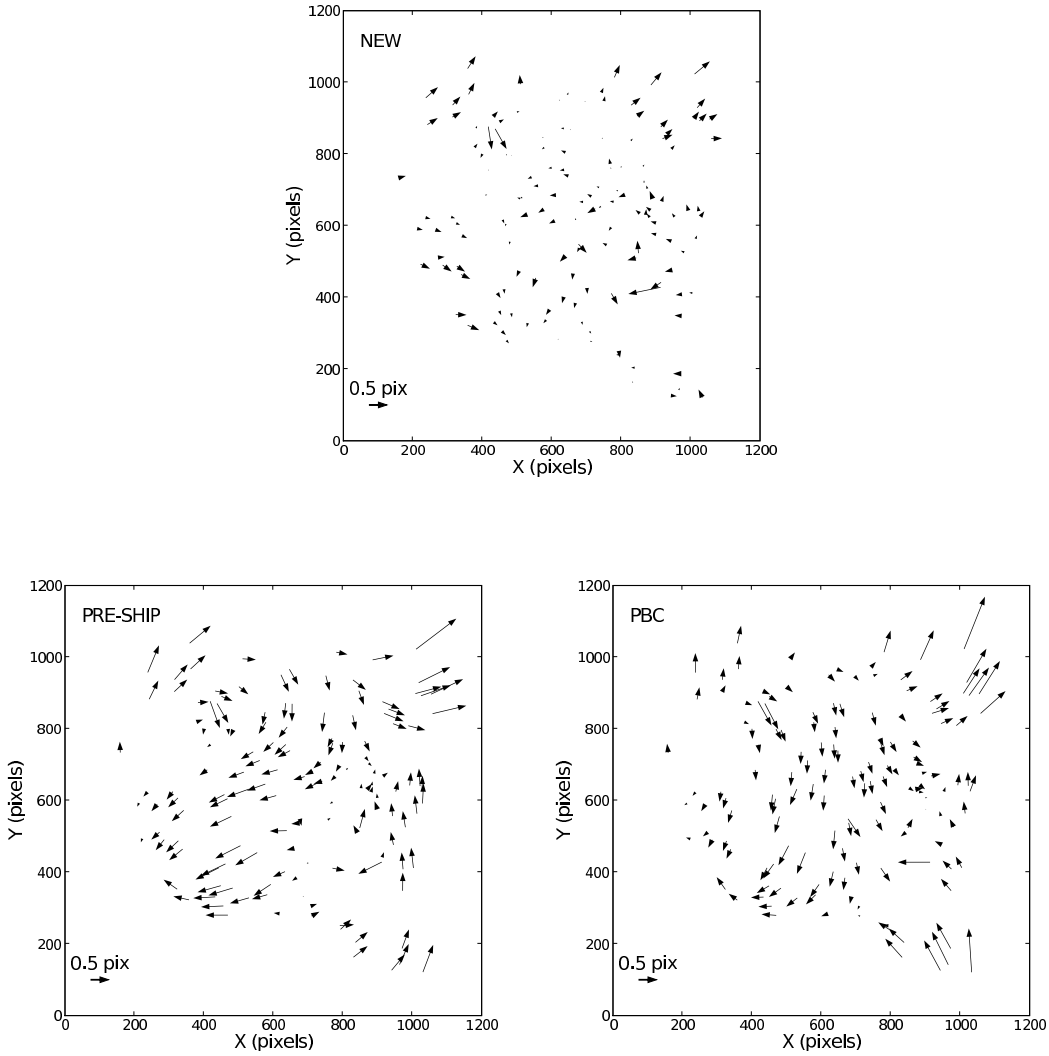

Figure 2.8 Differences between stellar positions in Galactic center images taken at PA=200^o (*arrow tail*) and PA=0^o (*arrow head*) after applying the new (*top*), pre-ship (*bottom left*), and PBC (*bottom right*) distortion solutions. While some residual distortion remains, much of the structure seen after using the pre-ship solution is removed with the new solution. The residual distortion remaining is ($\sigma_{x,0}$, $\sigma_{y,0}$) = (0.12, 0.11) pix, (0.17, 0.28) pix, and (0.27, 0.22) pix for the new, PBC, and pre-ship solutions, respectively.

As an additional check on the distortion solution, we use the images from widely-dithered (6″) 2008 May data set taken at PA=0^o (§2.1.2), which, unlike the test just described, maintain the independence of the X and Y axes as they are shifted relative to one another by only a translation. Largely-dithered data sets are essential in testing the distortion solution because stars are placed on very different locations on the detector and therefore provide a sensitive test of residual distortion. These data have an average RMS error on the positions of 0.05 pix. Only four overlapping fields, each of which was imaged three times and whose centers are the corners of a 6″×6″ box, were examined from this data set (Figure 2.9). Only stars detected in at least 6 of the 12 images (and therefore at least two of the four overlapping fields) were kept in the analysis. The stars had to also be detected in all three exposures at each dither position, and the average of the positions in these three exposures was taken as the position at the corresponding dither position. The error ($\sigma_{x,i}$, $\sigma_{y,i}$) from residual optical distortion of *each star's* offsets (Δx, Δy) from IRS 16SW-E (which was in each of the four fields) was computed as:

$$\sigma_{x,i} = \sqrt{\frac{1}{2}\sum_{j}^{N_{fields}} \frac{(\Delta x_j - \langle \Delta x_j \rangle)^2}{N_{fields}-1} - \frac{1}{2}\frac{1}{N_{fields}} \sum_{j}^{N_{fields}} \left(\frac{\delta^2_{pos,IRS16SWE}}{N_{exp}-1} + \frac{\delta^2_{pos,i}}{N_{exp}-1} \right)} \tag{2.2}$$

and likewise for $\sigma_{y,i}$, where we divide by the number of overlapping fields in which a star was detected (N_{fields}), and we correct for the NIRC2 positional measurement error (the standard deviation, δ_{pos}) per exposure (N_{exp}) for both IRS 16SW-E and star i. The factor of 2 in the denominator accounts for the fact that the distortion affects both stars, IRS 16SW-E and star i. These errors from the residual optical distortion are shown in Figure 2.10 for all three solutions. The median values (σ_x, σ_y) are (0.05, 0.06) pix, (0.07, 0.15) pix, and (0.18, 0.17)

pix, for the new, PBC, and pre-ship solutions, respectively. The new solution was found to significantly improve positional measurements overall as compared to both of the previous solutions and in particular, it is a factor of 3 better in the Y direction over the more recent PBC solution. As mentioned above, the uncertainties in the distortion models have not been removed from these values, as they are unknown for the two previous solutions. For the new distortion solution, however, the RMS offsets are consistent with the average uncertainty in the distortion model itself.

The errors computed using the pairwise analysis are approximately half the size of those reported using the GC observations at two position angles. We note that the pairwise analysis uses measurements that have uncertainties that are a factor of 3 larger than our other test and is therefore more sensitive to the removal of the measurement bias term. We take as the final residual error term for the new NIRC2 distortion solution the value from the first test: ($\sigma_{x,0}$, $\sigma_{y,0}$) = (0.11, 0.10) pix.

2.2.3 Additional Sources of Uncertainty

While the new distortion solution represents a significant step forward in our astrometric capabilities, it still leaves $\sim$0.1 pix or $\sim$1 mas residual distortion in LGSAO images that are widely dithered or taken at different position angles. The residual distortion is twice as large as the estimated uncertainties in the distortion solution ($\sim$0.05 pix; Figure 2.7), and must come from sources of uncertainty that are not accounted for in our analysis. Below we consider two possibilities, time-variable distortion, and the difference between NGSAO and LGSAO observations.

To test the stability of the camera's distortion, we created a distortion solution with data points from 2007, the year with the most data (N=1711). A smoothing

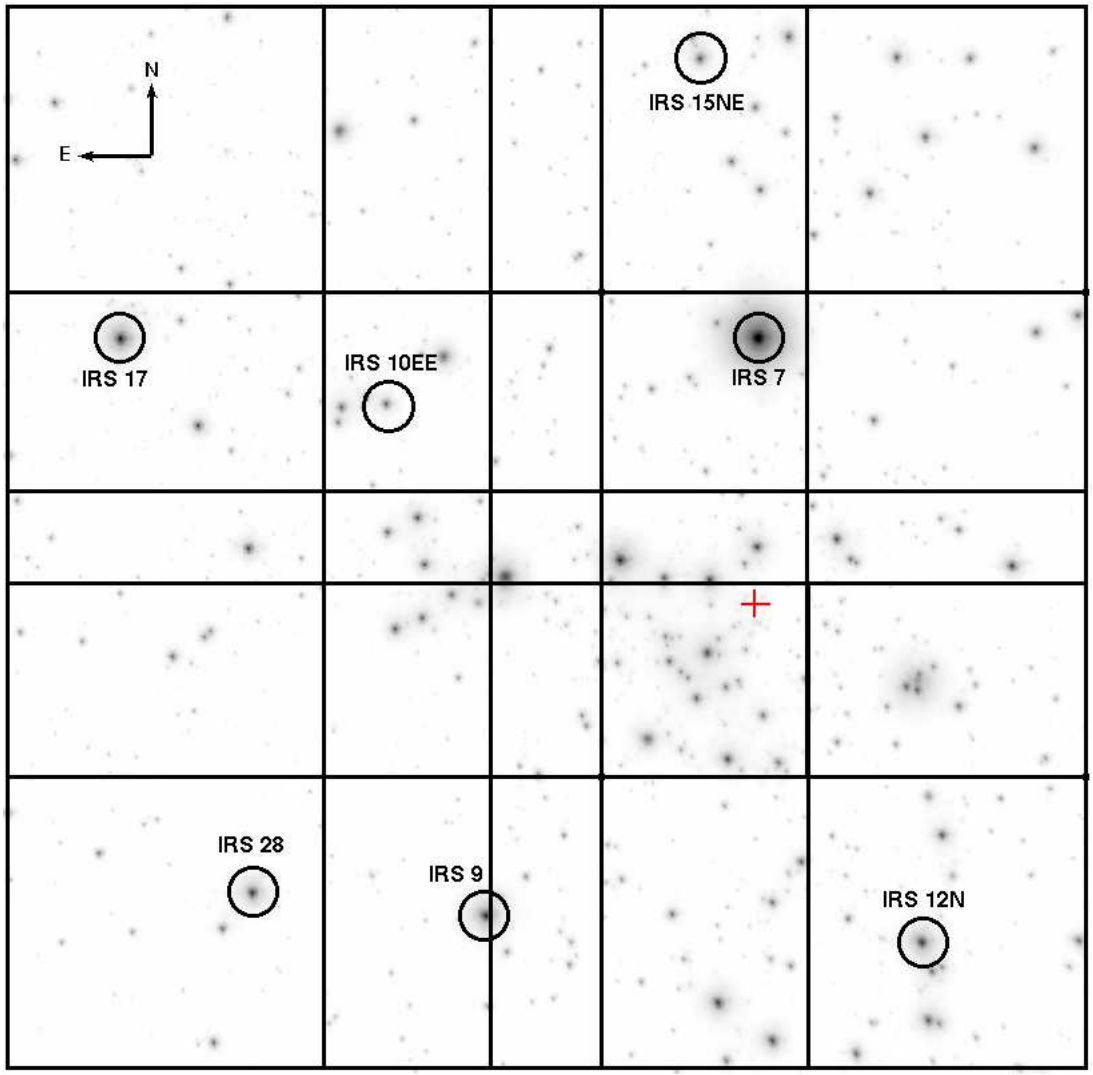

Figure 2.9 NIRC2 K' mosaic image of the Galactic center scaled to show the bright stars. The full field is $22'' \times 22''$. The black boxes show the nine dither positions making up the mosaic, with each box corresponding to the $10'' \times 10''$ NIRC2 field of view. The 7 SiO masers used in the construction of the Sgr A*-radio reference frame are circled, and Sgr A* is marked with a red cross. The four images that make up the SW corner of the mosaic were used in §2.2.2 to determine the quality of the distortion solution.

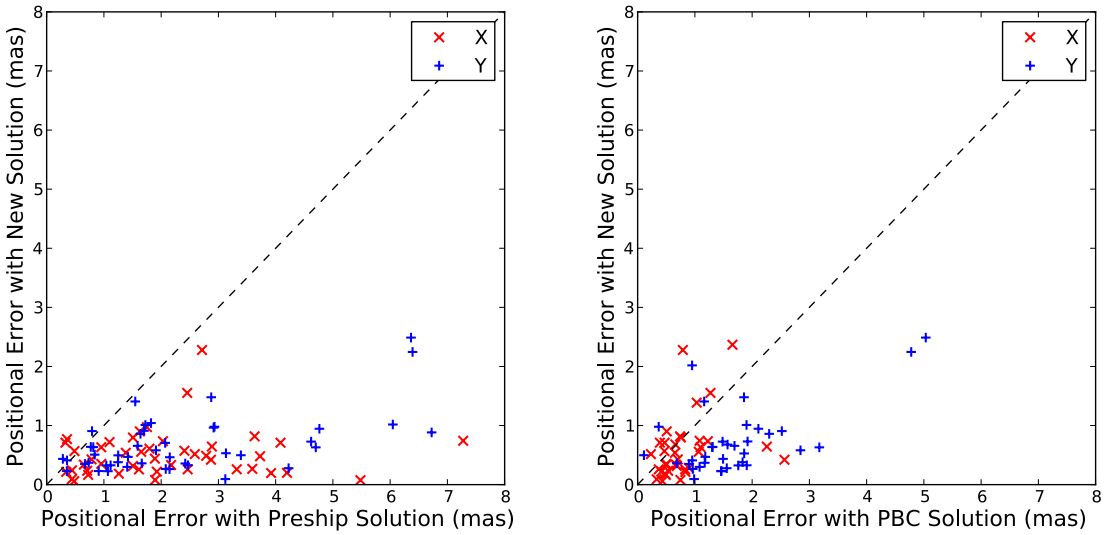

Figure 2.10 Pair-wise analysis on widely-dithered Galactic center data taken in 2008 May. The RMS error of the positional offsets from IRS 16SW-E are plotted. The plots compare the RMS error values from images corrected with the new versus the pre-ship distortion solution (*left*) and the new versus the PBC distortion solution (*right*). The new solution is a factor of ∼3-4 improved in both X (*red crosses*) and Y (*blue plus signs*) over the pre-ship solution and in Y over the PBC solution.

factor of $f = 120$ was used for the spline fitting and was determined in the same manner as our new distortion solution. As the number of data points from each of the years 2008 (N=253) and 2009 (N=489) was not sufficient to make separate distortion solutions for these years, we take the differences between the 2007-only distortion solution and the actual measured data from each of the individual years (see Table 2.1). We find no significant differences (0.05±0.30 pix and 0.09±0.29 pix for 2008 and 2009, respectively), suggesting that the distortion solution is stable within our measurement uncertainties. As a check, comparing the data from 2007 to the 2007-only solution gives an average difference of 0.01±0.22 pix, which has a smaller RMS error since it was the data set used to create the single-year model. Based on this analysis, we conclude that there is no evidence for time-dependent changes.

While we tested our distortion solution on LGSAO data, the model itself was computed using only NGS data, as the six LGS frames from 2008 June were thrown out based on the cuts mentioned in §2.2.1. To test the possibility that the NGS and LGS AO systems have different distortion solutions, we compare Galactic center data taken in both LGS and NGS modes, but otherwise the same setup and in the same night in 2008 May. The data were reduced using the usual data reduction steps (see Ghez et al., 2008), and final LGS- and NGS-only images of the Galactic center were produced. The astrometric precision for each of these images was 0.007 pix (NGS) and 0.012 pix (LGS) for stars with K<15. The NGS image was transformed into the LGS image's coordinate system allowing only for translation between the two frames. Differences between the transformed positions would indicate a possible difference in the distortion between the LGS and NGS observing modes. The RMS difference in the aligned positions, corrected for measurement error bias, is only $(\Delta_x, \Delta_y) = (0.06, 0.05)$ pix (1σ) and is therefore comparable to the error in the distortion model ($\sim$0.05

pix, Figure 2.7). Thus, given the uncertainties in the distortion solution, we do not see a difference in the astrometry from images taken in NGS or LGS mode and conclude that this is a negligible contribution to the residual distortion.

While we have not identified the source of residual distortion, we can functionally include it by adding a constant term of 0.1 pix (1 mas) in quadrature with the error map of the distortion (see §2.2.1) when analyzing astrometric data. We note that while these error terms are important for our localization of Sgr A*-radio in our infrared reference frame (§2.3.1), they do not come into consideration for relative proper motion measurements based on data using similar observational setups.

2.3 Application to the Galactic Center

Here we apply the new geometric optical distortion model and DAR corrections from §2.2.1 to Keck/NIRC2 observations of the Galactic center in order to construct a new IR reference frame (§2.3.1) that is significantly more accurate and stable than those that have been made in the past (§2.3.2). We also measure the motion of the nuclear cluster in this well-defined reference frame and generate a set of secondary infrared astrometric standards that are helpful for doing astrometry over much smaller fields of view (§2.3.3).

2.3.1 Construction of an Infrared, Sgr A*-Radio Rest Frame

Measurements of seven SiO masers that are detectable in the radio and infrared wavelengths are used to transform the IR maser mosaics into a Sgr A*-radio rest frame. At radio wavelengths, each of these masers has well measured positions and velocities with respect to Sgr A* (see, e.g., Reid et al., 2003, 2007). In

this analysis, we use radio positions and proper motions from M. Reid (private communication), who has improved the values compared to what is published in Reid et al. (2007) by adding one more epoch of observations and by applying a correction for the effects of differential nutation. The radio maser positions were propagated using the radio proper motion measurements to create a star list at the epoch of each IR mosaic. Each of the six infrared mosaics was aligned with a four-parameter model (two-dimensional translation, rotation, and a single pixel scale) to the radio maser star list by minimizing the error-weighted net displacements, D, for the masers, where the infrared positional errors include the positional RMS errors (from the 3 subset images; see §2.1.2), as well as errors from the distortion model (see Appendix 2.6). The net displacement and the weighting scheme used are described in Appendix A of Ghez et al. (2008). Errors in the transformation to the Sgr A*-radio rest frame in each epoch were determined using a jack-knife sampling technique, in which one maser at a time is excluded from the alignment. The various sources of error in our astrometry are broken down in Table 2.3. Distortion errors generally dominate the individual IR positional uncertainties of these masers, with the exception of IRS 12N and IRS 28, each of which are in only one pointing and are furthest from the tip-tilt star, where the AO corrections are the poorest. All the transformed IR positions agree with the radio positions to within $\sim 1\sigma$ of each other, suggesting that our uncertainties are well characterized and that we are not missing large systematic error sources.

The NIRC2 pixel scale and orientation values obtained from the SiO maser alignment are similar to those obtained from the M92 study (Table 2.4). We note, however, that the RMS scatter shows a larger variation between the epochs than the uncertainty inferred from the jack-knife analysis of each epoch. We therefore take the RMS values as our estimates of the uncertainties for our average pixel

scale and orientation angle given in Table 2.4. The weighted average NIRC2 plate scale and angle offset from the IR to radio alignments are 9.953 ± 0.002 mas pix^{-1} and 0.249 ± 0.012^o, respectively. We average the results from the two methods (SiO masers and M92) to obtain our final values for the NIRC2 pixel scale and orientation angle, 9.952 ± 0.002 mas pix^{-1} and 0.252 ± 0.009^o, respectively. Thus, 0.252^o must be added to the presumed PA (ROTPOSN - INSTANGL) in order to get the true PA of a NIRC2 image (i.e., the NIRC2 columns must be rotated eastward of North by 0.252^o).

Table 2.3. Measurements of SiO Masers

Star Name	[IR − Radio] Position			Error in Radio		Error in IR Centroid		Error in Alignment		Distortion Error [a]		σ Offset		DAR [b]
	X (mas)	Y (mas)	Total (mas)	X (mas)	Y (mas)	X (mas)	Y (mas)	X (mas)	Y (mas)	X (mas)	Y (mas)	X	Y	(mas)
IRS 9 (Avg)	-1.44	0.31	1.65	0.40	0.67	0.91	1.19	0.78	0.55	1.04	1.05	-0.82	0.13	-2.32
2005 June	-1.54	0.90	1.78	0.30	0.50	0.36	0.62	0.40	0.60	1.04	1.05	-1.27	0.62	-2.95
2006 May	-2.94	1.31	3.22	0.30	0.50	2.94	3.02	1.30	0.60	1.04	1.06	-0.87	0.40	-2.01
2007 August	-1.00	0.17	1.01	0.40	0.60	0.59	1.01	0.50	0.30	1.04	1.05	-0.74	0.11	-1.77
2008 May	-1.60	-0.43	1.66	0.40	0.70	0.48	0.62	0.80	0.70	1.05	1.05	-1.10	-0.27	-1.79
2009 June	-0.99	-0.84	1.30	0.50	0.80	0.86	0.89	0.90	0.50	1.05	1.05	-0.58	-0.50	-2.84
2010 May	-0.54	0.73	0.91	0.50	0.90	0.25	1.00	0.80	0.60	1.05	1.05	-0.38	0.40	-2.54
IRS 7 (Avg)	1.26	-6.61	6.75	5.02	5.03	0.32	0.40	0.28	1.32	1.09	1.07	0.24	-1.24	2.24
2005 June	1.96	-5.27	5.62	5.00	5.00	0.20	0.68	0.40	0.80	1.09	1.07	0.38	-1.01	2.21
2006 May	1.17	-6.85	6.95	5.00	5.00	0.51	0.31	0.30	1.50	1.09	1.07	0.23	-1.28	2.25
2007 August	1.57	-6.35	6.54	5.00	5.00	0.35	0.19	0.30	1.10	1.09	1.07	0.31	-1.21	2.29
2008 May	0.79	-7.89	7.93	5.00	5.00	0.28	0.27	0.20	1.50	1.09	1.07	0.15	-1.48	2.30
2009 June	1.47	-7.08	7.23	5.00	5.10	0.35	0.38	0.30	1.60	1.09	1.07	0.29	-1.30	2.17
2010 May	0.59	-6.22	6.25	5.10	5.10	0.22	0.56	0.20	1.40	1.08	1.07	0.11	-1.15	2.20
IRS 12N (Avg)	-3.46	-3.46	5.17	0.47	0.50	3.35	5.29	1.32	0.95	1.03	1.02	-1.08	-0.87	-2.94
2005 June	-1.81	-5.37	5.67	0.40	0.40	0.72	1.26	0.70	0.80	1.03	1.03	-1.21	-2.89	-2.53
2006 May	-4.64	-1.39	4.84	0.40	0.40	3.81	1.88	2.00	1.10	1.04	1.04	-1.04	-0.57	-3.13
2007 August	-1.30	-0.47	1.38	0.40	0.50	0.30	2.53	0.90	0.60	1.03	1.02	-0.89	-0.17	-3.35
2008 May	-3.35	-5.81	6.71	0.50	0.50	1.82	7.26	1.40	1.20	1.02	1.01	-1.31	-0.78	-3.36
2009 June	-3.99	-3.65	5.41	0.50	0.60	10.51	10.45	1.50	1.00	1.02	1.02	-0.37	-0.35	-2.54
2010 May	-5.70	-4.07	7.00	0.60	0.60	2.95	8.36	1.40	1.00	1.04	1.00	-1.64	-0.48	-2.74
IRS 28 (Avg)	-2.03	6.53	7.23	0.72	0.63	2.11	5.56	0.60	0.62	1.05	1.04	-0.84	1.34	-1.91
2005 June	-3.88	5.57	6.79	0.80	0.70	2.18	0.59	0.50	0.60	1.05	1.04	-1.49	3.69	-3.09
2006 May	-0.66	2.32	2.41	0.70	0.60	1.79	6.35	0.90	0.90	1.06	1.01	-0.28	0.36	-1.33
2007 August	-1.04	-0.54	1.17	0.60	0.50	2.49	1.77	0.30	0.40	1.07	1.03	-0.37	-0.25	-0.84
2008 May	-2.22	5.73	6.15	0.60	0.50	1.17	2.10	0.60	0.70	1.06	1.03	-1.24	2.30	-0.87
2009 June	-1.71	1.99	2.62	0.70	0.70	0.61	2.34	0.60	0.50	1.05	1.04	-1.12	0.74	-2.93
2010 May	-2.66	24.09	24.24	0.90	0.80	4.45	20.22	0.70	0.60	1.04	1.10	-0.57	1.19	-2.37
IRS 10EE (Avg)	0.71	1.75	2.00	0.32	0.38	0.39	0.45	0.40	0.73	1.11	1.03	0.57	1.24	2.03
2005 June	0.75	1.00	1.25	0.20	0.30	0.13	0.90	0.50	0.50	1.11	1.03	0.61	0.67	1.12

Table 2.3—Continued

Star Name	[IR − Radio] Position			Error in Radio		Error in IR Centroid		Error in Alignment		Distortion Error [a]		σ Offset		DAR [b]
	X (mas)	Y (mas)	Total (mas)	X (mas)	Y (mas)	X (mas)	Y (mas)	X (mas)	Y (mas)	X (mas)	Y (mas)	X	Y	(mas)
2006 May	-0.17	2.63	2.64	0.30	0.30	0.99	0.29	0.30	0.70	1.11	1.04	-0.11	2.00	2.46
2007 August	0.12	1.94	1.94	0.30	0.40	0.43	0.32	0.40	0.70	1.10	1.04	0.09	1.44	2.89
2008 May	1.19	1.01	1.56	0.30	0.40	0.31	0.14	0.50	0.80	1.10	1.04	0.93	0.73	2.88
2009 June	1.13	1.72	2.06	0.40	0.40	0.33	0.44	0.40	0.80	1.11	1.04	0.88	1.20	1.20
2010 May	1.27	2.18	2.52	0.40	0.50	0.19	0.60	0.30	0.90	1.11	1.03	1.03	1.38	1.64
IRS 15NE (Avg)	1.93	4.55	5.06	0.40	0.50	0.50	0.68	0.52	1.58	1.12	1.11	1.40	2.10	4.62
2005 June	2.89	3.25	4.35	0.30	0.40	0.41	0.34	0.60	1.00	1.11	1.11	2.12	2.05	4.42
2006 May	2.41	2.69	3.61	0.30	0.40	0.09	0.62	0.60	1.80	1.12	1.11	1.84	1.20	4.70
2007 August	1.95	4.11	4.55	0.40	0.50	0.49	0.73	0.50	1.30	1.11	1.12	1.42	2.13	4.85
2008 May	1.80	5.32	5.62	0.40	0.50	0.10	0.23	0.50	1.80	1.11	1.11	1.40	2.43	4.86
2009 June	1.63	5.66	5.89	0.50	0.60	0.61	0.72	0.50	1.90	1.12	1.11	1.12	2.37	4.37
2010 May	0.91	6.27	6.34	0.50	0.60	1.28	1.44	0.40	1.70	1.12	1.11	0.50	2.45	4.48
IRS 17 (Avg)	-0.85	0.34	1.54	4.52	2.35	0.51	0.46	0.83	0.53	1.12	1.04	-0.17	0.21	2.82
2005 June	-0.12	0.97	0.98	3.20	1.60	0.39	0.05	0.80	0.40	1.13	1.04	-0.03	0.50	1.27
2006 May	-0.48	1.57	1.64	3.50	1.80	1.00	0.45	0.80	0.60	1.12	1.04	-0.12	0.71	3.55
2007 August	-1.55	1.37	2.07	4.10	2.10	0.70	0.58	0.70	0.50	1.13	1.05	-0.36	0.56	4.28
2008 May	-0.35	0.00	0.35	4.60	2.40	0.18	0.28	1.00	0.50	1.12	1.04	-0.07	0.00	4.26
2009 June	-1.77	0.35	1.80	5.50	2.90	0.16	0.38	0.90	0.50	1.12	1.04	-0.31	0.11	1.41
2010 May	-0.86	-2.23	2.39	6.20	3.30	0.63	1.01	0.80	0.70	1.12	1.04	-0.13	-0.61	2.16

[a]Distortion error includes the residual distortion term described in the text.

[b]Differential Atmospheric Refraction relative to the center of the image

Table 2.4. NIRC2 Plate Scale and Orientation

Method	Plate Scale (mas pix^{-1})	Orientation (deg)
Calibrated w.r.t. ACS observations of M92[a]	9.950 ± 0.003 ± 0.001	0.254 ± 0.014 ± 0.002
2007 June	9.948 ± 0.001 ± 0.001	0.249 ± 0.006 ± 0.002
2007 July	9.948 ± 0.001 ± 0.001	0.256 ± 0.006 ± 0.002
2008 April	9.946 ± 0.007 ± 0.001	0.276 ± 0.030 ± 0.002
2008 June	9.952 ± 0.003 ± 0.001	0.270 ± 0.009 ± 0.002
2008 July	9.951 ± 0.002 ± 0.001	0.248 ± 0.004 ± 0.002
2009 May	9.949 ± 0.002 ± 0.001	0.282 ± 0.013 ± 0.002
Calibrated w.r.t. VLA observations of GC Masers[a]	9.953 ± 0.002	0.249 ± 0.012
2005 June	9.952 ± 0.001	0.237 ± 0.003
2006 May	9.955 ± 0.001	0.248 ± 0.007
2007 August	9.950 ± 0.001	0.253 ± 0.003
2008 May	9.954 ± 0.001	0.271 ± 0.005
2009 June	9.952 ± 0.001	0.253 ± 0.005
2010 May	9.955 ± 0.001	0.253 ± 0.005
Final Value[b]	9.952±0.002	0.252±0.009

Note. — Statistical (first) and absolute (second) uncertainties are shown for the ACS observations (see §2.1.1).

[a]Weighted averages are taken for the final values for each method. We use the more conservative RMS errors as the uncertainties on these values.

[b]Average of each method's weighted average (see Note a).

Our transformed IR positions from the mosaic images provide a calibrated astrometric reference frame in which Sgr A* is at rest at the origin. Comparison of the SiO masers as measured in the IR and radio provide estimates of how well we can localize the position and velocity of Sgr A*-radio within this reference frame. For each maser, a linear motion model is obtained by fitting a line to the star's transformed infrared positions as a function of time. In this initial step, the positional uncertainties include only the centroiding and alignment errors; the distortion uncertainty (see Appendix 2.6) is omitted here, since it is correlated across all epochs. Furthermore, the model fit is calculated with respect to $T_{0,IR}$, which is the average time of the IR positional measurements, weighted by the average of the X and Y positional uncertainties. Figures 2.11 and 2.12 show the

resulting fits, which have an average reduced χ^2 value of 0.62 (see Table 2.5), and the uncertainties in the resulting fit parameters were determined from the covariance matrix. In these figures, and in all other cases, X and Y increase to the east and north, respectively. While the reduced χ^2 values suggest that the uncertainties may be overestimated (possibly due to IRS 7; see Appendix 2.7), we err on the conservative side and do not re-scale our positional measurements. The velocities measured in the infrared are statistically consistent with the radio proper motion values[7]. Based on the weighted average of the velocity differences between the infrared and radio reference frames, we conclude that Sgr A* is at rest to within $\sim$0.09 mas yr^{-1} (compared to $\sim$0.03 mas yr^{-1} in the radio reference frame).

While increasing the time baseline and depth of the infrared measurements will improve upon this precision, we note that four out of 14 one-dimensional relative velocity measurements are already limited by the radio measurements. Further improvements in the radio will ultimately be required to create a reference frame that is more stable than 0.03 mas yr^{-1} (the current limits from the radio measurements alone).

In order to compare the IR and radio positional measurements, two additional steps are required. First we determine the time, $T_{0,(IR+radio)}$, at which the positional difference is expected to have the smallest uncertainty for each maser,

$$T_{0,(IR+radio)} = \frac{\sigma_{v,IR}^2 T_{0,IR} + \sigma_{v,radio}^2 T_{0,radio}}{\sigma_{v,IR}^2 + \sigma_{v,radio}^2} \tag{2.3}$$

where $\sigma_{v,IR}$ and $\sigma_{v,radio}$ are the velocity errors in the IR and radio, respectively. We take the average of these seven times, 2006.9, and find the IR and radio

[7]We note that using the latest radio values reduces the uncertainty in tying the IR and radio measurements, reported in Table 2.5, by 40% compared to the same analysis carried out using the radio values from Reid et al. (2007).

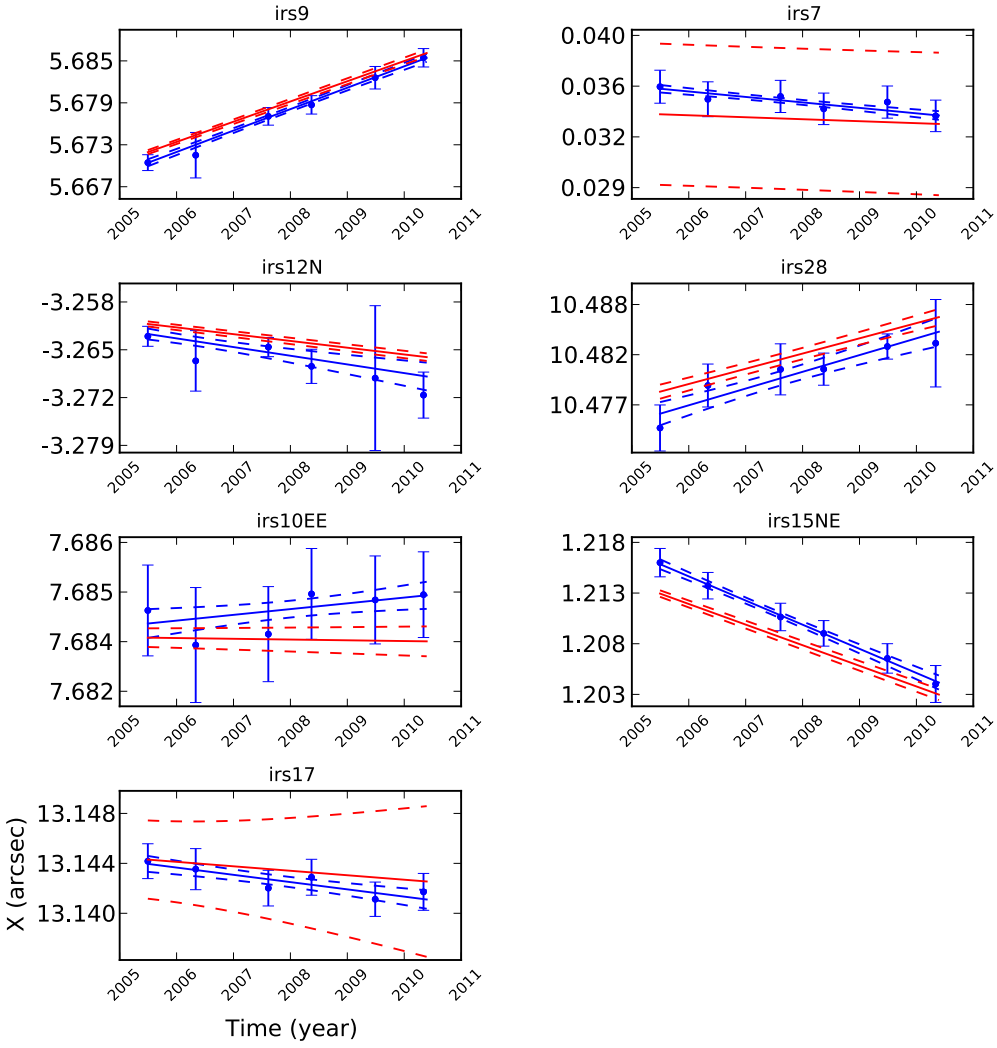

Figure 2.11 Absolute X positions (where X increases to the east) of Galactic center SiO masers in the infrared as a function of time and the velocity model fit (*blue*) and the proper motion model for the radio (*red*). The 1σ errors on the line fits are shown as dashed lines. The IR positional errors shown include centroiding and alignment errors. Radio proper motion measurements are taken from M. Reid (private communication).

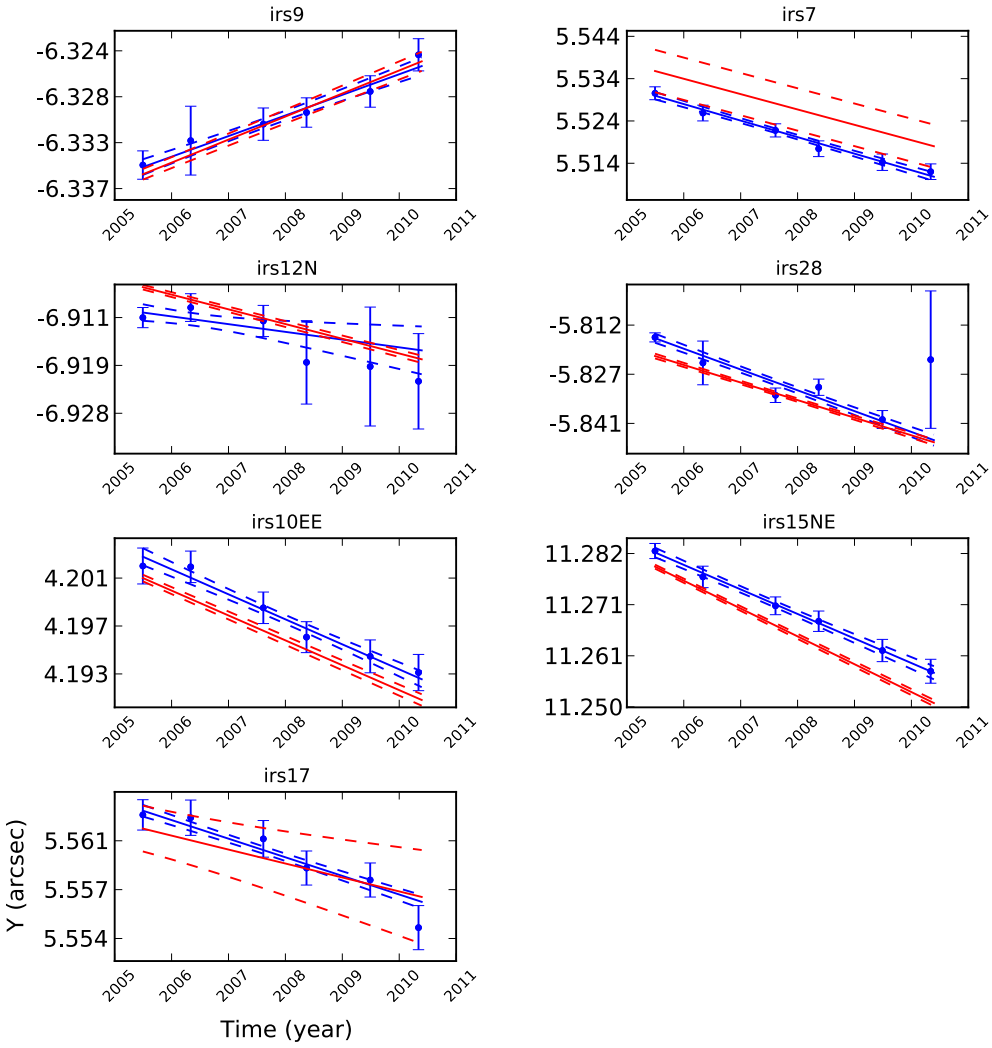

Figure 2.12 Same as Figure 2.11 but for Y positions (where Y increases to the north).

Table 2.5. Astrometry of SiO Masers

Maser	K (mag)	$\tilde{\chi}^{2}$ [a]	IR T_0 (year)	IR + Radio T_0 [b] (year)	[IR - Radio] X [c] (mas)	[IR - Radio] Y [c] (mas)	[IR - Radio] V_X (mas yr^{-1})	[IR - Radio] V_Y (mas yr^{-1})
IRS 9	9.063	0.29	2007.7	2007.2	-1.32 ± 1.11 ± 0.34	0.35 ± 1.17 ± 0.57	0.18 ± 0.18 ± 0.08	-0.23 ± 0.26 ± 0.14
IRS 7	7.658	0.68	2007.7	2007.2	1.46 ± 1.11 ± 5.00	-6.24 ± 1.22 ± 5.00	-0.25 ± 0.09 ± 0.22	-0.28 ± 0.31 ± 0.30
IRS 12N	9.538	0.60	2006.4	2006.4	-1.88 ± 1.26 ± 0.42	-2.74 ± 1.59 ± 0.47	-0.28 ± 0.49 ± 0.05	1.24 ± 1.03 ± 0.06
IRS 28	9.328	1.19	2007.6	2007.6	-2.12 ± 1.34 ± 0.62	3.93 ± 1.41 ± 0.52	0.16 ± 0.47 ± 0.22	-0.95 ± 0.49 ± 0.24
IRS 10EE	11.270	0.64	2008.1	2007.7	0.62 ± 1.14 ± 0.29	1.75 ± 1.13 ± 0.32	0.17 ± 0.12 ± 0.04	-0.01 ± 0.24 ± 0.05
IRS 15NE	10.198	0.06	2007.4	2007.1	2.31 ± 1.16 ± 0.36	3.90 ± 1.31 ± 0.47	-0.33 ± 0.20 ± 0.05	0.68 ± 0.39 ± 0.06
IRS 17	8.910	0.90	2007.7	2005.1	-0.68 ± 1.22 ± 3.72	0.80 ± 1.08 ± 1.91	-0.23 ± 0.24 ± 0.99	-0.33 ± 0.15 ± 0.54
Weighted Average [d]		0.62		2006.9	-0.31 ± 0.55	1.44 ± 0.59	0.02 ± 0.09	-0.06 ± 0.14

Note. — Infrared (first) and radio (second) formal uncertainties are reported for each maser's position and velocity. Average distortion errors ($\sigma \sim$1 mas) for each maser are added in quadrature to the infrared formal uncertainties. X and Y increase to the east and north, respectively.

[a] $\tilde{\chi}^2$ is the average of the X and Y χ^2 per degree of freedom.

[b] Average T_0 from both IR and radio measurements weighted by velocity errors (see Equation 2.3).

[c] Positional offsets computed for the common epoch of 2006.9.

[d] Weighted average and error in the weighted average are reported for all columns except the $\tilde{\chi}^2$ and T_0 columns, where we report the average.

positions and uncertainties at this common epoch. Then the correlated distortion error (including both the uncertainty in the model and the residual distortion, $\sim$0.1 pix) for each maser is added in quadrature to the formal uncertainty from the infrared fit. Comparison with the radio positions indicates that the position of Sgr A*-radio is known to within $\sim$0.57 mas in year 2006.9 in our infrared reference frame. We note that the localization of Sgr A*-radio in the IR reference frame is time-dependent (Figure 2.13). Decreasing the impact of uncertainties in the IR distortion model, with either more highly dithered measurements or a better distortion model, would improve this precision. Overall, our current measurement uncertainties for both the position and velocity of Sgr A* are a factor of 3-4 better than earlier measurements - either those of Ghez et al. (2008), when treated in the same manner[8], or those reported by Gillessen et al. (2009b) using their "maser system" method, which is comparable to the method used here[9].

Sgr A* is detected in three of the IR maser mosaics and its position is consistent with Sgr A*-radio in our IR reference frame (Figure 2.13). In 2008 May, Sgr A* was as bright as K=14.8 mag, which is one of the brightest IR detections of Sgr A* (see e.g., Do et al., 2009b; Sabha et al., 2010). In 2009 June and 2010 May, it was detected with K=16.4 and K=15.3, respectively. The magnitude of Sgr A* in 2009 is more in line with the faint end of what is observed for this highly variable source. The later detections were possible because the mosaics were deeper than the previous mosaics. No other mosaics show Sgr A* since these observations are composed of very short exposures to avoid saturation on the infrared-bright SiO masers. Figure 2.13 shows that all three detections

[8]We reported errors from a half-sample bootstrap in Ghez et al. (2008). To compare values we reran our analysis with the half-sample bootstrap, which overestimates the uncertainties since half the sample is removed.

[9]We note that Gillessen et al. (2009b) derive their astrometry using two distinct methods, and adopted the positional errors from one method (the "cluster system") and velocity errors from the second method (the "maser system").

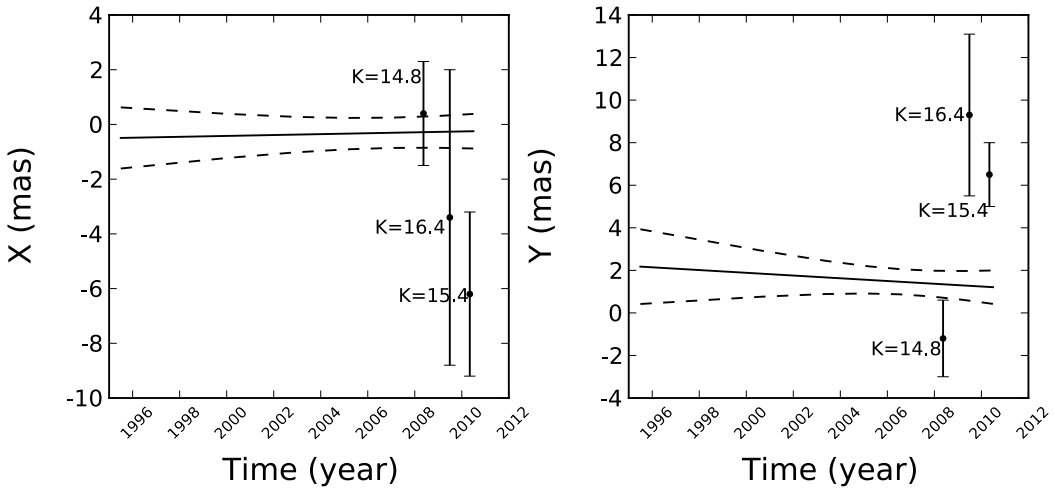

Figure 2.13 Position of Sgr A*-radio versus time in the IR reference frame based on analysis in §2.3.1 and values in Table 2.5 (dotted lines show 1σ uncertainties). Detected positions of Sgr A* in the infrared maser mosaics from 2008 May, 2009 June, and 2010 May are overplotted along with the magnitude of Sgr A*-IR. We note that the fainter detections may suffer from larger astrometric biases from underlying sources. Nonetheless, all three IR positions agree with the radio position of Sgr A*. In the IR reference frame, Sgr A*-radio is consistent with being at rest, at the origin.

are consistent within 3σ in X and Y with the position of Sgr A*-radio in the IR reference frame. Furthermore, the IR position is more consistent with the radio position (within 1σ) when Sgr A*-IR is in a relatively bright state and less prone to astrometric biases from underlying sources (e.g., Ghez et al., 2008; Gillessen et al., 2009b). This independent comparison confirms that we have a well constructed reference frame.

By carrying out the same analysis in polar coordinates (as opposed to cartesian), we find that the infrared and radio Sgr A*-rest coordinate systems show no net relative expansion (V_r) nor rotation (V_t/R) to within 0.12 mas yr^{-1} and 0.11 mas yr^{-1} arcsec^{-1} (1σ), respectively (Table 2.6).

2.3.2 Comparison of Sgr A*-Rest Reference Frame vs. Cluster-Rest Reference Frame

The Sgr A*-rest reference frame generated in §2.3.1 is more stable than the cluster-rest reference frame that has been used as the principle coordinate system for all previous proper motion studies. Here we are quantifying frame stability as the uncertainty in the velocity of the object that is defined to be at rest. Since the cluster-rest frame previously used is defined by assuming that a set of reference stars has no net motion, the translational stability of this reference frame is limited to be $\sigma/\sqrt{N}$, where σ is the intrinsic dispersion of the stars and N is the number of reference stars used. With a dispersion in the plane of the sky of roughly 2.6 mas yr^{-1} (Trippe et al., 2008; Schödel et al., 2009, see also §2.3.3), $\sim$850 reference stars would be needed in order to match the stability of our current Sgr A*-rest frame. This is a factor of $\sim$2 to 10 more than have been used in earlier studies (e.g., Trippe et al., 2008; Ghez et al., 2008; Lu et al., 2009; Gillessen et al., 2009b; Schödel et al., 2009).

Table 2.6. Astrometry of SiO Masers (Polar Coordinates)

Maser	R^a (arcsec)	[IR - Radio] Rad Velocity (mas yr^{-1})	[IR - Radio] Tan Velocity (mas yr^{-1})	[IR - Radio] Ang Velocity (mas yr^{-1} arcsec^{-1})
IRS 9	8.503	0.29 ± 0.23 ± 0.12	0.02 ± 0.22 ± 0.11	0.00 ± 0.22 ± 0.11
IRS 7	5.524	-0.28 ± 0.31 ± 0.30	-0.25 ± 0.09 ± 0.22	-0.04 ± 0.09 ± 0.22
IRS 12N	7.644	-1.00 ± 0.96 ± 0.06	0.78 ± 0.62 ± 0.05	0.10 ± 0.62 ± 0.05
IRS 28	11.989	0.60 ± 0.47 ± 0.22	0.75 ± 0.48 ± 0.24	0.06 ± 0.48 ± 0.24
IRS 10EE	8.757	0.15 ± 0.16 ± 0.04	0.09 ± 0.21 ± 0.05	0.01 ± 0.21 ± 0.05
IRS 15NE	11.340	0.64 ± 0.39 ± 0.06	-0.40 ± 0.20 ± 0.05	-0.04 ± 0.20 ± 0.05
IRS 17	14.271	-0.34 ± 0.23 ± 0.94	0.21 ± 0.17 ± 0.63	0.01 ± 0.17 ± 0.63
Weighted Average[b]		0.19 ± 0.12	-0.07 ± 0.11	-0.01 ± 0.11

Note. — Infrared (first) and radio (second) formal uncertainties are reported for each maser's position and velocity.

[a]Position reported for the common IR + radio epoch given in Table 2.5 for each maser, and using proper motions measured in the infrared.

[b]Weighted average and error in the weighted average are reported.

The stability of reference frames for observations made with fields of view that are too small to tie into the masers directly can be significantly improved by using secondary astrometric standards generated by the proper motion measurements for infrared stars other than the masers from the measurements presented in §2.3.1. To create these secondary standards, we use the same linear motion modeling done for the masers and estimate the positions and proper motions of stars that are detected in at least four of the 6 maser mosaics (N=1445). These stars have K' magnitudes that are brighter than 16 mag and a χ^2 distribution that is consistent with their positional uncertainties and degrees of freedom (Figure 2.14). From these, we select the 1279 stars that have velocities less than 10 mas yr^{-1} (to exclude mismatches) and velocity errors less than 1.5 mas yr^{-1} in both the X and Y directions (Figure 2.15). The positions and proper motions of these stars are reported in Table 2.7, and the left panel of Figure 2.16 shows the cumulative distribution as a function of radius for the entire sample, as well as for those known to be old and young. Reference frames defined based on these secondary astrometric standards (which can be young or old), as opposed to one defined on the premise that the old stars have no net motion, are significantly more stable, and the exact advantage depends on the field coverage; for the Keck speckle and $10''\times10''$ AO data (see, e.g., Ghez et al., 2008; Lu et al., 2009), the translational stability is expected to be a factor of 17.5 and 12.5 times better, or 0.03 and 0.02 mas yr^{-1}, respectively (see right panel of Figure 2.16). Similarly the rotational stability, quantified as the uncertainty in the average rotational velocity, is expected to be a factor of 20 and 9 times better, for the Keck speckle and AO data, or roughly 0.03 and 0.02 mas yr^{-1} arcsec^{-1}, respectively. This improvement has been seen and will be presented in a separate forthcoming paper (see also Yelda et al., 2010, conference proceedings showing these results).

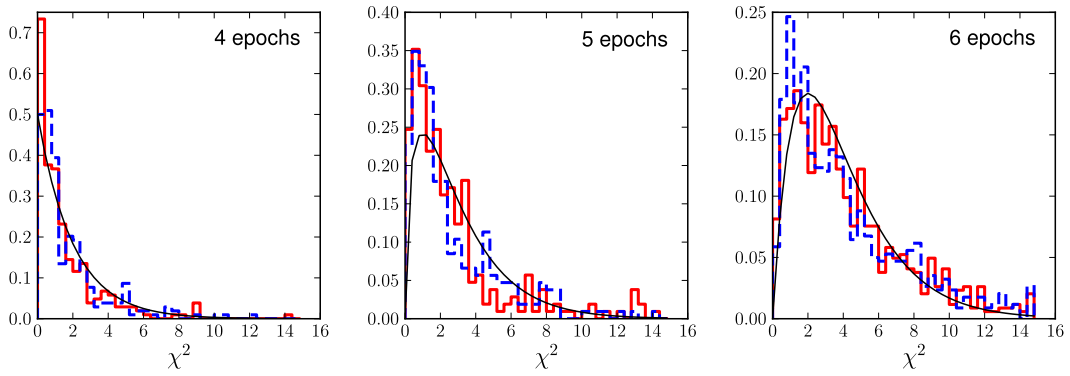

Figure 2.14 Histogram of velocity χ^2 values in X (*solid red*) and Y (*dashed blue*) for the stars detected in four (N=263), five (N=269), and six (N=912) maser mosaics. The theoretical χ^2 distributions for the corresponding degrees of freedom are overplotted as thin black curves for comparison. We find that the velocities are well-behaved, as indicated by the similarity between the observed and theoretical distributions.

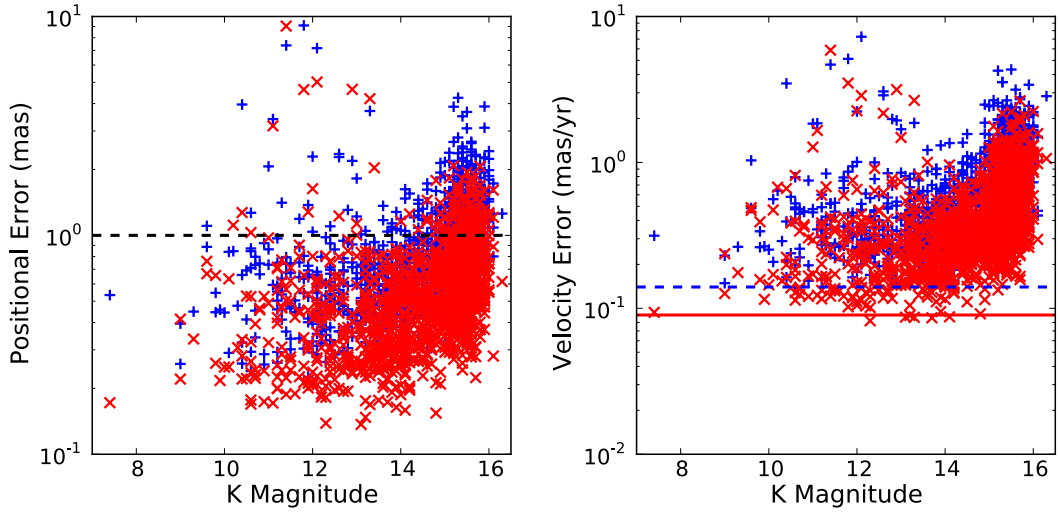

Figure 2.15 Positional (*left*) and velocity uncertainties (*right*) for X (*red crosses*) and Y (*blue plus signs*) versus K magnitude for all stars detected in at least four of the six maser mosaics (N=1445). We select stars with velocities less than 10 mas yr^{-1} and velocity errors less than 1.5 mas yr^{-1} in both the X and Y directions as our infrared astrometric standards, resulting in a total of 1279 stars. The dashed line in the left-hand plot shows the level of residual distortion (1 mas) which is added in quadrature to the positional errors in Table 2.7. The dashed lines in the right plot indicate the level at which the velocity of Sgr A* is known in the X (*solid red*) and Y directions (*dashed blue*), based on the IR to radio offsets of the masers found in §2.3.1 and Table 2.5.

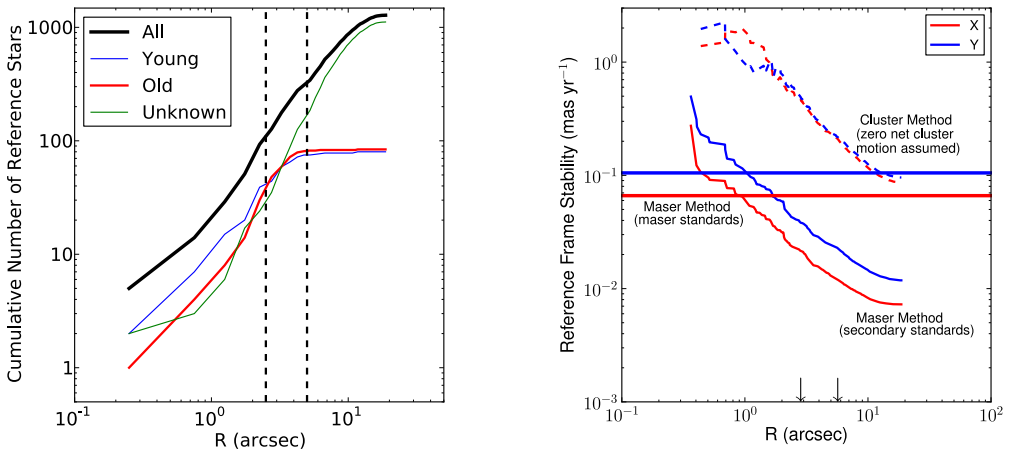

Figure 2.16 *(Left)* Cumulative radial distribution of all 1279 astrometric reference stars (*black*), as well as the distribution of stars based on spectral identification: young (N=77; *blue*), old (N=73; *red*), and unknown (N=1129; *green*). The field of view for both the speckle (R=2.5″) and the adaptive optics (R=5″) cameras are indicated (*dashed lines*). The speckle data (1995-2005) are dominated by young stars, and thus, using them as reference stars in the coordinate transformations is critical. Stars with unknown spectroscopic identifications dominate at larger radii. *(Right)* Error on the weighted average velocity of the cluster stars in X (*red*) and Y (*blue*) as a function of distance from Sgr A* as measured using two distinct methods. The curves show the improvement in the errors as more reference stars are included at larger radii. Using the 'cluster method' and excluding young stars (*dashed curves*), the assumption of no net cluster motion is made, resulting in a reference frame that is stable to ∼0.2 mas yr^{-1} at a radius of 5″ (corresponding to the field of view of Keck AO data). In a reference frame where Sgr A* is at rest, the 'maser method', the error on the weighted average velocity of the cluster stars is ∼0.02 mas yr^{-1} over the extent covered by the AO data (*solid curves*). The total error in the weighted average velocity from the method described in §2.3.2, which includes contributions from the cluster stars, as well as the masers in both the radio and infrared (*horizontal lines*), represents the stability of our reference frame (0.09 mas yr^{-1}).

Table 2.7. Galactic Center Secondary IR Astrometric Standards

Name	K' (mag)	$T_{0,IR}$ (year)	Radius (arcsec)	Δ R.A. (arcsec)	$\sigma_{R.A.}$[a] (mas)	Δ Dec. (arcsec)	σ_{Dec}[a] (mas)	v_{RA}[b] (mas yr^{-1})	v_{Dec}[b] (mas yr^{-1})
S0-3	14.8	2008.67	0.36	0.3351	1.4	0.1189	1.4	9.1 ± 0.3	-0.9 ± 0.5
S0-6	14.2	2008.43	0.36	0.0276	1.1	-0.3625	1.2	-5.3 ± 0.1	3.5 ± 0.4
S0-53	15.5	2005.89	0.40	0.3484	1.6	0.2037	1.4	-8.1 ± 1.1	7.5 ± 0.5

Note. — Table 2.7 is published in its entirety in the electronic version of Yelda et al. (2010).

[a]Positional errors include centroiding, alignment, and residual distortion (1 mas) errors, but do not include error in position of Sgr A* (0.55 mas, 0.59 mas in RA and Dec, respectively).

[b]Velocity errors do not include error in velocity of Sgr A* (0.09 mas yr^{-1}, 0.14 mas yr^{-1} in RA and Dec, respectively).

2.3.3 Motion of the Central Stellar Cluster in a Sgr A* Rest Frame

The proper motions for the secondary astrometric standards listed in Table 2.7 also offer the first opportunity to study the kinematic properties of the central stellar cluster directly in a Sgr A*-rest frame. Since all previous proper motions have been made in the cluster-rest reference frame, any net rotation of the cluster in the plane of the sky is removed from these earlier measurements. Rotationally, we find no motion in the plane of the sky in the tangential velocities (-0.09 $\pm$ 0.14 mas yr^{-1}) nor in the angular velocities (0.26 $\pm$ 0.36 mas yr^{-1} arcsec^{-1}) about Sgr A* (Figure 2.17). However, we do detect rotation in the plane of the Galaxy, as has been previously reported by both Trippe et al. (2008) and Schödel et al. (2009) and is shown in Figure 2.18, which shows that there is a preferred angle for the proper motion vectors of $25.4^o \pm 16.3^o$, consistent with the angle of the Galactic plane (31.4^o; Reid & Brunthaler, 2004). This rotation in the Galactic plane is also seen in the flattening of the distribution of velocities in the direction parallel to the Galactic plane as compared to the velocities in the perpendicular direction (Figure 2.19). Translationally, we find that the weighted average velocity of all the stars in the sample that are not known to be young (N=1202) is 0.21 $\pm$ 0.13 mas yr^{-1} ($\sim$8.0 $\pm$ 4.9 km s^{-1} at 8 kpc) and 0.13 $\pm$ 0.14 mas yr^{-1} ($\sim$4.9 $\pm$ 5.3 km s^{-1}) in the X and Y directions (where X and Y increase to the east and north), respectively. Figure 2.20 compares the mean translational motion of the nuclear stellar cluster to the motion of Sgr A* (as determined in §2.3.1) and shows that there is no relative motion between the cluster and the black hole. The uncertainties quoted here are the RMS errors of the weighted average velocities from a bootstrap analysis with 10^5 trials, where in each trial a random set of data was sampled (with replacement) from the observed cluster velocity distribution.

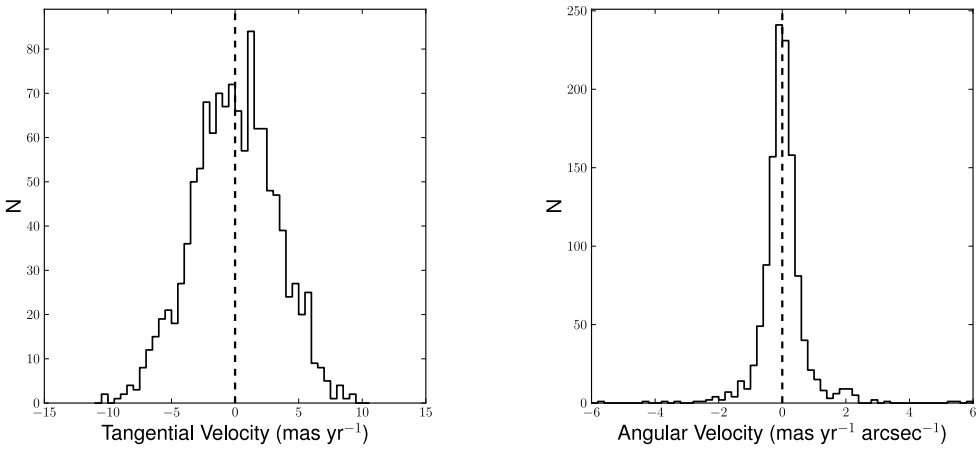

Figure 2.17 (*Left*) Histogram of tangential velocities of the astrometric reference stars (excluding known young stars). The tangential motion in the plane of the sky is consistent with zero mas yr^{-1} (*dashed line*). (*Right*) Histogram of angular velocities of the reference stars (excluding known young stars). The angular velocity is consistent with zero mas yr^{-1} (*dashed line*).

2.4 Summary & Conclusions

We have improved upon existing geometric distortion solutions for the NIRC2 camera at the W. M. Keck II telescope and have, for the first time, implemented DAR corrections to our Galactic center astrometry. In all tests that were performed, the new distortion solution shows an improvement by a factor of ∼2-4 over existing solutions. We take as our final residuals: (σ_x, σ_y) ∼ (0.11, 0.10) pix ∼ (1.1, 1.0) mas. This is the error that is incurred when combining images taken at various offsets and position angles. The transformations between the ACS/WFC and NIRC2 reference frames yield a consistent plate scale and angle offset to that obtained using Galactic center infrared data which are tied to the radio reference frame. We find an average plate scale and angle offset for the NIRC2 narrow camera of 9.952 ± 0.002 mas pix^{-1} and 0.252 ± 0.009^o, respectively.

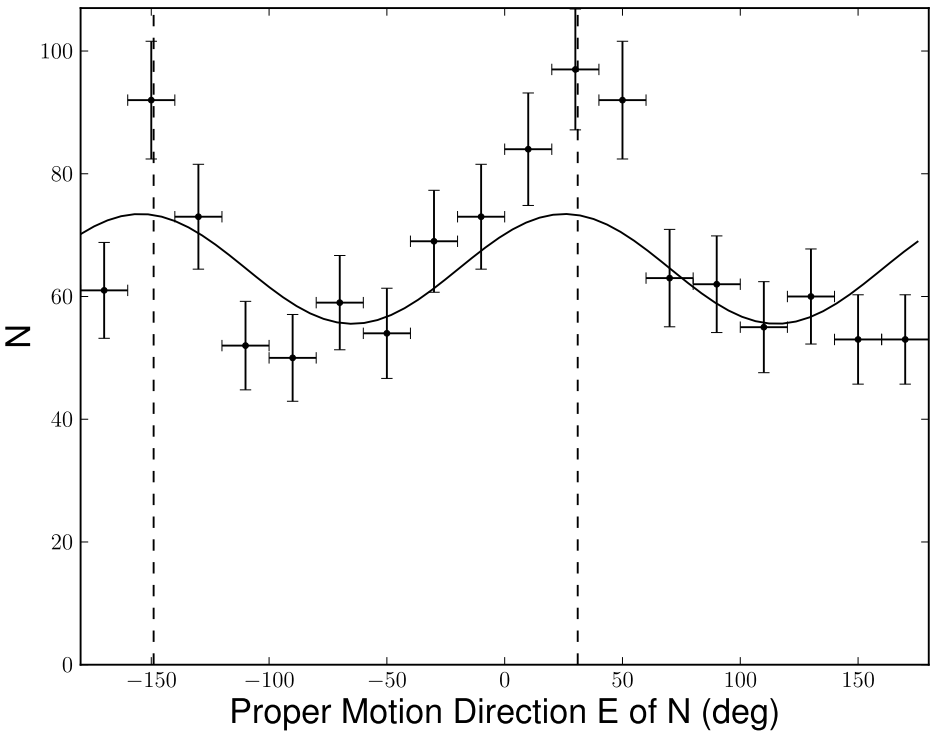

Figure 2.18 Histogram of proper motion direction, defined as the angle east of north, of the infrared astrometric standards in the central ∼1 pc. The vertical error bars are Poisson errors, while the horizontal bars denote the width of the histogram bins. The angle of the Galactic plane is shown as the dashed line (∼31^o and 180^o opposite). The data are best fit with a cosine curve which peaks at 25.4^o ± 16.3^o, which is consistent with the angle of the Galactic plane.

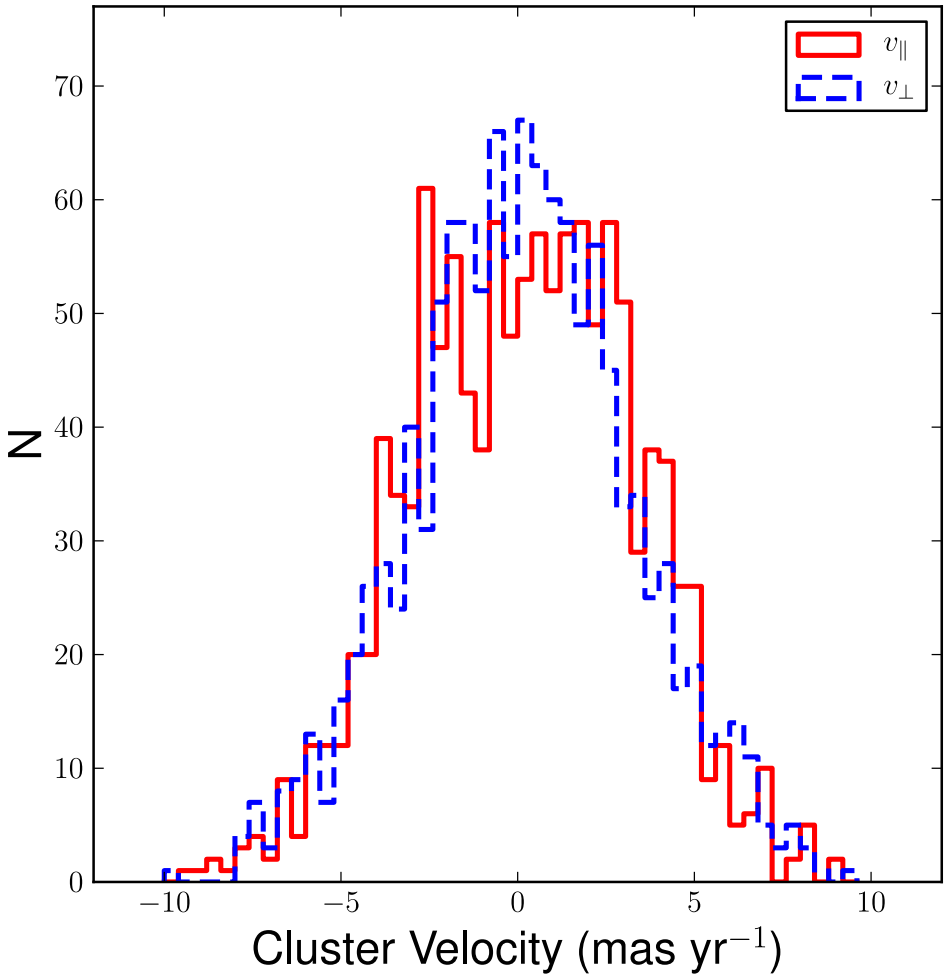

Figure 2.19 (*Left*) Reference star velocities parallel (*solid red*) and perpendicular (*dashed red*) to the Galactic plane ($\theta = 31.4^o$). The flattening of the $v_{\parallel}$ distribution is due to the rotation of the cluster stars along the Galactic plane.

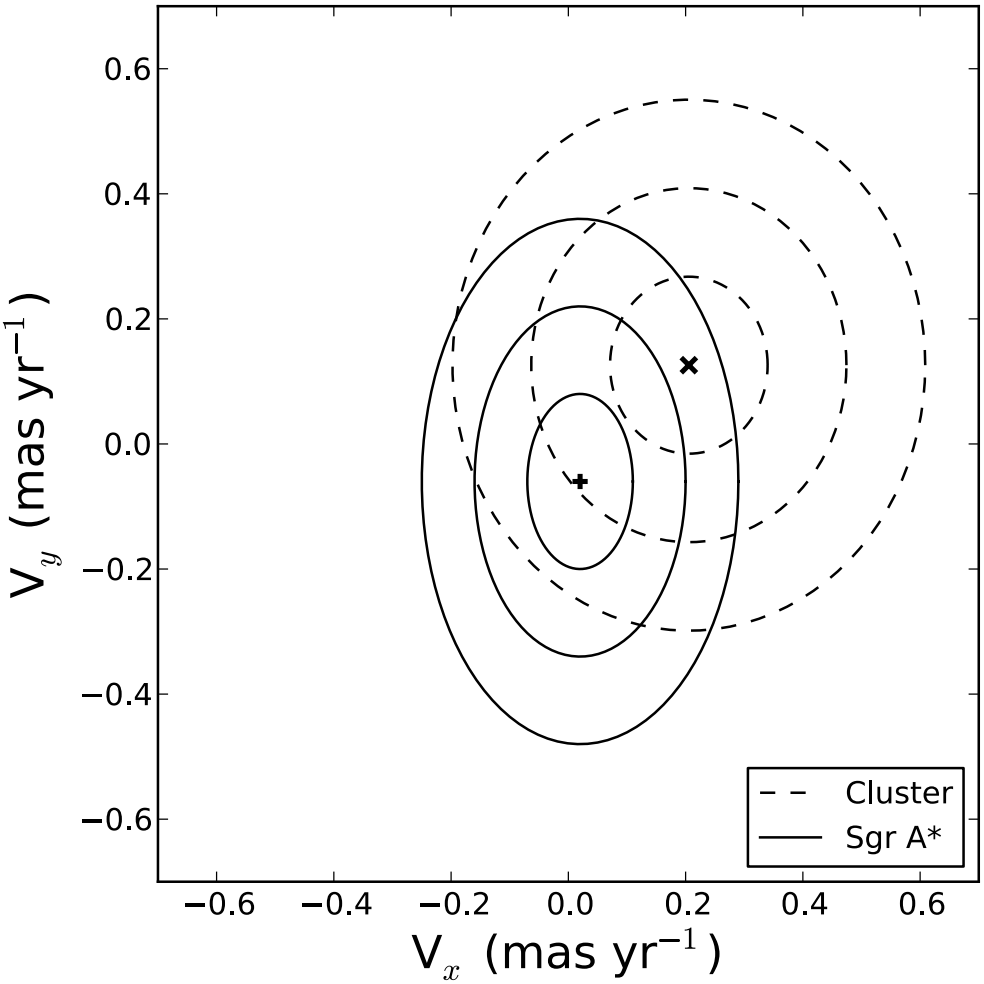

Figure 2.20 Velocity of Sgr A* in the infrared reference frame (*plus sign*) with 1, 2, and 3σ contours shown (*solid curves*), as compared to the cluster's weighted average velocity (*cross; dashed curves*). V_x and V_y are defined such that positive values are motions that increase in the east and north directions, respectively.

The new distortion solution and its associated uncertainty, in the form of FITS files, may be obtained at `http://www.astro.ucla.edu/~ghezgroup/distortion`. The FITS files, or look-up tables, may be fed into the IRAF routine *Drizzle* during the data reduction process. The values in the look-up tables specify the shifts required to put an image into a "distortion-free" reference frame.

As a result of the work presented here, Galactic center astrometry can now be tied to a Sgr A*-radio rest frame to better than $\sim$0.6 mas and $\sim$0.1 mas yr^{-1} ($\sim$3.5 km s^{-1} at 8 kpc) in position and velocity space, respectively, which is a factor of 3 improvement over earlier reported efforts. We note that the velocity of Sgr A* along the line of sight is likely to be minimal ($\sim$3.5 km s^{-1}, 1σ) given the constraints on the motion in the plane of the sky. Since the cluster has been found to exhibit no net motion with respect to the local standard of rest (LSR) to within $\pm$5 km s^{-1} (Figer et al., 2003; Trippe et al., 2008), this adds confidence in the estimates of the distance to the Galactic center (R_o) from orbital analyses in which the black hole is assumed to have no line of sight motion with respect to the LSR. With this assumption, R_o estimates from comparable orbital analyses in Ghez et al. (2008), Gillessen et al. (2009a) and Gillessen et al. (2009b) have values of 8.4 $\pm$ 0.4 kpc, 7.7 $\pm$ 0.4 kpc, and 7.3 $\pm$ 0.5 kpc, respectively[10].

We present a new set of infrared astrometric standards that can be used to define the reference frame (with Sgr A*-radio at rest, at the origin) in smaller field of view Galactic center measurements that do not contain enough of the SiO radio masers and that are used for stellar orbit measurements. We measure the motion of the stellar cluster in a Sgr A*-rest frame and confirm that the cluster rotates in the plane of the Galaxy.

A stable astrometric reference frame is a key requirement when using stellar

[10]The orbital analysis compared is the case of S0-2 only, no 2002 astrometric data, and priors only on V_z

orbits to study the central supermassive black hole and its environment. Stellar orbits have already proven to be powerful tools for measuring the black hole's mass and distance, as well as placing limits on a black hole companion (Ghez et al., 2008; Gillessen et al., 2009b). In time, stellar orbital work will probe the extended mass distribution and general relativity through the detection of prograde and retrograde precession, respectively (Rubilar & Eckart, 2001). Weinberg et al. (2005) considered the effect of an assumed extended mass distribution within the orbit of the central arcsecond, 16-year period star, S0-2, and estimated an apocenter shift after one revolution of $\Delta s \sim$0.3 mas, which corresponds to an effect of $\phi \sim$0.02 mas yr^{-1} (or an angular velocity of 0.08 mas yr^{-1} arcsec^{-1})[11]. The prograde relativistic precession of S0-2, on the other hand, is predicted to be $\phi \sim$0.06 mas yr^{-1} (or an angular velocity of 0.27 mas yr^{-1} arcsec^{-1}; Weinberg et al., 2005), thereby requiring a reference frame that is stable to 0.02 mas yr^{-1}. Detection of either the prograde or retrograde precession of the central arcsecond sources will therefore require an extremely stable astrometric reference frame.

Figure 2.21 shows the expected improvement in the stability of the astrometric reference frame with time using the maser method described in §2.3. The various contributions to the stability of the reference frame come from measurements of the SiO masers in both the radio (*dotted lines*) and infrared (*dash-dotted lines*), as well as from the transformation of the infrared stars into the Sgr A*-radio rest frame (*thick solid lines*). In order to detect either the prograde relativistic precession or the retrograde precession from the extended mass distribution, the combination of these various sources of error must be reduced to less than 0.02 mas yr^{-1}. Figure 2.21 shows that this will be possible only starting in the year $\sim$2022, using the method described in §2.3. High precision radio measurements

[11]We note that this is only an approximation as the amount of extended mass within the orbit of S0-2 is highly unknown.

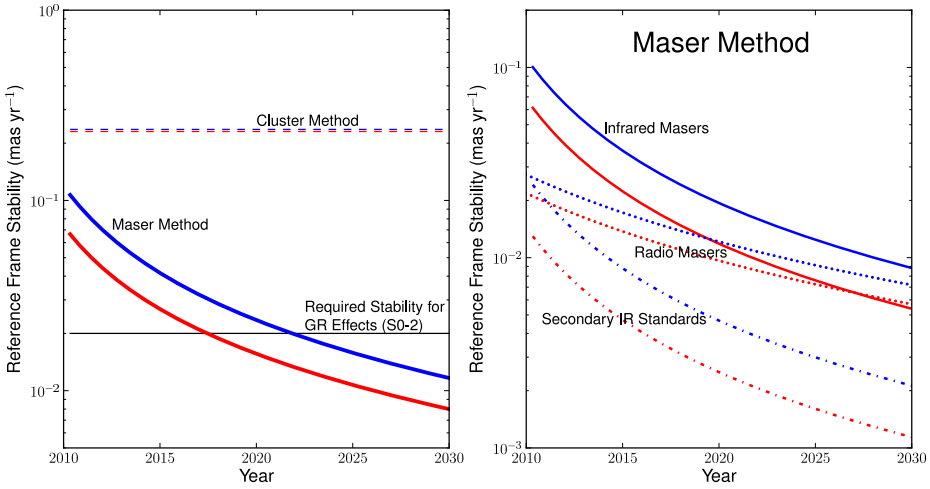

Figure 2.21 (*Left*) Predicted stability in X (*red*) and Y (*blue*) of the reference frame with time (assuming the field of view of Keck AO images, $10'' \times 10''$). The maser method (*solid curves*; §2.3) allows for an improvement in the stability with time as $t^{-3/2}$, whereas the cluster method (*dashed lines*), which assumes no net motion of the stellar cluster, is fundamentally limited by the cluster's intrinsic dispersion and therefore will not improve with time. In order to detect the prograde relativistic precession at the 3σ level (neglecting the retrograde precession due to the extended mass distribution), the reference frame must be stable to within $\sim$0.02 mas yr^{-1} (*black line*). Using the maser method, a significant detection of the retrograde precession of S0-2's orbit will be possible beginning in the year $\sim$2022. (*Right*) The three sources of error that contribute to the stability of the reference frame using the maser method are shown separately. These include the radio masers (*dotted*), the infrared masers (*thick solid*), and the secondary astrometric standards (*dash-dotted*). Note the different scaling for the Y axis in the two plots.

of additional masers within this region, such as IRS 14NE (Li et al., 2010) or others that may be discovered with the Expanded Very Large Array (EVLA), would help to achieve the required level of precision more rapidly, as the IR measurements are already in hand for this entire region.

2.5 Appendix A: Starfinder

Starfinder iteratively determines first the PSF, from a set of user selected "PSF stars", and then the positions and fluxes of all stars in the field (Diolaiti et al., 2000). Successive iterations improve the PSF estimate by subtracting off stars identified in the previous pass. However, errors in the initial PSF estimate can lead to spurious source detections due to speckles or airy ring substructure that are incorrectly identified as stars. These errors propagate through all iterations and lead to increased astrometric noise from fitting an incorrect PSF and astrometric biases due to the detection of false sources.

To minimize the impact of these false sources on the PSF estimation and subsequent astrometry and photometry, we insert a step into each *StarFinder* iteration that trims out these false sources from the list of identified stars before re-extracting the PSF on subsequent iterations. We define our valid star detection limits as a contrast curve of delta-magnitude vs. separation, which is computed by azimuthally averaging the PSF. For every source, we remove all detections that are fainter than this contrast curve. This typically removes 20% of the originally detected sources, with roughly half coming from from substructure in the first airy wing and the other half coming from speckles in the extended PSF halo. We also increased our PSF box size from 1", as used in Ghez et al. (2008) and Lu et al. (2009), to 2" to improve photometric accuracy; however, this had a minimal impact on astrometry.

2.6 Appendix B: Distortion Uncertainties for the IR Maser Mosaic

We generate a map of positional uncertainties that arise from uncertainties in the distortion model for our IR maser mosaic to facilitate assignment of this source of uncertainty. This is simply a mosaic of the distortion uncertainty models discussed in §2.2.1 and shown in Figure 2.7, where the residual distortion of 0.1 pix (§2.2.2) was added in quadrature to each pixel. To construct the mosaicked error map, we compute the distortion error contribution at each pixel as

$$\sigma_{dist} = \sqrt{\frac{\sigma_1^2 + \sigma_2^2 + ... + \sigma_N^2}{N}} \tag{2.4}$$

where σ_i is the distortion uncertainty at each individual pixel and N is the number of overlapping fields, which can vary between 1 and 4. This resulted in a mosaicked map of approximately 2200×2200 pix.

2.7 Appendix C: Possible Astrometric Bias from IRS 7

The linear motion modeling of the IR maser measurements in §2.3.1 have unexpectedly low reduced χ^2. In our current analysis, alignment uncertainties are treated as purely random errors. If there is a systematic problem with one of the radio maser positions, this could create a significant correlated alignment error that is not captured in our present analysis and cause the reduced χ^2 to be smaller than its expected value for random errors. Indeed, one possible culprit is the radio position of IRS 7, which, as discussed in Reid et al. (2003) is more uncertain than the other masers used for two related reasons. First, it is a supergiant and therefore is expected to have a much larger maser emission region (r ∼

10 mas) than the other masers used, which are thought to be Mira variables (r $\sim$ 1 mas). Second, the maser spot location for IRS 7 jumped in 1998 (although the spots moved with similar proper motion before and after 1998), making the position of IRS 7 harder to assess than its proper motion. The solution has been to take the mid-point between the positions before and after 1998, which amounts to applying a 10 mas offset to the post-1998 values and increasing the positional uncertainties to 5 mas. If we remove this offset from the reported position of IRS 7 in our analysis (prior to aligning the IR positions in each epoch), the resulting average χ^2 of the linear motion models for the IR maser measurements is 0.97, which may suggest that this offset should not be applied. Since this has only a minor impact on our current analysis, we have used the values reported in §2.3.1 and Table 2.5 for the results reported in this study. However this may become a more important issue in the future as the precision of the IR maser measurements improves as discussed in §2.4.

CHAPTER 3

The Eccentricity Distribution and Radial Structure of the Young Stellar Disk in the Galactic Center

The presence of the young, massive stars in the vicinity of the supermassive black hole (SMBH) at the center of the Galaxy has puzzled both observers and theorists alike since their discovery over two decades ago (for a review, see Genzel et al., 2010). Spectroscopic observations of the central parsec have revealed an enigmatic population of nearly 200 hot, early-type stars, including Wolf-Rayet (WR) stars and O and B type main sequence stars, giants, and supergiants (Allen et al., 1990; Krabbe et al., 1991, 1995; Blum et al., 1995; Tamblyn et al., 1996; Najarro et al., 1997; Ghez et al., 2003; Paumard et al., 2006; Do et al., 2009a; Bartko et al., 2010). Their location in the GC raises the question of how stars can form in such a hostile environment, as the tidal forces from the 4×10^6 $M_\odot$ SMBH (Ghez et al., 2008; Gillessen et al., 2009b) would prevent the collapse of typical molecular clouds within its radius of influence (Sanders, 1992; Morris, 1993).

Clues to the origin of these stars can be gained through the detailed study of their orbital dynamics, as the age of the population ($\sim$6 Myr; Paumard et al., 2006) is much less than the relaxation timescale in the Galactic center ($\sim$1 Gyr; Hopman & Alexander, 2006). A particularly prominent feature that has been observed is a stellar disk containing a large fraction of the O and WR stars orbit-

ing the black hole in a clockwise (CW) sense, with an inner edge at a projected radius of $R = 0''.8$ (Genzel et al., 2000; Levin & Beloborodov, 2003; Genzel et al., 2003; Paumard et al., 2006; Lu et al., 2009; Bartko et al., 2009). At smaller radii, dynamical effects such as vector resonant relaxation (Rauch & Tremaine, 1996; Hopman & Alexander, 2006; Alexander, 2007) will randomize the orbital planes within the lifetimes of the B stars, which is in agreement with observations (Schödel et al., 2003; Ghez et al., 2005b; Eisenhauer et al., 2005; Gillessen et al., 2009b). The coherent motion of the disk stars may be indicative of *in situ* formation in a massive, gas disk around the SMBH (Levin & Beloborodov, 2003). Standard models of accretion disks around central black holes are expected to fragment under their own self-gravity and lead to the formation of stars (Kolykhalov & Syunyaev, 1980; Shlosman & Begelman, 1987; Goodman, 2003; Nayakshin, 2006). In such models, the steady build-up of the gas disk leads to stars on circular orbits, as the gas will have circularized prior to star formation. However, there is growing evidence that the young stars are on more eccentric orbits (Paumard et al., 2006; Beloborodov et al., 2006; Lu et al., 2009; Bartko et al., 2009; Gillessen et al., 2009b). Several theories have invoked the infall of giant molecular clouds or the collision of two clouds to produce initially eccentric stellar disks (Mapelli et al., 2008; Yusef-Zadeh & Wardle, 2008; Wardle & Yusef-Zadeh, 2008; Bonnell & Rice, 2008). The surface density predicted by *in situ* formation scenarios falls off like r^{-2} (Lin & Pringle, 1987; Levin, 2007) and agrees well with observations of the disk (Paumard et al., 2006; Lu et al., 2009; Bartko et al., 2009).

A stellar disk may also result from the inward migration of a massive cluster whose stars are tidally stripped as it spirals in under dynamical friction (Gerhard, 2001). However, this theory has been difficult to reconcile with observations, most notably the surface density profile. During the infall, the cluster will deposit

stars throughout the GC with a radial profile of $r^{-0.75}$, much shallower than that observed (Berukoff & Hansen, 2006). Furthermore, in order for the cluster to reach the small galactocentric radii that the young stars occupy, unrealistic cluster properties are required, such as an initial cluster mass of $>10^5$ $M_\odot$ or the presence of an intermediate mass black hole (IMBH; Hansen & Milosavljević, 2003; Gürkan & Rasio, 2005; Berukoff & Hansen, 2006) containing too large a fraction of the total cluster mass (Kim et al., 2004).

While there is consensus in the literature regarding the existence of the clockwise disk and its surface density profile, many of its properties have yet to be constrained, in part because interpretations of kinematic studies rely on the ability to assign disk membership. For example, Bartko et al. (2009) reported a bimodal eccentricity distribution for the disk, which is difficult to explain dynamically. The authors could not rule out that contamination by non-members of the disk led to the second peak seen at $e = 0.9$ - 1.0. Contamination may also affect the interpretation of the geometric structure of the disk, which was recently claimed to be highly warped (Bartko et al., 2009).

Further controversy exists regarding the kinematic properties of the stars that are not on the clockwise disk. Claims of a second, counterclockwise (CCW) disk have been made (Genzel et al., 2003; Paumard et al., 2006), although this structure has been refuted by Lu et al. (2009) and later reinterpreted as a possible streamer or dissolving disk by Bartko et al. (2009). Precise orbital parameter estimates are necessary for resolving this issue, as the presence of a second structure has implications for both star formation and stellar dynamical evolution in the Galactic center. For example, Löckmann & Baumgardt (2009) showed that if two highly inclined disks of different masses did exist at one point in the GC, their mutual interaction would lead to the ultimate destruction of the lower mass

disk within 5 Myr and we would therefore not observe the structure today. Such a scenario, however, would demand that two star formation events at or near the GC occurred within 2 Myr of one another. Others have proposed a disk-origin for all of the massive, young stars, many of which have dynamically evolved off of the original disk's orbital plane. Dynamical torques on the disk from an intermediate mass black hole (Yu et al., 2007) or from the circumnuclear disk (CND; Šubr et al., 2009; Haas et al., 2011a,b) located at $R \sim 1.5$ pc (Christopher et al., 2005), for example, can excite stars to relatively high inclinations.

We have carried out a detailed kinematic analysis of the Galactic center's young star population using high precision astrometric measurements over a 16-year baseline. Both the size and radial extent of our sample have increased by a factor of ∼3-4 over our previous efforts in Lu et al. (2009). The sample is presented in §3.1 followed by the data sets used in §3.2. The data analysis, including image processing and the astrometric techniques used, are detailed in §3.3. In §3.4 and §3.5 we present the orbital analysis and results. A series of simulations of a clockwise disk around the SMBH are presented, and compared to the observational data in an attempt to describe the disk properties and are presented in §3.6. The implications of our results are described in §3.7 and we conclude in §3.8.

3.1 Sample

There are 116 stars that form the sample of this study (see Figure 3.1). These stars are selected based on the following four criteria:

1. located outside $R = 0\farcs8$, which has been previously identified as the inner edge of the clockwise disk;

2. located within the $27'' \times 27''$ region centered roughly on Sgr A* and defined by our widest imaging field of view (see §3.2);

3. are spectroscopically identified as young; and

4. have spectral line depths sufficient to measure a radial velocity (RV) and are reported in this work, Do et al. (2009a), Bartko et al. (2009) or Paumard et al. (2006). We note that Bartko et al. (2010) report the discovery of an additional 62 O, B, and WR stars, but do not publish the locations or velocities of these stars. We therefore cannot include these stars in our analysis here.

For these stars, we report new or updated astrometric measurements and radial velocities. The radial velocities for 38 young stars and astrometry for 84 young stars are reported here for the first time from our Keck observations, which are described in the next section.

3.2 Data Sets

3.2.1 Narrow Field Imaging Observations

The primary astrometric measurements in this study were made over a 16-year baseline using a combination of high angular resolution speckle K-band ($2.2\mu m$) and adaptive optics K'-band (2.12μm) imaging. The speckle data, obtained between 1995 and 2005 from the W. M. Keck I telescope using the Near Infrared Camera (NIRC; Matthews & Soifer, 1994; Matthews et al., 1996), have a $\sim 5'' \times 5''$ field of view and have been reported in previous publications (Ghez et al., 1998, 2000, 2005b, 2008; Lu et al., 2009). From the 27 epochs of available speckle data, we use those epochs with more than 900 frames to insure robust coordinate trans-

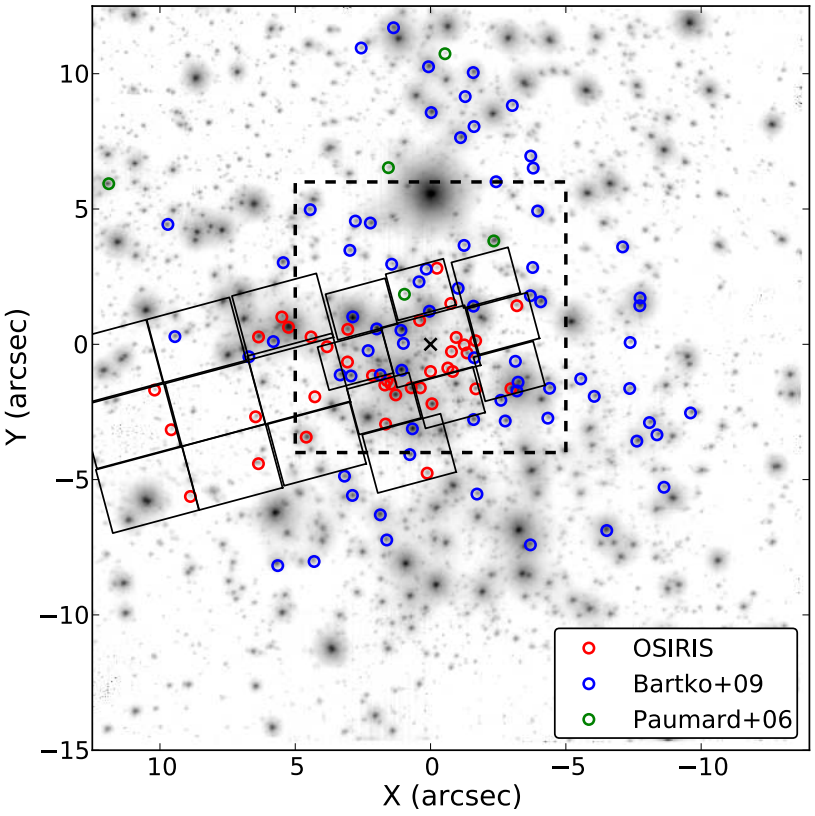

Figure 3.1 The location of the 116 young stars with RV and astrometric measurements that comprise the sample for this study. In the background is the wide-field adaptive optics mosaic image from 2008 May covering the central ∼1 pc of the Galaxy. Each star is color-coded based on the source of its radial velocity measurement. We also show the field coverage of our OSIRIS observations (*solid boxes*) and the central 10″ field of view (*dashed box*). This is the largest sample used to study the kinematic structure of the young star population to date.

formations (see §3.3.2.2). This excludes only 2000 April (805 frames), resulting in 26 speckle epochs with a time baseline of 10 years (see Table 3.1).

Since 2004, we have utilized the Keck II adaptive optics (AO) system in conjunction with the facility near infrared camera NIRC2 (PI: K. Matthews) in its narrow-field mode, which has a plate scale of 9.952 mas/pix as reported in Yelda et al. (2010) and a 10″ field of view (∼0.4 pc at the 8 kpc distance to the GC; Ghez et al., 2008). Here we include all existing Keck AO observations, which span 19 epochs and a time baseline of seven years. The first eight of these observations (from 2004 to 2007) were reported in earlier studies (Ghez et al., 2005a, 2008; Lu et al., 2009), and, to these data, we add 11 new AO data sets taken between 2008 and 2011, which doubles the AO time baseline. The observational setup for these new data was the same as the 2006-2007 laser guide star adaptive optics (LGSAO) observations reported in Ghez et al. (2008). Specifically, a 20-point pseudo-random 0.7″×0.7″ dither pattern was used, with an initial position that placed IRS16NE at pixel (229, 720). The images were taken at a position angle (PA) of 0°, and each frame consisted of 10 co-added 2.8 s integrations. At least three exposures were taken at each dither position. The star USNO 0600-28577051 (R=13.7 mag and Δr_{SgrA^*}=19″) was used to correct for tip and tilt in the LGSAO observations and served as the natural guide star in the NGSAO observation of the Galactic center. All AO data sets used in this work are summarized in Table 3.1.

Table 3.1. Summary of Speckle and AO Imaging Observations

Date (UT)	Frames Obtained	Frames Used	FWHM (mas)	Strehl	N_{stars}	K_{lim}[a] (mag)	σ_{pos}[b] mas	Data Source[c]
1995.439	15114	1800	57	0.06	151	15.4	1.06	speckle; (ref. 1)
1996.485	9261	865	60	0.03	77	14.1	1.76	speckle; (ref. 1)
1997.367	3811	1837	61	0.04	139	15.4	1.28	speckle; (ref. 1)
1998.251	9751	1639	62	0.04	83	14.6	1.52	speckle; (ref. 2)
1998.366	16531	2102	69	0.04	126	15.4	1.32	speckle; (ref. 2)
1998.505	9751	933	61	0.06	127	15.3	1.24	speckle; (ref. 2)
1998.59	20375	1933	61	0.06	172	15.6	0.84	speckle; (ref. 2)
1998.771	4776	1082	55	0.07	120	15.3	1.49	speckle; (ref. 2)
1999.333	19512	1857	70	0.07	183	15.7	1.06	speckle; (ref. 2)
1999.559	19307	2108	55	0.09	232	15.8	0.75	speckle; (ref. 2)
2000.381	21492	2492	55	0.08	242	15.8	0.67	speckle; (ref. 3)
2000.548	15124	1581	61	0.07	194	15.6	1.11	speckle; (ref. 3)
2000.797	2587	1517	59	0.04	77	14.4	1.34	speckle; (ref. 3)
2001.351	11343	1994	54	0.07	175	15.5	1.03	speckle; (ref. 3)
2001.572	15920	1695	54	0.11	239	16.0	0.79	speckle; (ref. 3)
2002.309	16130	1958	66	0.05	183	15.7	1.15	speckle; (ref. 3)
2002.391	18338	1443	58	0.08	252	15.8	0.85	speckle; (ref. 3)
2002.547	8878	1118	61	0.06	125	15.3	1.40	speckle; (ref. 3)
2003.303	14475	1841	61	0.04	121	15.3	1.06	speckle; (ref. 3)
2003.554	6948	1703	64	0.07	180	15.7	1.17	speckle; (ref. 3)
2003.682	9799	1723	63	0.07	182	15.7	1.22	speckle; (ref. 3)
2004.327	20140	1423	62	0.08	185	15.7	0.75	speckle; (ref. 4)
2004.564	14440	2161	59	0.08	200	15.7	0.86	speckle; (ref. 4)
2004.567	10	10	60	0.28	598	15.9	0.30	LGSAO; (ref. 5)
2004.66	3040	1301	57	0.08	167	15.6	1.25	speckle; (ref. 4)
2005.312	15770	1679	59	0.06	162	15.6	0.99	speckle; (ref. 6)
2005.495	10	10	61	0.26	929	16.3	0.32	LGSAO; (ref. 8)
2005.566	14820	1331	60	0.05	111	15.2	1.19	speckle; (ref. 6)
2005.58	59	31	57	0.18	1865	19.0	0.10	LGSAO; (ref. 7)
2006.336	153	107	58	0.24	1952	19.1	0.05	LGSAO; (ref. 7)
2006.47	289	156	57	0.30	2460	19.5	0.08	LGSAO; (ref. 7)
2006.541	70	64	58	0.28	2179	19.3	0.09	LGSAO; (ref. 7)

Table 3.1—Continued

Date (UT)	Frames Obtained	Frames Used	FWHM (mas)	Strehl	N_{stars}	K_{lim}[a] (mag)	σ_{pos}[b] mas	Data Source[c]
2007.374	101	76	58	0.28	2514	19.4	0.09	LGSAO; (ref. 7)
2007.612	139	78	57	0.24	1879	19.0	0.08	LGSAO; (ref. 7)
2008.371	138	134	54	0.25	2089	19.4	0.06	LGSAO; (new)
2008.562	179	104	58	0.27	2189	19.3	0.04	LGSAO; (new)
2009.34	311	149	57	0.27	2316	19.2	0.08	LGSAO; (new)
2009.561	146	75	62	0.21	1701	18.9	0.09	LGSAO; (new)
2009.689	55	43	61	0.25	1921	18.9	0.11	LGSAO; (new)
2010.342	219	158	63	0.23	2037	19.1	0.06	LGSAO; (new)
2010.511	136	117	61	0.23	1956	18.9	0.08	LGSAO; (new)
2010.62	143	127	60	0.21	1826	19.0	0.07	LGSAO; (new)
2011.401	164	114	66	0.19	1563	18.8	0.13	LGSAO; (new)
2011.543	212	167	59	0.21	2031	19.2	0.08	NGSAO; (new)
2011.642	218	196	59	0.27	2372	19.4	0.05	LGSAO; (new)

[a]K_{lim} is the magnitude at which the cumulative distribution function of the observed K magnitudes reaches 90% of the total sample size.

[b]Positional error taken as error on the mean from the three sub-images in each epoch and includes stars with $K < 15$.

[c]Data originally reported in (1) Ghez et al. (1998), (2) Ghez et al. (2000), (3) Ghez et al. (2005b), (4) Lu et al. (2005), (5) Ghez et al. (2005a), (6) Rafelski et al. (2007), (7) Ghez et al. (2008), and (8) Lu et al. (2009).

Table 3.2. Summary of Wide-field Mosaic Observations

Date (UT)	N Dither Positions	$< N_{frmObtained} >$ per Position	$< N_{frmUsed} >$ per Position	FWHM (mas)	Strehl	N_{stars}	K_{lim}[a] (mag)	σ_{pos}[b] mas
2006 May	13	3.4	3.4	63	0.20	6583	18.1	1.63
2008 May	13	3.4	2.9	78	0.11	4494	17.1	1.88
2010 June	9	7.2	5.4	76	0.12	5189	17.6	1.71

[a]K_{lim} is the magnitude at which the cumulative distribution function of the observed K magnitudes reaches 90% of the total sample size.

[b]Positional errors include distortion error (see text).

3.2.2 Wide Field Imaging Mosaic Observations

To measure the proper motions of the young stars at larger radii from Sgr A* ($R \gtrsim 7''$), we obtained three epochs of K'-band LGSAO mosaics with the NIRC2 narrow camera that cover $27''\times27''$ ($\sim$1.1 pc $\times$ 1.1 pc). These observations were taken in 2006 May 3, 2008 May 20, and 2010 June 5. The tip-tilt star, PA, filter, exposure time, and initial position were the same as those used for the central $10''$ data set. In order to obtain the large field of view, we used a 9-position box pattern with a $8.5''$ dither offset and 3-7 frames at each dither position. For the first two epochs, we also obtained a 4-position box pattern with $4''$ dithers, providing large overlaps between all tiles in the mosaic. At least three exposures were taken at each dither position. We refer to these wide-field data as "mosaics" and the details of the observations can be found in Table 3.2.

3.2.3 Spectroscopic Observations

To spectroscopically identify young stars and measure their line-of-sight motions, high angular resolution spectroscopic observations were obtained with the integral field spectrograph OSIRIS in conjunction with the LGSAO sytem at Keck II (Larkin et al., 2006). The central $4''$ have been observed since 2006 with the Kn3 narrowband filter centered on the Brγ line ($\lambda = 2.1661$ μm) and using the 35 mas plate scale. In 2010, we began the Galactic Center OSIRIS Wide-field Survey (GCOWS), in which observations were taken along the eastern portion of the clockwise disk in order to maximize the number of young star identifications (Do et al., in prep.). These observations reached a radial extent of $R \sim 14''$ east of Sgr A* and used the 50 mas plate scale. The details of our OSIRIS observations are presented in Ghez et al. (2008), Do et al. (2009a), and Do et al. (in prep.). While the spectroscopic identification of young stars using OSIRIS has been reported elsewhere (Do et al., 2009a, Do et al. in prep.), we report the radial velocities from this instrument for the first time here.

3.3 Data Analysis

3.3.1 Image Processing

All data sets were reduced using standard data processing techniques, including sky subtraction, flat-fielding, and bad-pixel and cosmic-ray rejection. The AO data were corrected for both optical distortion using the latest solution for the NIRC2 narrow camera and achromatic differential atmospheric refraction (DAR; Yelda et al., 2010). Based on this distortion solution, we derive an improved solution for the NIRC speckle camera (Appendix 3.9) using a similar approach to Lu et al. (2009). The updated NIRC distortion coefficients are presented in

Table 3.5.

For each observing run, individual frames are combined to make an average map. The details of this process depend on the observing technique used. The speckle data are combined to create an average image for each epoch using a weighted shift and add technique as described in Hornstein (2007). The final speckle images cover a field of view of $\sim 6'' \times 6''$, centered approximately on Sgr A*. For the adaptive optics narrow field data, frames are selected based on the image quality, as measured by the full width at half-maximum (FWHM) of the point spread function. We choose to keep only those frames whose FWHM is within 25% of the minimum observed FWHM measured in a given epoch. These images are then combined with a weighted average, where the weights are equal to the Strehl ratio of each image. For each epoch of mosaic data, we create an average image at each dither position (i.e., 13 for each of the 2006 and 2008 observations, and nine for the 2010 observation). All exposures taken at a given dither position are included in the corresponding average image except for a few cases where the frames were of extremely poor quality for one of several reasons (e.g., clouds or laser collision with neighboring telescopes). As done in our previous efforts, we create three independent subset images of equivalent quality in order to determine astrometric and photometric uncertainties for the speckle and AO central $10''$ images. Likewise, subset images are created for each of the individual dither positions in the mosaics.

3.3.2 Astrometry

3.3.2.1 Star Lists

Stars are identified and their positions are extracted from all images using the PSF fitting algorithm *StarFinder* (Diolaiti et al., 2000), which is optimized for

AO observations of crowded stellar fields to identify and characterize stars in the field of view. A model PSF for each image is iteratively constructed based on a set of bright stars in the field that have been pre-selected by the user. The model PSF is then cross-correlated with the image in order to identify sources in the field. The stars that are input for PSF construction are IRS 16C, 16NW, and 16NE for the speckle images, and IRS 16C, 16NW, 16SW, 16NE, 29, 33E, S1-23, S2-16, and S3-22 for the central 10″ AO images. The set of PSF stars used for each image in the mosaic, on the other hand, depends on the position of that image within the wide mosaic field of view. These stars include the aforementioned sources for the central 10″ AO data set, as well as the following stars: IRS 1NE, 1SE, 2, 7, 9, 10EE, 10E3, 12N, 14SW, 14NE, 28, 34W, S5-183, S5-69, S8-3, S8-8, S9-3, S9-9, S10-2, S10-3, S11-4, S11-6, S9-5, S12-2, S13-61. To identify sources, we use a *StarFinder* correlation threshold of 0.8 in the average image and 0.6 in each of the three subset images. The initial star list for each epoch contains only those sources that are detected in the average image and in all three subset images. The inaccuracies in the PSF model for the adaptive optics images occasionally lead to spurious source detections near bright stars. We therefore use the procedure described in Appendix A of Yelda et al. (2010) to remove these false sources (∼20% of the sources identified). Altogether, we identify 162 and 1915 stars on average in the speckle ($<K_{lim}> = 15.4$) and AO data sets ($<K_{lim}> = 18.8$), respectively.

There are two sources of statistical uncertainty associated with each positional measurement in the narrow field images. First is the centroiding uncertainty (σ_{cnt}), which is taken as the error on the mean of the positions for each star in the three subset images. Second, there is a term that appears to arise from inaccuracies in the estimates of the PSF wings of neighboring sources. As described in Appendix 3.10, we follow a procedure similar to Clarkson et al.

(2012), and estimate this additive error term (σ_{add}) to be 0.18 mas and 0.10 mas for the speckle and central 10″ observations, respectively. Figure 3.2 shows the centroiding and additive errors for each of our speckle and central 10″ data sets. In addition, three of the adaptive optics data sets were taken at either different positions or position angles than the rest of the AO observations and therefore are impacted by residual distortion left over after the distortion correction is applied, as described in Yelda et al. (2010). We account for the effects of residual distortion in these images by performing a local distortion correction (Appendix 3.11), which adds 0.5-1.4 mas errors to these epochs. The centroiding uncertainties in the speckle data are typically a factor of ∼5 larger than the additive error and therefore dominate the error budget. For the AO data, these two error terms are comparable (σ_{cnt} ∼0.1 mas).

Final star lists for the wide field mosaics require additional steps and a different treatment of the uncertainties. Star lists are created for each tile in the mosaics similarly to the central 10″ AO data. The full mosaic star list is then constructed by sequentially stitching together the lists from each tile following a procedure similar to that in Anderson & van der Marel (2010). We begin by first transforming the stars' positions from the central tile to their positions in the Sgr A*-radio rest frame, in which ∼1200 stars down to a K-band limiting magnitude of $K_{lim} \sim 16$ were measured over the central $22'' \times 22''$ in Yelda et al. (2010) and are updated here (see next section). We note that our wide field mosaics include fainter ($K_{lim} \sim 18$) and more distant (FOV $\sim 30'' \times 30''$) stars than what was measured in Yelda et al. (2010). Once the central tile is transformed, a new reference list of positions is created in the following way. For stars that are matched across the two lists being transformed, their positions and their associated errors are updated. The new positions are taken as the weighted average of the positions in the two previously aligned lists and weighted by their

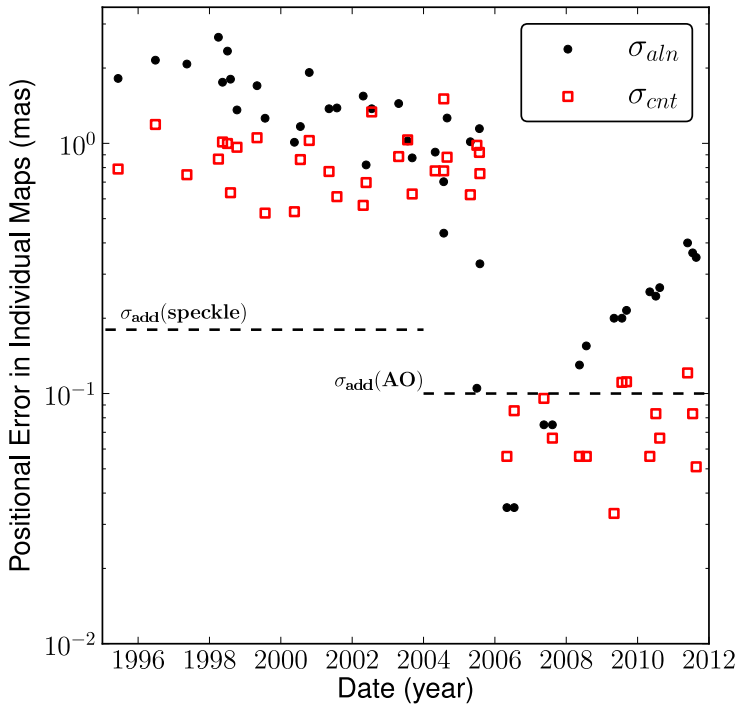

Figure 3.2 Alignment (*filled black points*) and centroiding (*unfilled red squares*) uncertainties as a function of epoch, which include speckle data from 1995-2005 and central 10″ AO data from 2004-2011. The median uncertainty of the young stars is reported for each epoch. Alignment errors are minimized near the reference epoch, 2006 June, and increase with time away from this epoch. All epochs with $\sigma_{aln} > 0.5$ mas are from speckle imaging, where the higher uncertainties are a result of very few reference stars as compared to AO data. The additive errors for speckle and AO are shown as dashed lines.

centroiding and distortion errors[1]. The new positional errors are taken as the average of the errors from the two previously aligned lists. For the stars that do not have positions in the Sgr A*-radio frame (i.e., those fainter than $K \sim 16$ or outside the $22'' \times 22''$ FOV), we include their transformed positions and their original errors (centroiding and distortion errors) in the new reference list.

[1]Distortion errors include the statistical error (∼0.05 pix) in the optical distortion model and the residual distortion term (∼0.1 pix), both of which are described in Yelda et al. (2010).

This new list then serves as the reference list for the stitching of the next tile in the sequence. This procedure is repeated until all tiles are aligned. The order in which each tile is aligned is as follows. After the central field from the 9-point dither observations is first aligned, the tiles from the 4-point dither (if they were taken) are aligned (in the order: SW, NE, SE, NW). This is followed by the alignment of the remaining tiles from the 9-point dither observations (in the order: E, W, N, S, NE, SE, NW, SW). After completing the full alignment, we refine this intermediate star list by once again transforming each tile's star list to it a final time. Each of the alignments performed in these steps involves a 2nd order polynomial transformation, consisting of 12 coefficients.

3.3.2.2 Cross-Epoch Coordinate Transformations

In order to measure relative positions and proper motions, stellar positions from each epoch must be transformed to a common reference coordinate system. This procedure is complicated by the fact that stars available for performing the transformation have detectable proper motions. Previous Galactic center astrometric reference frames were constructed by minimizing the net displacement of reference stars between star lists, a procedure which implicitly assumes that these stars have no net motion over the field (the "cluster" reference frame; e.g., Eckart & Genzel, 1997; Ghez et al., 1998, 2008; Gillessen et al., 2009b)[2]. However, net motion is known to exist in the GC, including an overall rotation of the late-type star cluster in the plane of the Galaxy (Trippe et al., 2008; Schödel et al., 2009; Yelda et al., 2010), as well as coherent motion in a clockwise, young stellar disk in the central parsec (Levin & Beloborodov, 2003; Genzel et al., 2003; Paumard et al., 2006; Lu et al., 2009; Bartko et al., 2009). Neglecting to account for this

[2]We note that Gillessen et al. (2009b) define a reference frame using a combination of the cluster and maser reference frames.

motion results in degeneracies between the transformation parameters and the measured stellar velocities. It is therefore important to understand the motion of these stars if they are to be used in the construction of a stable reference frame.

The positions and proper motions presented in Yelda et al. (2010) of >1200 Galactic center stars offer an opportunity to construct a stable astrometric reference frame for this work. Astrometric measurements of these secondary standards were determined relative to Sgr A* in a reference frame constructed by tying infrared astrometry of seven SiO masers to their precise radio measurements (the "maser" reference frame; Reid et al., 2007; Yelda et al., 2010). Here we update these positions and velocities using a slightly modified version of the analysis described in Yelda et al. (2010). Specifically, we now use mosaicked star lists (described in §3.3.2.1) as opposed to mosaicked images. The mosaicked star lists are comprised of the nine individual lists from the nine fields that cover the radial extent of the masers. The Sgr A*-rest reference frame was otherwise created in the same way as in Yelda et al. (2010). The updated positions and proper motions relative to Sgr A* for 1210 stars are presented in Table 3.3. As compared to the previous measurements reported in Yelda et al. (2010), we find several stars with $>3\sigma$ difference in either the X ($N = 6$ stars) or Y ($N = 19$ stars) velocity coordinate. However, the χ^2 value of the velocity fits improved in almost all cases with our new analysis, and we therefore use these updated values when constructing our reference frame. One final note is that we present fewer astrometric standards here as compared with Yelda et al. (2010), which had 1279 stars. All 69 missing stars are fainter than $K = 15.5$. The reason for this is that with mosaicked images as opposed to mosaicked starlists, higher signal to noise is achieved in the overlapping areas and therefore fainter stars can be detected.

Table 3.3. Galactic Center Secondary IR Astrometric Standards

Name	K' (mag)	$T_{0,IR}$ (year)	Radius (arcsec)	Δ R.A. (arcsec)	$\sigma_{R.A.}$[a] (mas)	Δ Dec. (arcsec)	σ_{Dec}[a] (mas)	v_{RA}[b] (mas yr^{-1})	v_{Dec}[b] (mas yr^{-1})
S0-3	14.8	2008.39	0.36	0.3351	1.1	0.1195	1.4	9.4 ± 0.4	-1.2 ± 0.6
S0-6	14.2	2008.30	0.36	0.0292	1.1	-0.3624	1.2	-5.2 ± 0.3	3.7 ± 0.4
S0-5	15.3	2007.99	0.41	0.1790	1.1	-0.3664	1.3	-2.1 ± 0.3	0.4 ± 0.5

Note. — This is an updated version of Table 2.7 (see text). The table will be published in its entirety in the electronic version of Yelda et al. (in prep).

[a]Positional errors include centroiding, alignment, and residual distortion (1 mas) errors, but do not include error in position of Sgr A*.

[b]Velocity errors do not include error in velocity of Sgr A* (0.09 mas yr^{-1}, 0.14 mas yr^{-1} in RA and Dec, respectively).

The alignment of the stars' positions across all epochs is a multi-step process. The star lists from the deep central AO and speckle images are transformed to the coordinate system defined by the 2006 June AO image using a second-order polynomial transformation. This epoch was chosen as the reference epoch, t_{ref}, because it is the deepest of our data sets (K_{lim}=18.5 versus K_{lim}=15.5 for our earlier fiducial epoch of 2004 July). In the alignment of each epoch, t_e, we first propagate the positions of the secondary astrometric standards from t_{ref} to the expected positions in t_e using their known velocities. We then find the best-fit transformation from the original positions in t_e to their propagated positions. This use of velocity information allows us to use all of the astrometric standards, regardless of spectral type, and removes the degeneracy between frame transformations and the stellar velocities. Uncertainties from this transformation (σ_{aln}) are characterized using a half-sample bootstrap. These alignment errors are a function of time from the reference epoch and of the number of reference stars used in the transformation. As seen in Figure 3.2, σ_{aln} is minimized near the reference epoch and is larger for the speckle epochs ($\sigma_{aln} > 0.5$ mas), which have on average $\sim$6$\times$ fewer reference stars than are available in AO epochs.

The speckle observations were taken in stationary mode, and so the field rotated over the course of the night. As a result, the final image had a field of view with varying numbers of frames contributing to each pixel. This led to relatively poor astrometric measurements near the edges of the FOV. To account for this effect, we require that each source be at a location in the average map that was covered by at least 80% of the frames contributing to that map. This prevented edge effect problems for these data sets, which had much less uniform coverage than the AO data sets. In total, 300 combined detections from 15 stars near the edge of the speckle field of view were removed.

Given the high stellar density environment of the Galactic center, it is important to consider the effects of source confusion (Ghez et al., 2008; Gillessen et al., 2009b; Fritz et al., 2010). Stellar positions can be affected by unknown, underlying sources that have not previously been detected, or they may be affected by known sources that, when passing sufficiently close to a star, get detected as only one source instead of two. While it is not possible to account for the former case, we can determine when a star's positional measurement is biased by another known source. Using preliminary acceleration fits (see §3.3.2.3), the distance between every pair of stars in the narrow field data is computed. For epochs in which the predicted positions of two stars come within 60 mas of one another (roughly the FWHM of our images), but only one star is actually detected, we exclude that detection as it is likely confused by the undetected source. Ten stars in this work were affected by confusion between 1 and 11 times, and IRS 16CC was confused in 26 epochs by a $K \sim 13$ mag star that has come within $\sim$30 mas since 2004. A total of 79 young star positional measurements were removed due to confusion, leaving 1727 positions for the narrow-field sources combined.

The mosaic star lists are aligned in a similar way as described above, but separately from the deep central and speckle data. The reference epoch chosen for the alignment of these three star lists was the 2008 observation, as this was the mid-point of these data sets. Young stars that are outside the central 10″ field of view and that are identified in all three mosaics are included in the orbital analysis. In other words, the astrometry obtained from the central 10″ data sets takes precedence over the mosaic astrometry. The final analysis includes astrometry for 69 young stars from the central AO + speckle data sets and 47 young stars from the wide field mosaics, bringing the total number of young stars in this work to 116.

As a final step, all positions are placed in an absolute reference frame defined by radio measurements of seven SiO masers (Reid et al., 2007; Yelda et al., 2010). Our star lists thereby consist of positions measured relative to Sgr A*-radio.

3.3.2.3 Proper Motion and Acceleration Measurements

All the x and y positions are independently fit as a function of time with kinematic models. For the central $10''$ field, each star is fit with two models: (1) proper motion only and (2) proper motion and acceleration. Stars detected beyond the central $10''$ field (i.e., those in the wide mosaic fields) have just three positional measurements and are therefore only fit for velocities. The reference time, t_0, for the position, velocity, and acceleration measurements of each star is chosen as the mean time of all epochs, weighted by the star's positional uncertainties. The velocity fits take on the form

$$x(t) = x_0 + v_{x,0}(t - t_0) \tag{3.1}$$

$$y(t) = y_0 + v_{y,0}(t - t_0), \tag{3.2}$$

and the acceleration fits are of the form

$$x(t) = x_0 + v_{x,0}(t - t_0) + \frac{1}{2}a_{x,0}(t - t_0)^2 \tag{3.3}$$

$$y(t) = y_0 + v_{y,0}(t - t_0) + \frac{1}{2}a_{y,0}(t - t_0)^2. \tag{3.4}$$

Whether a star has measurable accelerated motion depends on several factors, including its distance from the supermassive black hole, the time baseline over which it is detected, and the precision with which its positions are measured. In order to determine whether a star's motion is best described by a velocity or

acceleration model, we compare the goodness of fit of the two models using the F-test, where we estimate the quantity

$$F = \frac{\chi^2_{pm}}{\chi^2_{acc}} \tag{3.5}$$

which follows an F-distribution under the null hypothesis (Hays, 1994). Here χ^2_{pm} and χ^2_{acc} are the reduced χ^2 values for the proper motion and acceleration fits, respectively. The test is performed on the X and Y coordinates of the model fits independently. We require that F is greater than the critical F value at the 4σ significance level. In addition, the star must not have a significant ($>5\sigma$) non-physical acceleration (i.e., tangential or positive radial acceleration) and it must be detected in more than 30 out of the 45 possible epochs, which removes the sources that show unphysical accelerations arising from effects such as source confusion (§3.3.2.2) or edge effects in speckle images (§3.3.2.1). With these criteria, we measure accelerations with $>5\sigma$ significance for the following six stars (beyond a projected radius of $0\farcs8$): S0-15, S1-3, IRS 16C, S1-12, S1-14, IRS 16SW, all of which are negative radial and therefore plausibly physical. This increases the number of acceleration measurements beyond $1''$ over our previous work in Lu et al. (2009) by a factor of six, or equivalently, an additional five stars, three of which are reported by Gillessen et al. (2009b). The most distant star from the SMBH for which an acceleration measurement is made is IRS 16SW, located at $R = 1\farcs5$ ($\sim$0.06 pc), which is well outside the inner edge of the stellar disk. For all other sources, the proper motion fit is used.

The position, proper motion, and acceleration errors from the fitting procedure as a function of K magnitude ($\lambda = 2.2$ μm) for young stars in the central $10''$ data set are shown in Figure 3.3. The median errors in positions and proper motions are 0.05 mas and 0.03 mas yr^{-1}, respectively. Stars detected in relatively

more epochs show smaller errors in positions and velocities, as seen in the top panels of Figure 3.3. Acceleration errors are plotted for the six stars that have reliable acceleration measurements, as well as 12 stars with 3σ upper limits below their theoretical maximum acceleration (see §3.4.2). The average acceleration uncertainty among these stars is 10 μas yr^{-2} ($\sim$0.4 km s^{-1} yr^{-1}), which is a factor of six improvement over our earlier efforts in Lu et al. (2009). These measurements match and sometimes exceed the highest astrometric precision that has been reported to date (Gillessen et al., 2009b). For completeness, we show the radial velocity uncertainties for all 116 young stars in the sample and indicate the source of the measurement that we use in our analysis (i.e., Keck/OSIRIS or VLT/SINFONI).

The position and proper motion measurements of stars at large radii and detected in only the wide mosaics have typical uncertainties of 0.4 mas and 0.23 mas yr^{-1}, respectively. The relatively high uncertainties, as compared to stars in the narrow field, are a result of having only three measurements and a four-year baseline. We present the positions, proper motions, and accelerations for our sample in Table 3.4.

3.3.3 Radial Velocities

OSIRIS radial velocity estimates were made by comparing the observed location of the Brγ line to its rest wavelength of $\lambda_0 = 2.1661$ μm. The velocities are then transformed to the local standard of rest (LSR) reference frame by correcting for the Earth's rotation and motion around the sun, and for the Sun's peculiar motion. RV uncertainties (σ_{RV}) from OSIRIS are estimated as the rms of the line profile fits from three independent subsets of the original data. Uncertainties range from $\sim$10-90 km s^{-1} and are reported in Table 3.4. Only one frame,

however, was obtained for the star S1-24 ($K = 11.5$), and had a signal-to-noise ratio of $SNR = 74$. Given this relatively high SNR, we choose to include this RV measurement and we estimate its uncertainty using an empirically-derived relation between SNR and σ_{RV}:

$$\sigma_{RV} = 175.4 \times SNR^{-0.367}. \tag{3.6}$$

Further details on the RV extraction process are reported in Ghez et al. (2008).

If multiple RV measurements exist, the Keck measurements take precedence, followed by the VLT measurements reported in Bartko et al. (2009) and Paumard et al. (2006). This results in a sample of RV measurements, of which 38 were made with OSIRIS, and 78 were taken from either Bartko et al. (2009) or Paumard et al. (2006). The 15 stars that are in common between the Do et al. OSIRIS observations and the VLT observations have a median radial velocity difference of $\sim$55 km s^{-1}. Changing the reference from which the radial velocities are pulled for these 15 stars does not change the results presented here. We note that the Do et al., (in prep.) observations were designed to sample the eastern portion of the clockwise disk in order to maximize the number of young star identifications. With observed K magnitudes ranging from $\sim$9-15.5, the Do et al. samples include WR stars at the bright end and B1V stars at the faint end. In contrast, Bartko et al. (2009) include only WR and O-type stars ($K < 14$), all 90 of which are included in our sample. Here we report OSIRIS radial velocities for 38 young stars. Our spectroscopic sample contains the most extensive survey within the clockwise disk plane to date.

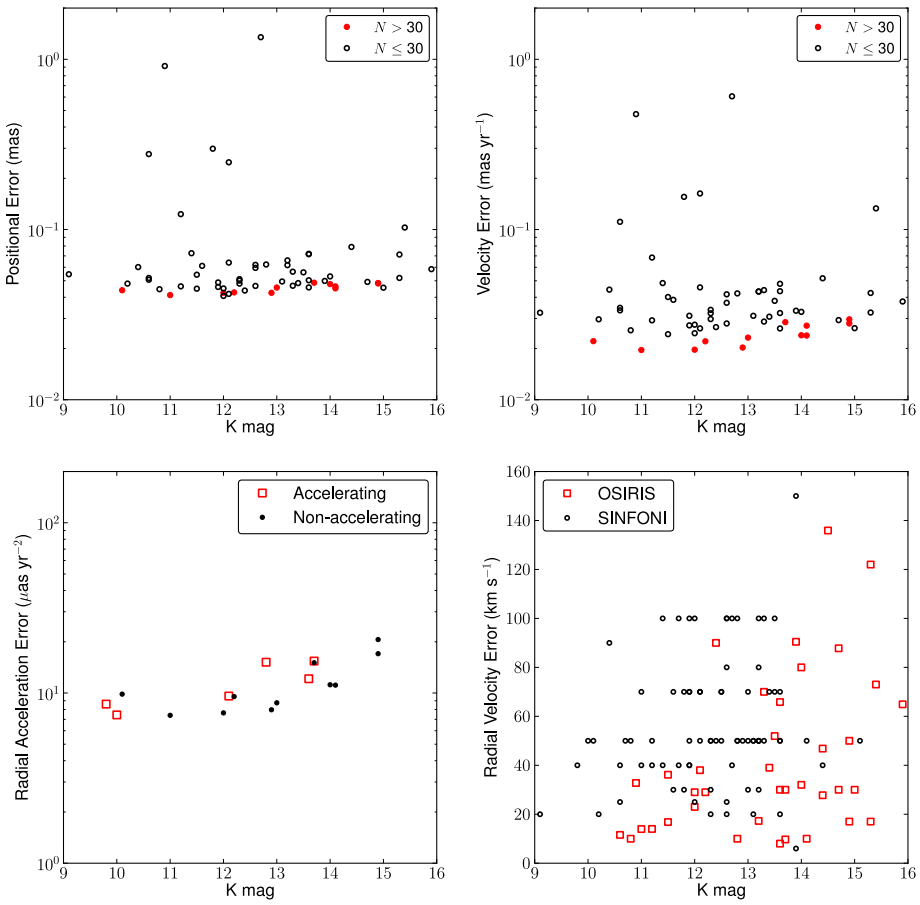

Figure 3.3 Position (*top left*), proper motion (*top right*), and acceleration (*bottom left*) errors as a function of K magnitude for our sample of young stars beyond a projected radius of 0.″8 and in the central 10″ AO data set. The astrometric errors are estimated from either the proper motion or acceleration fit to each star's individual positions over time. Stars with $N > 30$ epochs (*filled red points*) have smaller errors in position and proper motion than stars in fewer epochs (*open circles*). The radial acceleration errors are shown for stars in $N > 30$ epochs, where we separately plot those six stars passing the F test for accelerations (*open red squares*) and those stars for which no detectable accelerations are found (*filled black points*), requiring a non-zero line-of-sight distance. The average acceleration uncertainty among these stars is 10 μas yr^{-2} ($\sim$0.4 km s^{-1} yr^{-1}). We also show for completeness the errors in the line-of-sight velocity as a function of K magnitude (*bottom right*), where we identify the source of the measurement (Keck/OSIRIS and VLT/SINFONI).

Table 3.4. Kinematic Data of Galactic Center Young Stars

Name	K (mag)	N	Epoch (year)	Radius (arcsec)	ΔRA [a] (arcsec)	ΔDEC [a] (arcsec)	v_{ra} (mas/yr)	v_{dec} (mas/yr)	v_z (km/s)	v_z [b] Ref	a_ρ [c] (mas/yr^2)	1 - LH (non-disk)	Disk Cand.
Stars with Acceleration Detections													
S1-3	12.1	45	2007.7	0.96	0.357	0.888	-13.70 ± 0.02	1.73 ± 0.03	-72 ± 38	1	-0.160 ± 0.010	0.415	Yes
S0-15	13.6	43	2007.6	0.99	-0.962	0.214	-3.47 ± 0.02	-10.82 ± 0.03	-597 ± 8	1	-0.293 ± 0.012	0.950	Yes
irs16C	9.8	45	2007.5	1.20	1.068	0.539	-8.54 ± 0.02	7.72 ± 0.02	158 ± 40	2	-0.083 ± 0.009	0.447	Yes
S1-12	13.7	36	2007.8	1.28	-0.777	-1.016	10.84 ± 0.02	-2.42 ± 0.03	-34 ± 30	1	-0.082 ± 0.015	0.487	Yes
S1-14	12.8	40	2007.8	1.38	-1.332	-0.349	4.96 ± 0.02	-7.39 ± 0.03	-364 ± 10	1	-0.123 ± 0.015	0.497	Yes
irs16SW	10.0	45	2007.3	1.45	1.091	-0.952	7.37 ± 0.02	2.97 ± 0.02	470 ± 50	2	-0.074 ± 0.007	0.082	Yes
Stars with Acceleration Constraints													
S0-14	13.7	36	2007.9	0.81	-0.764	-0.277	2.16 ± 0.02	-0.93 ± 0.03	-16 ± 9	1	> -0.120	0.011	Yes
S1-1	13.0	45	2007.7	1.03	1.027	0.037	5.62 ± 0.02	1.62 ± 0.03	536 ± 30	2	> -0.025	0.000	No
irs16NW	10.1	45	2007.6	1.22	0.064	1.223	5.79 ± 0.02	1.21 ± 0.03	-15 ± 50	2	> -0.045	0.000	No
S1-33	14.9	35	2008.0	1.25	-1.246	-0.007	-0.34 ± 0.02	5.55 ± 0.03	3 ± 17	1	> -0.110	0.000	No
S1-18	14.9	43	2007.8	1.69	-0.773	1.508	-7.63 ± 0.02	1.13 ± 0.03	-249 ± 50	1	> -0.050	0.022	Yes
S1-22	12.7	32	2007.8	1.67	-1.588	-0.509	7.73 ± 0.02	-2.60 ± 0.03	-235 ± 100	2	> -0.122	0.201	Yes
S2-4	12.2	35	2007.6	2.09	1.498	-1.459	7.94 ± 0.02	3.07 ± 0.03	208 ± 29	1	> -0.023	0.205	Yes
S2-7	14.1	42	2007.7	2.08	0.943	1.853	-6.61 ± 0.02	1.83 ± 0.03	-94 ± 50	3	> -0.053	0.228	Yes
S2-6	12.0	38	2007.6	2.11	1.641	-1.332	7.85 ± 0.02	2.33 ± 0.02	148 ± 29	1	> -0.020	0.068	Yes
irs16SW-E	11.0	39	2007.6	2.19	1.880	-1.120	5.87 ± 0.02	3.89 ± 0.02	366 ± 70	2,3	> -0.028	0.047	Yes
S2-22	12.9	44	2007.7	2.31	2.304	-0.214	-1.63 ± 0.02	6.42 ± 0.02	49 ± 50	2	> -0.040	0.000	No
S2-58	14.0	37	2007.9	2.43	2.146	-1.134	-0.73 ± 0.02	6.62 ± 0.03	63 ± 32	1	> -0.040	0.000	No

Table 3.4—Continued

Name	K (mag)	N	Epoch (year)	Radius (arcsec)	ΔRA [a] (arcsec)	ΔDEC [a] (arcsec)	v_{ra} (mas/yr)	v_{dec} (mas/yr)	v_z (km/s)	v_z [b] Ref	a_ρ [c] (mas/yr^2)	1 - LH (non-disk)	Disk Cand.
Linearly-Moving Stars													
S1-2	14.7	30	2007.8	1.01	0.046	-1.011	13.10 ± 0.02	-0.12 ± 0.03	34 ± 30	1		0.286	Yes
S1-8	14.1	41	2007.7	1.08	-0.606	-0.898	9.05 ± 0.02	-5.24 ± 0.03	-171 ± 10	1		0.500	Yes
S1-21	13.3	27	2007.9	1.65	-1.650	0.109	4.02 ± 0.02	-4.79 ± 0.03	-29 ± 70	1		0.132	Yes
S1-19	13.6	29	2007.7	1.67	0.411	-1.623	8.41 ± 0.02	-3.11 ± 0.03	-164 ± 30	1		0.205	Yes
S1-24	11.5	30	2007.7	1.79	0.728	-1.631	2.64 ± 0.02	-6.16 ± 0.03	206 ± 30	2,3		0.000	No
irs16CC	10.6	19	2001.3	2.07	1.997	0.545	-1.72 ± 0.11	6.79 ± 0.11	241 ± 25	2,3		0.391	Yes
irs29N	10.4	17	2009.0	2.08	-1.560	1.381	4.75 ± 0.04	-5.05 ± 0.05	-190 ± 90	2,3		0.034	Yes
irs33N	11.2	20	2007.8	2.22	-0.037	-2.222	3.62 ± 0.02	-5.54 ± 0.03	20 ± 14	1		0.000	No
S2-50	15.3	24	2008.1	2.27	1.696	-1.503	2.25 ± 0.04	2.22 ± 0.04	-56 ± 122	1		0.275	Yes
S2-17	10.8	25	2007.9	2.29	1.323	-1.871	9.24 ± 0.02	0.15 ± 0.03	62 ± 10	1		0.296	Yes
S2-16	11.9	23	2008.0	2.32	-1.052	2.066	-9.16 ± 0.02	-0.61 ± 0.03	-100 ± 70	2,3		0.730	Yes
S2-21	13.4	20	2007.8	2.33	-1.641	-1.658	9.35 ± 0.03	-3.33 ± 0.04	-109 ± 39	1		0.476	Yes
S2-19	12.6	24	2007.8	2.34	0.398	2.311	-8.28 ± 0.02	1.32 ± 0.03	41 ± 20	2,3		0.346	Yes
S2-74	13.1	19	2007.8	2.78	0.134	2.781	-8.84 ± 0.03	1.55 ± 0.03	36 ± 20	2,3		0.276	Yes
S2-76	15.4	9	2010.2	2.82	-0.225	2.811	2.81 ± 0.12	1.86 ± 0.15	-28 ± 73	1		0.000	No
irs16NE	9.1	26	2008.0	3.05	2.888	0.981	3.05 ± 0.03	-8.90 ± 0.04	-10 ± 20	2,3		0.000	No
S3-2	12.0	24	2007.9	3.13	3.076	0.555	4.31 ± 0.02	1.30 ± 0.03	-446 ± 23	1		0.000	No
S3-3	15.0	22	2008.1	3.15	3.082	-0.645	3.76 ± 0.02	4.57 ± 0.03	43 ± 30	1		0.000	No
S3-5	12.0	22	2008.0	3.17	2.953	-1.153	2.87 ± 0.02	4.94 ± 0.03	327 ± 100	2,3		0.430	Yes
S3-96	14.4	17	2008.9	3.19	-3.133	-0.627	-0.07 ± 0.04	5.64 ± 0.06	40 ± 40	2,3		0.000	No

Table 3.4—Continued

Name	K (mag)	N	Epoch (year)	Radius (arcsec)	ΔRA [a] (arcsec)	ΔDEC [a] (arcsec)	v_{ra} (mas/yr)	v_{dec} (mas/yr)	v_z (km/s)	v_z [b] Ref	a_ρ [c] (mas/yr^2)	1 - LH (non-disk)	Disk Cand.
S3-19	11.9	19	2007.9	3.20	-1.566	-2.786	7.90 ± 0.03	-1.30 ± 0.04	-114 ± 50	2,3		0.317	Yes
irs33E	10.2	19	2008.0	3.20	0.691	-3.127	6.85 ± 0.02	-1.06 ± 0.04	170 ± 20	2,3		0.026	Yes
S3-25	13.9	19	2007.6	3.28	1.424	2.959	-7.08 ± 0.03	0.77 ± 0.04	-84 ± 6	2		0.195	Yes
S3-26	12.3	19	2007.8	3.31	-2.588	-2.069	5.80 ± 0.03	2.12 ± 0.04	63 ± 30	2,3		0.085	Yes
S3-30	12.4	19	2008.0	3.37	1.661	-2.937	-0.72 ± 0.02	4.32 ± 0.03	0 ± 90	1		0.018	Yes
irs13E1	10.6	19	2007.8	3.40	-2.971	-1.647	-3.87 ± 0.03	-1.98 ± 0.04	-3 ± 11	1		0.000	No
S3-190	14.0	19	2008.2	3.49	-3.186	1.423	-3.27 ± 0.03	-2.29 ± 0.04	-244 ± 80	1		0.215	Yes
S3-10	12.1	19	2008.0	3.52	3.340	-1.113	-0.14 ± 0.02	5.50 ± 0.03	305 ± 70	2		0.427	Yes
irs13E4	11.8	19	2008.1	3.52	-3.231	-1.403	-5.77 ± 0.17	1.70 ± 0.14	56 ± 70	2,3		0.000	No
irs13E2	10.6	19	2007.7	3.63	-3.190	-1.726	-6.78 ± 0.03	1.43 ± 0.04	40 ± 40	2,3		0.000	No
S3-314	15.3	19	2007.9	3.83	3.829	-0.090	3.08 ± 0.03	4.16 ± 0.04	11 ± 17	1		0.000	No
S3-331	13.6	19	2008.0	3.85	-1.238	3.650	5.70 ± 0.04	4.64 ± 0.05	-167 ± 20	2,3		0.000	No
S3-374	12.3	19	2007.7	3.95	-2.757	-2.835	-0.49 ± 0.03	-3.78 ± 0.04	20 ± 20	2		0.000	No
S4-36	12.6	19	2007.8	4.10	-3.685	1.794	-5.37 ± 0.03	-3.92 ± 0.04	-154 ± 25	2,3		0.345	Yes
S4-71	12.3	18	2008.0	4.15	0.769	-4.076	0.12 ± 0.02	-4.28 ± 0.04	60 ± 50	2		0.000	No
irs34W	11.6	19	2007.9	4.36	-4.066	1.570	-2.66 ± 0.04	-4.89 ± 0.04	-290 ± 30	2,3		0.441	Yes
S4-169	13.5	18	2007.8	4.43	4.417	0.274	-2.28 ± 0.03	4.42 ± 0.05	145 ± 51	1		0.555	Yes
irs3E	11.4	19	2007.8	4.47	-2.338	3.816	4.61 ± 0.04	1.19 ± 0.05	107 ± 100	3		0.000	No
irs7SE	13.3	19	2007.3	4.57	2.976	3.469	5.84 ± 0.04	0.22 ± 0.05	-150 ± 100	2,3		0.000	No
S4-258	12.6	19	2007.5	4.68	-4.392	-1.630	-4.70 ± 0.04	2.45 ± 0.05	330 ± 80	2,3		0.000	No
S4-262	15.9	17	2008.1	4.70	4.280	-1.939	-1.25 ± 0.03	-5.09 ± 0.05	43 ± 64	1		0.000	No

Table 3.4—Continued

Name	K (mag)	N	Epoch (year)	Radius (arcsec)	ΔRA [a] (arcsec)	ΔDEC [a] (arcsec)	v_{ra} (mas/yr)	v_{dec} (mas/yr)	v_z (km/s)	v_z [b] Ref	a_ρ [c] (mas/yr^2)	1 - LH (non-disk)	Disk Cand.
irs34NW	13.2	16	2007.7	4.72	-3.766	2.839	-5.94 ± 0.04	-3.33 ± 0.05	-150 ± 30	2,3		0.519	Yes
S4-287	13.6	17	2007.8	4.77	0.125	-4.767	2.97 ± 0.02	1.57 ± 0.04	-51 ± 65	1		0.058	Yes
S4-364	11.7	3	2007.8	5.00	2.224	4.481	5.77 ± 0.20	-2.30 ± 0.22	-134 ± 40	2,3		0.000	No
S5-34	13.6	19	2007.6	5.12	-4.329	-2.731	-3.61 ± 0.04	-1.68 ± 0.05	-40 ± 70	2		0.000	No
irs1W	10.9	15	2008.3	5.29	5.255	0.620	-1.35 ± 0.21	9.66 ± 0.74	-36 ± 32	1		0.000	No
S5-235	13.2	3	2007.8	5.34	2.781	4.553	-1.14 ± 0.20	-3.77 ± 0.22	-115 ± 50	2		0.000	No
S5-237	13.2	3	2007.8	5.59	5.500	1.002	-1.33 ± 0.23	6.44 ± 0.18	35 ± 17	1		0.000	No
S5-236	13.1	3	2008.4	5.69	-5.547	-1.282	4.43 ± 0.22	1.95 ± 0.21	155 ± 50	2		0.000	No
S5-183	11.5	17	2007.4	5.74	4.604	-3.431	-4.29 ± 0.03	-1.90 ± 0.05	-148 ± 16	1		0.000	No
S5-187	13.2	17	2007.5	5.79	-1.712	-5.532	-0.97 ± 0.03	-3.76 ± 0.05	10 ± 50	2		0.000	No
S5-231	12.0	3	2008.4	5.81	5.813	0.097	0.02 ± 0.56	6.04 ± 0.17	24 ± 25	2		0.000	No
S5-191	12.8	17	2007.9	5.82	3.184	-4.872	-1.35 ± 0.03	-3.54 ± 0.05	140 ± 50	2		0.000	No
S6-89	12.1	16	2009.2	6.22	5.445	3.013	3.05 ± 0.16	-6.01 ± 0.16	-135 ± 70	2		0.000	No
irs9W	12.1	17	2007.4	6.29	2.882	-5.593	5.62 ± 0.03	3.58 ± 0.06	140 ± 50	2,3		0.422	Yes
S6-90	12.3	3	2007.9	6.32	-3.954	4.924	-0.50 ± 0.24	-2.93 ± 0.23	-350 ± 50	2,3		0.005	Yes
S6-96	12.8	3	2006.9	6.35	-6.045	-1.940	-1.35 ± 0.37	8.38 ± 0.57	-35 ± 50	2		0.000	No
S6-81	11.0	3	2008.1	6.37	6.360	0.267	-2.16 ± 0.20	5.34 ± 0.15	-14 ± 13	1		0.000	No
S6-95	13.2	3	2008.1	6.47	-2.420	6.004	4.02 ± 0.22	0.77 ± 0.22	-305 ± 100	2,3		0.000	No
S6-63	11.2	17	2007.9	6.57	1.852	-6.306	6.04 ± 0.05	1.80 ± 0.09	110 ± 50	2		0.611	Yes
S6-93	12.8	3	2008.1	6.67	4.448	4.973	4.69 ± 0.21	-0.85 ± 0.20	-80 ± 100	2,3		0.000	No
S6-100	13.9	3	2008.0	6.71	1.562	6.524	-4.87 ± 0.22	2.87 ± 0.20	-300 ± 150	3		0.016	Yes

Table 3.4—Continued

Name	K (mag)	N	Epoch (year)	Radius (arcsec)	ΔRA [a] (arcsec)	ΔDEC [a] (arcsec)	v_{ra} (mas/yr)	v_{dec} (mas/yr)	v_z (km/s)	v_z [b] Ref	a_ρ [c] (mas/yr^2)	1 - LH (non-disk)	Disk Cand.
S6-82	13.5	3	2007.5	6.73	6.715	-0.470	2.07 ± 0.19	5.68 ± 0.26	86 ± 100	2,3		0.184	Yes
S7-30	13.9	3	2008.4	7.00	6.469	-2.682	-2.63 ± 0.19	-3.32 ± 0.15	-87 ± 90	1		0.000	No
S7-161	13.6	3	2009.5	7.38	-7.376	0.061	-2.16 ± 0.49	-2.55 ± 0.40	-120 ± 50	2		0.333	Yes
S7-16	12.5	3	2008.1	7.41	1.621	-7.236	2.49 ± 0.21	3.30 ± 0.23	160 ± 50	2		0.264	Yes
S7-19	13.2	3	2007.8	7.53	-3.794	6.507	4.22 ± 0.24	3.52 ± 0.19	-65 ± 50	2		0.000	No
S7-180	13.4	3	2008.9	7.54	-7.360	-1.637	-3.92 ± 0.28	0.48 ± 0.29	120 ± 70	2		0.000	No
S7-10	11.4	3	2008.1	7.71	-1.105	7.635	-5.14 ± 0.19	-1.87 ± 0.16	-92 ± 40	2,3		0.474	Yes
S7-36	14.4	3	2008.5	7.74	6.363	-4.415	2.63 ± 0.20	2.33 ± 0.16	26 ± 46	1		0.180	Yes
S7-216	10.7	3	2008.4	7.86	-7.731	1.424	1.82 ± 0.24	6.59 ± 0.23	60 ± 50	2		0.000	No
S7-20	13.3	3	2008.4	7.88	-3.700	6.955	4.11 ± 0.26	2.89 ± 0.26	-45 ± 50	2		0.000	No
S7-228	11.8	3	2008.3	7.93	-7.741	1.708	2.19 ± 0.26	3.67 ± 0.23	150 ± 30	2		0.000	No
S7-236	12.5	3	2007.7	7.95	-7.093	3.598	-3.65 ± 0.28	-2.59 ± 0.25	-170 ± 70	2		0.681	Yes
S8-15	13.0	3	2008.2	8.20	-1.603	8.043	-3.30 ± 0.20	-2.64 ± 0.16	-130 ± 50	2		0.387	Yes
S8-7	11.9	3	2008.3	8.28	-3.688	-7.415	4.53 ± 0.20	0.54 ± 0.19	30 ± 100	2		0.516	Yes
S8-181	11.6	3	2007.9	8.42	-7.620	-3.580	-2.15 ± 0.24	-1.90 ± 0.20	70 ± 70	2,3		0.005	Yes
S8-4	11.0	3	2008.3	8.56	-0.021	8.560	-0.92 ± 0.18	3.81 ± 0.16	-138 ± 40	2,3		0.000	No
S8-196	12.4	3	2008.4	8.59	-8.087	-2.896	0.16 ± 0.26	-0.14 ± 0.21	190 ± 50	2		0.000	No
S9-143	12.6	3	2008.1	9.01	-8.365	-3.347	-0.33 ± 0.25	-1.29 ± 0.21	40 ± 100	2		0.112	Yes
S9-20	13.2	3	2007.8	9.11	4.304	-8.031	2.55 ± 0.27	1.48 ± 0.21	180 ± 80	2,3		0.227	Yes
S9-23	13.6	3	2008.2	9.24	-1.277	9.151	-3.89 ± 0.18	-3.43 ± 0.17	-185 ± 50	2		0.156	Yes
S9-13	13.1	3	2008.2	9.32	-3.019	8.821	2.00 ± 0.19	3.68 ± 0.20	-160 ± 50	2		0.000	No

Table 3.4—Continued

Name	K (mag)	N	Epoch (year)	Radius (arcsec)	ΔRA [a] (arcsec)	ΔDEC [a] (arcsec)	v_{ra} (mas/yr)	v_{dec} (mas/yr)	v_z (km/s)	v_z [b] Ref	a_ρ [c] (mas/yr^2)	1 - LH (non-disk)	Disk Cand.
S9-1	12.6	3	2008.4	9.45	9.450	0.281	-1.79 ± 0.18	-2.59 ± 0.16	-230 ± 100	2,3		0.000	No
S9-114	10.8	3	2008.3	9.48	-6.509	-6.886	2.08 ± 0.20	3.22 ± 0.18	160 ± 50	2		0.000	No
S9-283	12.5	3	2008.1	9.93	-9.605	-2.539	0.80 ± 0.23	1.00 ± 0.21	30 ± 70	2,3		0.000	No
S9-9	11.7	3	2008.4	9.94	5.650	-8.182	-0.91 ± 0.18	-1.18 ± 0.17	130 ± 100	2,3		0.000	No
S10-50	14.7	3	2008.2	10.09	9.586	-3.160	-0.48 ± 0.21	-3.88 ± 0.16	96 ± 87	1		0.000	No
S10-136	13.0	3	2007.9	10.12	-8.624	-5.289	-1.76 ± 0.27	6.04 ± 0.26	-70 ± 70	2,3		0.000	No
S10-5	11.9	3	2008.3	10.16	-1.574	10.039	-1.67 ± 0.18	-1.18 ± 0.21	-180 ± 70	2,3		0.047	Yes
S10-4	11.2	3	2008.1	10.25	0.078	10.254	-2.09 ± 0.19	1.56 ± 0.21	-250 ± 40	2,3		0.000	No
S10-32	14.4	3	2008.3	10.34	10.200	-1.694	3.41 ± 0.18	3.68 ± 0.16	161 ± 27	1		0.366	Yes
S10-34	14.5	3	2008.4	10.51	8.877	-5.626	1.08 ± 0.23	3.76 ± 0.24	-107 ± 135	1		0.059	Yes
S10-7	12.7	3	2008.0	10.67	9.709	4.428	-0.34 ± 0.21	-4.24 ± 0.20	-150 ± 40	2,3		0.000	No
S10-48	15.1	3	2007.2	10.75	-0.533	10.732	2.01 ± 0.22	1.56 ± 0.44	-205 ± 50	3		0.000	No
S11-21	13.5	3	2008.0	11.24	2.566	10.947	-2.08 ± 0.22	-1.78 ± 0.24	-160 ± 70	2		0.075	Yes
S11-5	11.9	3	2007.9	11.77	1.370	11.693	-0.26 ± 0.21	2.64 ± 0.30	-65 ± 40	2,3		0.000	No
S13-3	11.9	3	2008.3	13.29	11.895	5.932	1.31 ± 0.20	2.28 ± 0.19	-190 ± 40	3		0.000	No

Note. — All uncertainties are 1σ relative errors and do not include errors in the plate scale, location of Sgr A*, or position angle.

[a]Positions relative to Sgr A* as determined from polynomial fitting. Relative errors are, on average, ∼0.1 mas and ∼0.4 mas for central $10''$ and mosaic stars, respectively.

[b]Radial velocity data obtained from observations in (1) Do et al. (2009a) and Do et al. (in prep), (2) Bartko et al. (2009), and (3) Paumard et al. (2006). Note that some RV measurements reported in Bartko et al. (2009) were first reported in Paumard et al. (2006).

[c]Accelerations were fit for stars falling within the central $10''$ field of view only.

3.4 Orbital Analysis

With six kinematic variables measured (x_0, y_0, v_x, v_y, v_z, a_R), the orbital elements can be estimated if the black hole properties are known. We use updated SMBH properties based on the kinematic measurements of the 16-year period star, S0-2. We estimate uncertainties in the orbital period (P), eccentricity (e), inclination (i), angle to the ascending node (Ω), longitude of periapse (ω), and time of periapase passage (T_0) by carrying out a Monte Carlo simulation in which we create 10^5 artificial data sets. In each data set, we sample the six kinematic measurements, as well as the gravitational potential parameters, from Gaussian distributions (except for the acceleration in the case of non-accelerating stars; see §3.4.2 below), which has a mean and 1σ width corresponding to the variable's measured value and uncertainty. This procedure produces a probability density function (PDF) for each orbital element. Our sample has a radial extent that is a factor of $\sim$3 larger than in our previous efforts (Lu et al., 2009), so we include an extended mass component in addition to the central point mass in describing the gravitational potential. We describe our use of the gravitational potential parameters and acceleration information in more detail below.

3.4.1 Enclosed Mass

Given the radial extent of the data ($R < 14'' \sim 0.5$ pc), we assume that the enclosed mass is composed of the central supermassive black hole and an extended mass component from the nuclear stellar cluster. The properties of the supermassive black hole are best determined using the orbit of the 16-year period central-arcsecond star, S0-2 (Ghez et al., 2008; Gillessen et al., 2009b). In this work, we rederive the black hole properties using (1) the astrometry from the aligned star lists reported here to ensure that the position of Sgr A* is identified

in the same reference frame as our stellar kinematic measurements, and (2) all radial velocities used by Ghez et al. (2008) and newly acquired data from OSIRIS since that work[3]. This results in a black hole mass of 4.6 ± 0.7 $\times 10^6$ $M_\odot$ and a distance of $R_0 = 8.23 \pm 0.67$ kpc. We incorporate shifts of the dynamical center in the reference frame, which is on the order of a few mas. However, given that the stars are at projected radii $R \sim 1''$-$10''$, we do not expect that this will impact the results presented here.

Following Schödel et al. (2009), we take the extended mass distribution as a function of the star's 3-dimensional distance to be

$$M_{ext} = 4\pi \int \rho(r) r^2 dr, \tag{3.7}$$

where the mass density, $\rho(r)$, is a power-law of the form

$$\rho(r) = \rho_0 \left(\frac{r}{r_M} \right)^{-\Gamma}. \tag{3.8}$$

The extended mass component is roughly $M_{ext}(r < 1 \text{ pc}) \sim 1 \pm 0.4 \times 10^6$ $M_\odot$, where the error is taken as the difference in extended mass estimates from isotropic and anisotropic velocity models in Schödel et al. (2009). Given this uncertainty in M_{ext}, the mass density normalization ρ_0 for $r_M = 5$ pc ($\sim 100''$) and $\Gamma = 1$ is $\rho_0 = 3.2 \pm 1.3 \times 10^4$ $M_\odot\,\text{pc}^{-3}$. While we do not know the line-of-sight distance (and therefore the full 3D distance) *a priori*, we use the star's projected radius to determine M_{ext}, which is a lower limit on the true extended mass. For the radial range of our data, the above assumptions lead to $M_{ext} < 5 \times 10^5$ $M_\odot$, which is an order of magnitude smaller than the mass of the SMBH

[3]Since the analysis presented here, the black hole properties were rederived after including the most recent imaging observation from Keck in 2012 May, as well as all currently published radial velocity data (Meyer et al., in press). The newly-derived black hole mass and distance are consistent with the values we use to within 1σ.

and should therefore have a minimal effect on the orbital estimates.

In each trial of the Monte Carlo simulations, we randomly select a black hole mass M_{BH}, distance R_0, origin (x_0, y_0), and mass density normalization constant ρ_0, pulled from a Gaussian distribution with mean and 1σ width corresponding to the values stated above. In a given trial, all 116 stars' orbits are determined using the same gravitational potential.

3.4.2 Constraining the z-coordinate with Accelerations

The line-of-sight distance, z, can be determined for stars that show significant deviations from linear motion in the plane of the sky. As described in Lu et al. (2009), the acceleration and the line-of-sight distance relative to the central mass, M, are related as

$$a_R = \frac{-GMR}{r^3} = \frac{-GMR}{(R^2 + z^2)^{3/2}}. \tag{3.9}$$

Here R is the star's projected radius relative to Sgr A* and a_R is the acceleration in the plane of the sky along the radial direction.

In each MC trial for the six stars with accelerations, we sample an acceleration from a Gaussian distribution centered on the best fit a_R with a 1σ width equivalent to the uncertainty in the measurement. We convert the sampled a_R to a line-of-sight distance by rearranging Equation 3.9:

$$z = \left[\left(\frac{GMR}{a_R}\right)^{2/3} - R^2\right]^{1/2}, \tag{3.10}$$

where M and R are the randomly sampled enclosed mass and 2-dimensional radius, respectively. We note that there is a sign ambiguity in the line-of-sight distance, which results in degenerate orbital solutions.

On the other hand, accelerations that are consistent with zero can still provide

constraints on the line-of-sight distance. As described in Lu et al. (2009), the maximum acceleration a star can have is $|a|_{z0} = GM/R^2$, which is equivalent to the acceleration the star would have if its line-of-sight distance were $z = 0$. A star with a 3σ acceleration upper limit, $|a|_{3\sigma}$, that is less than $|a|_{z0}$ must therefore have a 3-dimensional position that is larger than its observed projected position (i.e., $|z| > 0$). Thus, the non-detection of an acceleration translates to a lower limit on the line-of-sight distance. Furthermore, the minimum acceleration allowed, $|a|_{bound}$, is set by the assumption that the star is bound. For stars with 3σ upper limits below $|a|_{z0}$, we sample from a uniform acceleration distribution between a_{bound} and $a_{3\sigma}$. For all other stars, including those outside the central $10''$ field (i.e., stars from the mosaic fields), we sample from a uniform acceleration distribution between a_{bound} and a_{z0}.

Each trial in the MC simulation has a unique maximum acceleration, a_{z0}, as a function of radius since the mass is sampled at the beginning of each trial. We check for unbound orbits or for the selection of accelerations $|a_R| > |a|_{z0}$ within each trial, and resample the kinematic variables in these cases.

Figure 3.4 shows the radial acceleration measurements as a function of projected radius for stars in the central $10''$ field for which we have acceleration information. The six significant accelerations are shown with 1σ error bars. An additional 12 stars have 3σ upper limits below or equivalent to the nominal theoretical maximum acceleration and for which the line-of-sight distance is constrained to $z \geq 0$ (shown as downward-pointing arrows).

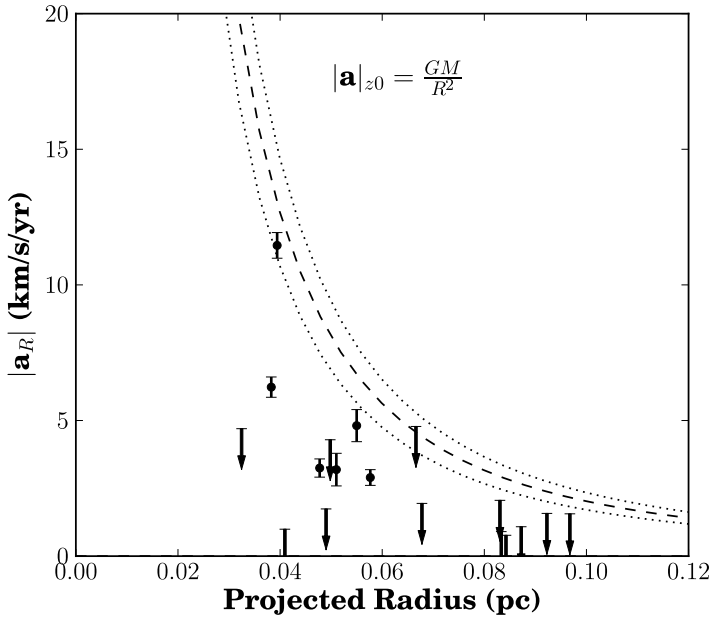

Figure 3.4 Accelerations along the radial coordinate as a function of the stars' projected radius. The theoretical maximum acceleration ($|a|_{z0}$) for the nominal black hole mass of 4.6×10^6 $M_\odot$ is shown as the dashed curve, with the 1σ upper and lower boundaries shown as dotted curves. We detect six significant accelerations out to R=1.″5 (0.06 pc), shown with 1σ error bars. These sources have known line-of-sight distances and therefore have the best-determined orbital solutions. Stars with 3σ acceleration upper limits below the theoretical maximum acceleration are shown as downward pointing arrows and have strong constraints on their line-of-sight distances ($|z| > 0$).

3.5 Results

3.5.1 Stellar Orbits

Orbital parameter estimates of stars with detected accelerations will be the most precisely determined as the magnitude of the line-of-sight distance to these stars is known. The line-of-sight distances to the six accelerating stars in our sample are determined to within $\sim$0.01 pc (1σ). Figures 3.5 and 3.6 show the e, i, and Ω PDFs as a function of z for these sources. The PDFs are constrained to small regions of parameter space for positive and negative z. Each of the degenerate solutions in i and Ω have 1σ widths of $<5^{\circ}$. The eccentricities are determined to within 0.1 (1σ) for all of these sources.

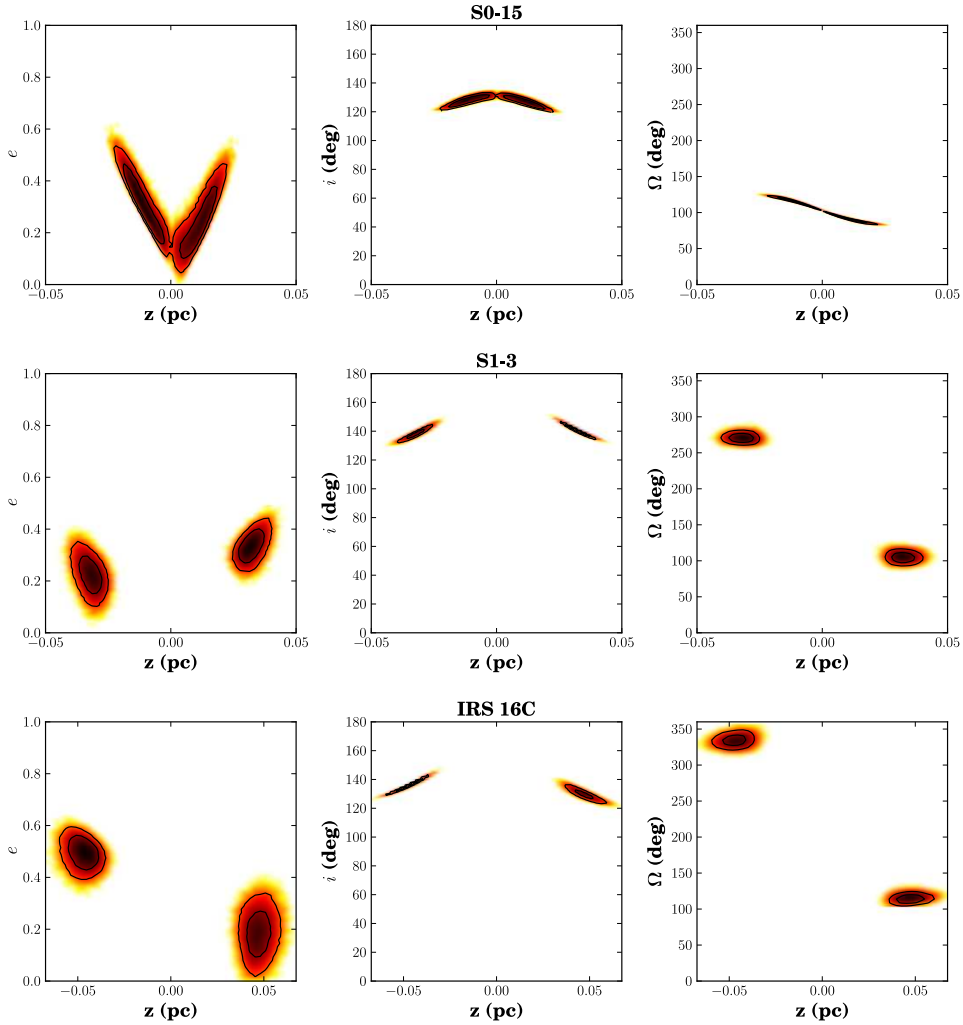

Figure 3.5 The probability distribution functions for eccentricity (*left*), inclination (*middle*), and angle to the ascending node (*right*) as a function of the line-of-sight distance for the six stars with significant accelerations in the plane of the sky. The absolute value of the line-of-sight distance, $|z|$, is precisely determined for each of these stars from their measured accelerations. The sign ambiguity of z results in the degenerate set of solutions. The stars S0-15 and S1-14 have solutions consistent with z=0. The 1σ and 2σ contours of the PDFs are overplotted as solid lines.

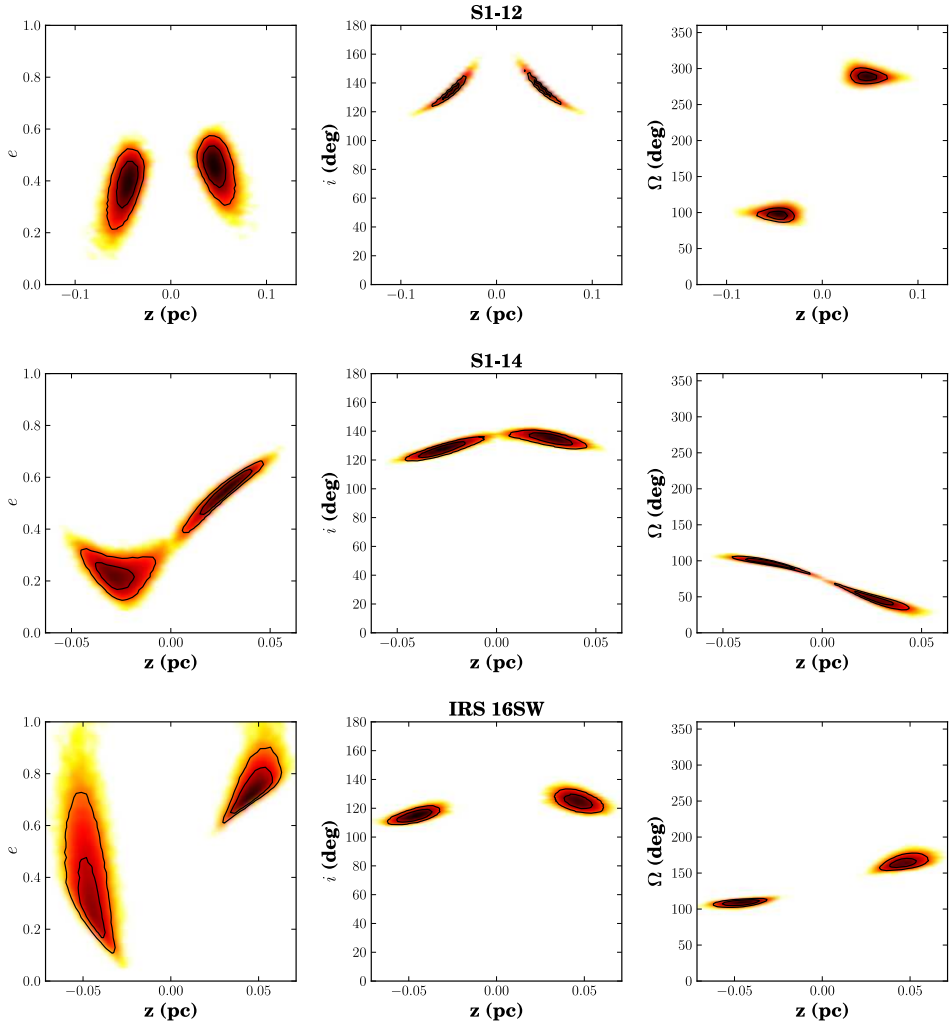

Figure 3.6 Same as Figure 3.5, for S1-12, S1-14, and IRS 16SW.

3.5.2 Clockwise Disk Membership

To identify the clockwise disk structure in our analysis and assign disk membership we construct a density map of the stars' orbital plane normal vectors. Figure 3.7 shows the density of normal vectors (in stars deg^{-2}) from the MC simulations for all 116 stars. The direction of the normal vector is described by

inclination, i, and the position angle of the ascending node, Ω, which are shown as the latitudinal and longitudinal lines in Figure 3.7, respectively. The density at each location in the PDF(i, Ω) map is computed for the six nearest normal vectors within a given trial in the MC simulation (Lu et al., 2009). These values are then averaged over all 10^5 trials and an average density map is obtained.

To quantify the significance of any structures in the normal vector density maps, we run 1000 Monte Carlo simulations, each of which include 116 stars on randomly-distributed orbits. The positions of the simulated stars must fall within the field of view covered by the Keck and VLT spectroscopic observations. A nearest neighbor density map is created as mentioned above for each simulation. We show as an example one of the resulting density maps in Figure 3.8. There is a clear deficit of edge-on orbits ($i = 90°$), which artificially enhances the densities at other inclinations and leads to higher peak densities than expected for randomly-distributed orbits. This bias away from edge-on orbits is due to the uniform acceleration prior, which results in smaller line-of-sight distances on average than the simulated stars' true distances. Small $|z|$ will favor face-on orbits over edge-on orbits, which leads to the deficit seen in Figure 3.8. For each simulated map, we determine the peak density as well as the average and standard deviation of the background density, which is calculated using a sigma-clipping technique. We then determine the height of the peak density relative to the background within each density map and create a histogram that includes the heights from all 1000 simulations (Figure 3.9). We compare the observed peak density height to this distribution in order to estimate its significance.

The observed distribution of normal vectors (Figure 3.7) shows an overdensity of 0.024 stars deg^{-2} at (i, Ω) = (130.2°, 96.3°). The height of this peak density over the background is 11.5. A peak height of $\geq$11.5 did not occur in the 1000

simulations of isotropically-distributed orbits. This gives a probability of being consistent with an isotropically-distributed population of less than 0.1% (Figure 3.9). Assuming a Gaussian distribution, this would be equivalent to a 3.3σ detection, giving us confidence that this is in fact a real structure. The direction of the disk plane differs slightly from that in Lu et al. (2009) due to our use of an improved model for the optical distortion in our images (Yelda et al., 2010) and is in better agreement with Paumard et al. (2006) and Bartko et al. (2009). In addition to the peak from the clockwise disk, low-level structure can be seen in Figure 3.7 extending from the CW disk location to larger values of Ω, although this feature is not significant. We investigate these apparent structures in more detail below.

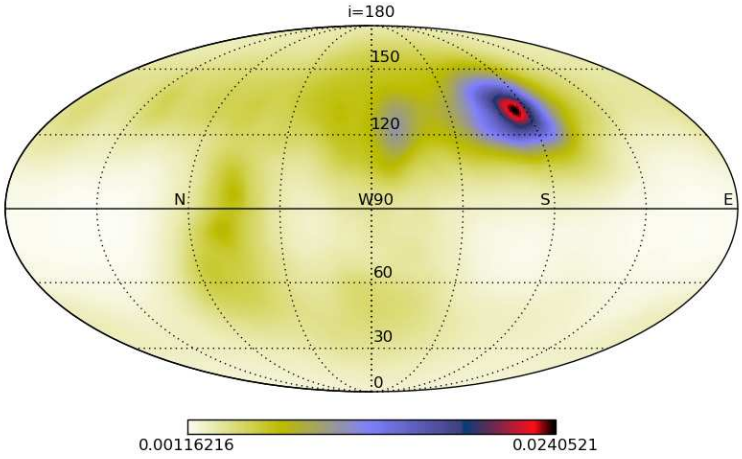

Figure 3.7 Density of normal vectors to the orbital planes of all 116 stars in the sample shown in the HEALpix framework (Górski et al., 2005). The direction of the normal vector is described by the inclination (horizontal lines) and the angle to the ascending node (longitudinal lines). An overdensity of 0.024 stars deg^{-2} at $(i, \Omega) = (130°, 96°)$.

While the existence of the clockwise disk has been well-established prior to

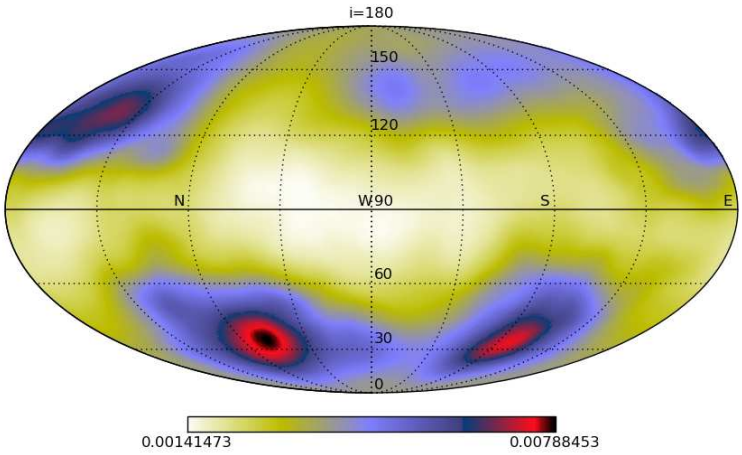

Figure 3.8 Similar to Figure 3.7, but for 116 MC-generated stars with randomly-distributed orbital planes. Note the bias away from edge-on orbits ($i = 90°$) as well as several apparent structures, including what may be interpreted as a counterclockwise disk or streamer.

this work, it is important to identify which stars are likely disk members in order to properly characterize the disk properties. Using Equations 10 and 11 of Lu et al. (2009), which compares each star's PDF(i, Ω) to that of the disk, we determine the likelihood ($LH_{non-disk}$) that a star is *not* part of the clockwise disk at the 3σ significance level ($LH_{non-disk} > 0.9973$). The remaining stars are therefore candidate disk members. This results in 58 candidates, which are identified with red proper motion vectors in Figure 3.10. The opening angle of the disk, taken as the half-width at half-maximum (HWHM) of the peak density of normal vectors, is 15.2°, consistent with previous estimates (Paumard et al., 2006; Lu et al., 2009; Bartko et al., 2009). The uncertainty in the orientation of the disk plane is estimated as the HWHM divided by $\sqrt{N_{members}}$, which gives an uncertainty of 2°.

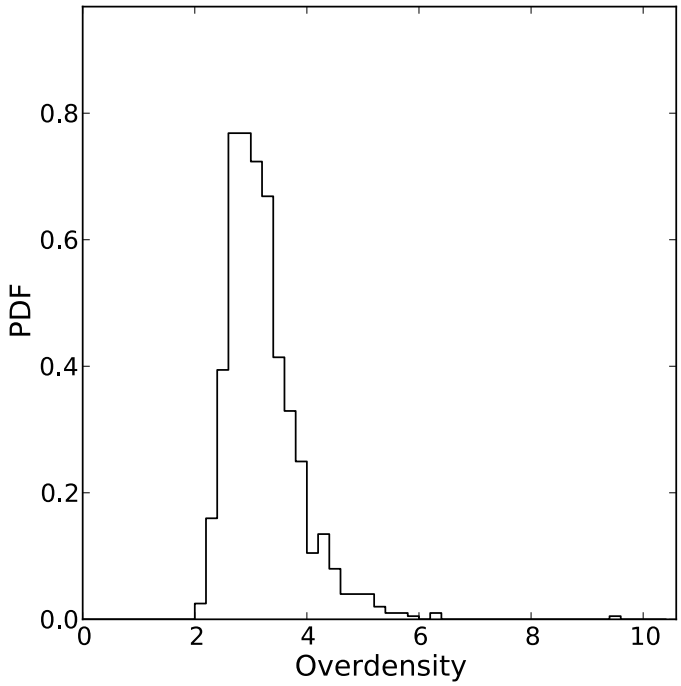

Figure 3.9 Distribution of peak density heights of normal vectors relative to background from 1000 simulations of 116 isotropically-distributed stars.

3.5.3 Eccentricity Distribution of the Clockwise Disk Stars

The orbits for those stars with detected accelerations, which are the best determined since the full 3D positions and 3D velocities are known, are found to be eccentric. All six stars are candidate disk members, which is not surprising since accelerations are more likely to be detected at small radii, where the disk is most prominent. Figure 3.11 shows the combined eccentricity distribution for all candidate disk members, where we separately plot the accelerating stars (N=6) from the stars without acceleration detections (N=52). Orbital solutions that fall within 15.2° of the disk solution are included, thus weighting the distribution by disk membership probabilities. Both eccentricity distributions are clearly offset from $e = 0$, with an average for the accelerating stars of $< e > = 0.27$

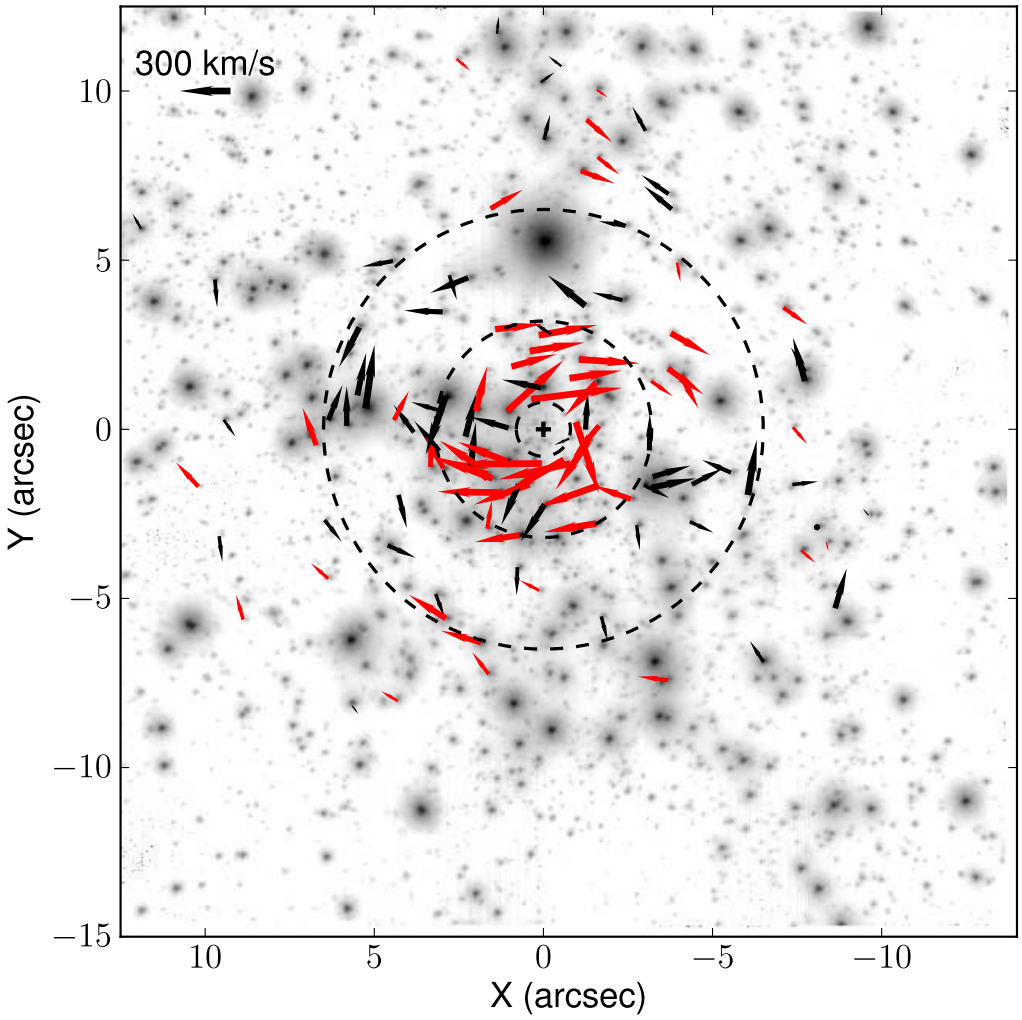

Figure 3.10 Velocity vectors of all 116 stars in the sample. Red arrows indicate the candidate disk members. All remaining stars are shown with *black* arrows. Sgr A* is marked as a cross in the center. The dashed circles mark the three radial bins discussed in §3.5.4 and are located at $R = 0\farcs8$, $3\farcs2$, and $6\farcs5$.

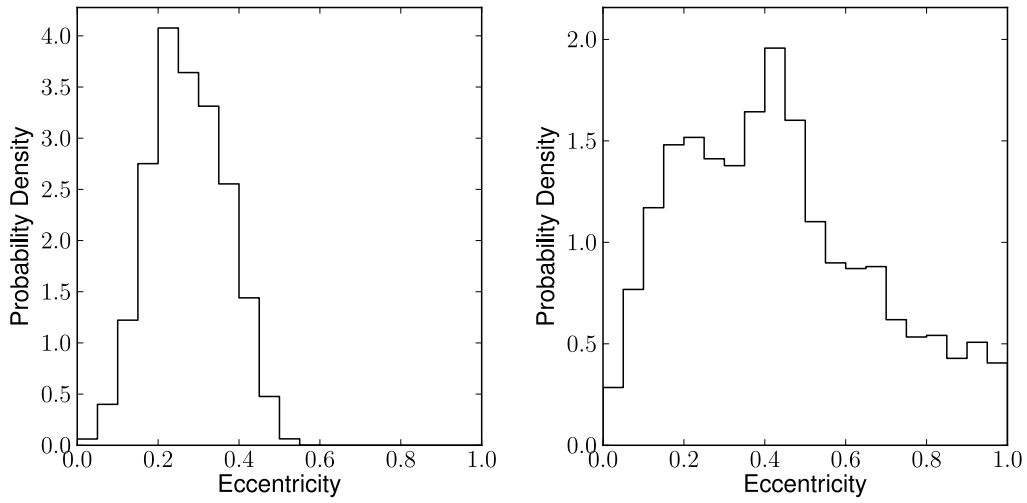

Figure 3.11 Eccentricity distributions for candidate disk members with acceleration detections (*left*) and the remaining candidate disk members (*right*). All orbital solutions falling within 15° of the disk are included, thereby weighting the distributions by disk membership.

$\pm$ 0.09 and the non-accelerating stars $< e > = 0.43 \pm 0.24$. The uncertainty on the eccentricity reported here is the standard deviation of the distribution ($\sigma_{e,measured}$). However, it is critical to account for the impact of measurement error since the eccentricity is a positive definite quantity. We therefore estimate the bias, $\sigma_{e,bias}$, from measurement error on the eccentricity distribution using simulations in §3.6.1, and we report our final values in §3.7.1.

3.5.4 Radial Structure of the Disk

The global structure of the disk can be described by studying its orientation as a function of radius. To this end, we group stars into three radial bins, selecting radial intervals such that roughly equal numbers of stars (∼40) fall in each bin, similarly to the method of Bartko et al. (2009). The radial intervals used are 0.″8 - 3.″2, 3.″2 - 6.″5, and 6.″5 - 13.″3. The density of normal vectors within each

radial bin is mapped using the same nearest neighbor technique described in the above section. Figure 3.12 shows the resulting PDF(i, Ω) for each bin. As in §3.5.2, to quantify the true significance of any peaks, we run MC simulations of isotropically-distributed stars. However, in this set of simulations, we use 40 stars within the radial bin of interest and again constrain their positions to within the field of view covered by the spectroscopic observations.

In the inner radial bin ($N = 39$), the clockwise disk is detected with a height over the background of $\sim$15. Such a peak density height did not occur in any of the 1000 isotropic simulations run (the highest peak density height reached for the inner radial bin was 9.5). Assuming a Gaussian distribution, this would be equivalent to 3.3σ, and we therefore consider this a real detection. The peak density of normal vectors (0.014 stars deg^{-2}) is found at (i, Ω) = (128.7°, 97.7°), consistent with the angles found when using the entire sample. The HWHM is 13.8°, slightly smaller than that found using the entire sample, which is a result of not including stars at larger radii that tend to have larger uncertainties. No other significant structure is detected in the inner interval.

The middle radial bin ($N = 38$) shows a peak density of 0.0025 stars/deg^2 at (i, Ω) = (127.2°, 103.4°), again consistent with the previously determined angle of the clockwise disk, but with nearly an order of magnitude decrease in density. The height of this structure relative to the background is 3.7, which occured in 32 out of 100 isotropic simulations (32%). Thus, this feature is not significant. While the structure extending from the clockwise disk location towards higher i and Ω is also not significant, it appears consistent with the direction of the proposed "warp" by Bartko et al. (2009). This excess feature is explored in more detail in section 3.6.3. We do not detect the previously proposed counterclockwise disk, nor any other significant features in the middle radial bin.

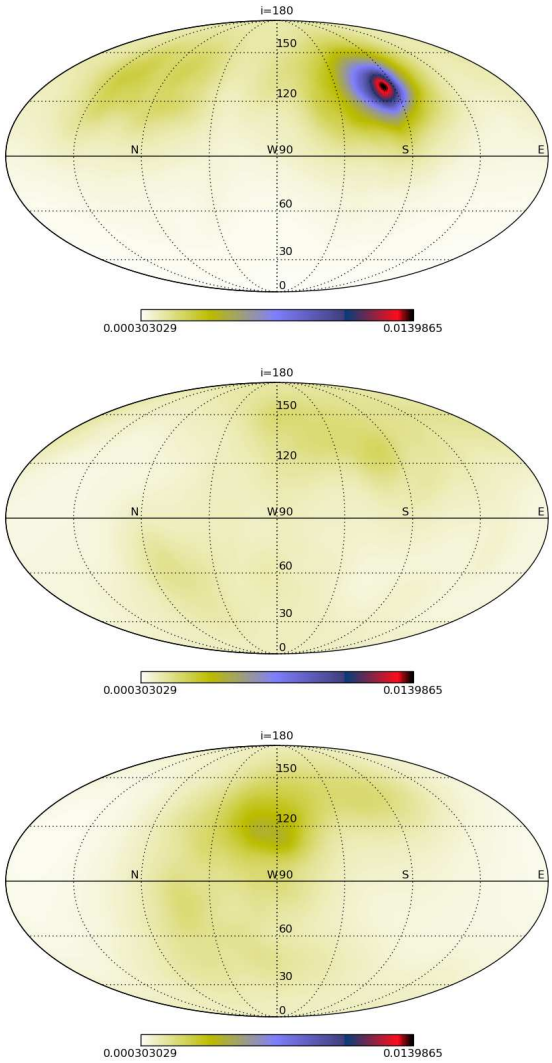

Figure 3.12 Density of normal vectors for stars in the three separate radial bins: 0.″8-3.″2 (*top*), 3.″2-6.″5 (*middle*), and 6.″5-13.″3 (*bottom*). The clockwise disk feature at $(i, \Omega) = (130°, 96°)$ is prominent in the inner and middle radial bins, but shows a decrease in density with radius. The degenerate orbital solutions associated with the CW disk stars are seen as the slight density enhancement near $(i, \Omega) \sim (130°, 300°)$ in the top panel. The middle radial interval shows hints of the CW disk and an elongated structure extending from this location. In the outermost radial bin, a slight density enhancement is seen at $(i, \Omega) = (117°, 192°)$, but is not found to be significant. The only significant structure seen is the clockwise disk at the innnermost radii. The same scaling is used in each plot to show the relative strength of the features.

Finally, the outermost bin ($N = 39$) shows faint hints of the main clockwise disk (bottom panel of Figure 3.12) and a slight overdensity near (117.3°, 192.0°), consistent with the feature seen by Bartko et al. (2009). The peak density in this location has a height of ∼5 relative to the background. In our isotropic simulations, a peak density height of >5 occurs at a rate of 4%. We therefore conclude that this minor density enhancement does not differ from a population of stars on randomly-distributed orbits.

3.6 Modeling the Disk

Here we present a series of simulations in which we model the observations of a stellar disk in order to explore the impact of measurement error and our acceleration prior assumptions on the observed properties of the disk. In particular, we focus on the eccentricity distribution, the fraction of disk members, and the orientation of the plane as a function of radius.

In each set of simulations performed, we create mock kinematic data (x, y, v_x, v_y, v_z, a_x, a_y), add errors to each of these variables, and run our MC orbital simulations similarly to the way the observed data are treated (§3.4). These mock data are generated by assuming a true orbit (inclination i, angle to the ascending node Ω, time of periapase passage T_0, longitude of periapse ω, period P, and eccentricity e) around a point mass of 4.6×10^6 $M_\odot$. For all stars in all simulations, we uniformly sample T_0 from 1995 (the beginning of our observations) to 1995 + P, and ω from 0° to 360°. For isotropic stars, we assume a surface density profile of $n(r) \propto r^{-1.14}$ as found by Do et al. (in prep.) for the young stars beyond $R = 1''$, the eccentricities are sampled from a uniform distribution between 0 and 1, and i and Ω are sampled uniformly over the range of allowed angles. When simulating disk stars, the semi-major axes are randomly

sampled such that the resulting surface density profile in the disk plane follows the observed profile, $n(r) \propto r^{-1.9}$ (Paumard et al., 2006; Lu et al., 2009; Bartko et al., 2009), which when combined with the black hole mass gives the period of the orbit. The orientation of the disk plane is set to that of the observed disk, $(i,\ \Omega) = (130.2°,\ 96.3°)$. The distribution of stellar eccentricities for disk stars is varied and depends on the simulation. From these simulated orbits, we select the 3D positions, velocities, and accelerations at a particular "observation" time, which we take as 2004.2, the mean time of our actual observations. Mock accelerations are only determined for stars within $5''$, consistent with our treatment of the real data. We consider only those simulated stars whose projected positions are within the field of view covered by the spectroscopic observations.

The noise added to the mock data is based on the observed measurement uncertainty as a function of distance from the black hole, as astrometric uncertainties tend to increase with radius. The observed uncertainties as a function of projected radius are shown in Figure 3.13. We determine the minimum and maximum uncertainties in position, velocity, and acceleration of the known young stars in our sample in $1''$ radial intervals. In each trial of a simulation, the uncertainties are randomly sampled from a uniform distribution between these boundaries for the appropriate radial interval (dependent on the simulated star's projected radius). We then run 10^4 MC trials in which we sample from the mock data and the assigned uncertainties for each simulated star. This results in a 6-dimensional PDF representing the probability distributions for the six orbital elements. For simplicity, we only use acceleration information if the star's simulated acceleration is significant (5σ), given its assigned uncertainty. For the remaining stars, a uniform acceleration prior is used, imposing the same boundaries of the minimum acceleration allowed given a bound orbit and the maximum acceleration given the star's projected radius (§3.4.2).

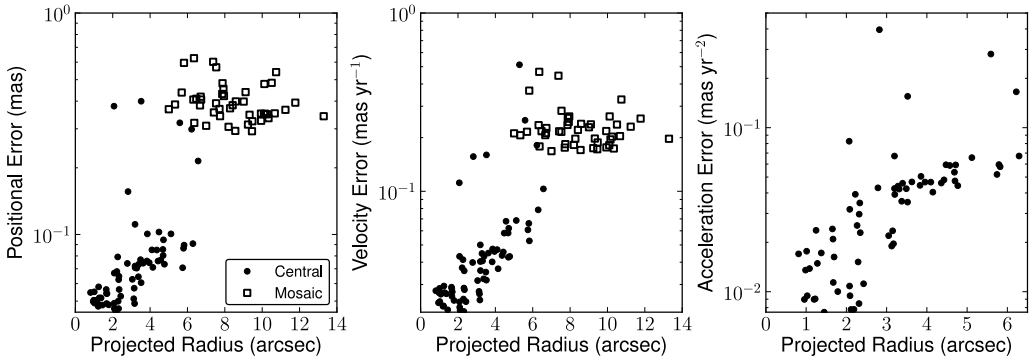

Figure 3.13 Observed position (*left*), proper motion (*middle*), and acceleration (*right*) uncertainties as a function of projected radius. The average uncertainty along the X and Y coordinate are plotted. The filled circles mark the stars in our narrow-field data set and unfilled squares indicate the stars in the wide-field mosaic data, which have projected radii $R > 5''$. We note that in contrast to our treatment of the data in §3.3.2.3, all young stars in the narrow field data sets were fit for accelerations for the purpose of determining uncertainties for the mock data created in the simulations of §3.6. Astrometric uncertainties applied to the mock data are pulled from a uniform distribution ranging from the minimum and maximum observed uncertainties within $1''$ intervals.

3.6.1 Eccentricity Bias

The eccentricities estimated in our orbital analysis may be systematically biased upward as a result of measurement error. Here we test whether or not measurement error can make a truly circular disk appear to be eccentric. To quantify the amount of bias, we create mock data for two disk models, each consisting of 100 stars orbiting the SMBH with orbital parameters as described above and an eccentricity of $e = 0.0$ and $e = 0.3$. Figure 3.14 shows the mock data and the resulting eccentricities from the MC simulations, which are shown separately for stars with significant and non-significant accelerations. The distributions include all solutions with orbital planes within 15° from the input disk plane. The peak of the eccentricity distribution of the circular disk model is measured at $e = 0.0$ - 0.05 for the accelerating stars, and at $e = 0.1$ - 0.15 for the stars without accel-

erations. This rules out the possibility that the observed eccentricities in Figure 3.11 are circular, especially for the best determined orbits (i.e., orbits of the accelerating stars). In the simulation of eccentric disk stars, the distribution for the non-accelerating stars is broader and slightly shifted upward as compared to that of the accelerating stars, a result of the increased measurement uncertainty. The average eccentricity for the simulated accelerating and non-accelerating stars is 0.31 ± 0.06 and 0.42 ± 0.21, respectively. Thus, while the eccentricity bias is negligible for the stars with the best determined orbits, the impact of the measurement error on the remaining stars is seen as both a shift in the expectation value (of $\sim$0.12) and a broadening in the distribution (of $\sigma_{e,bias} = 0.21$) of the eccentricities.

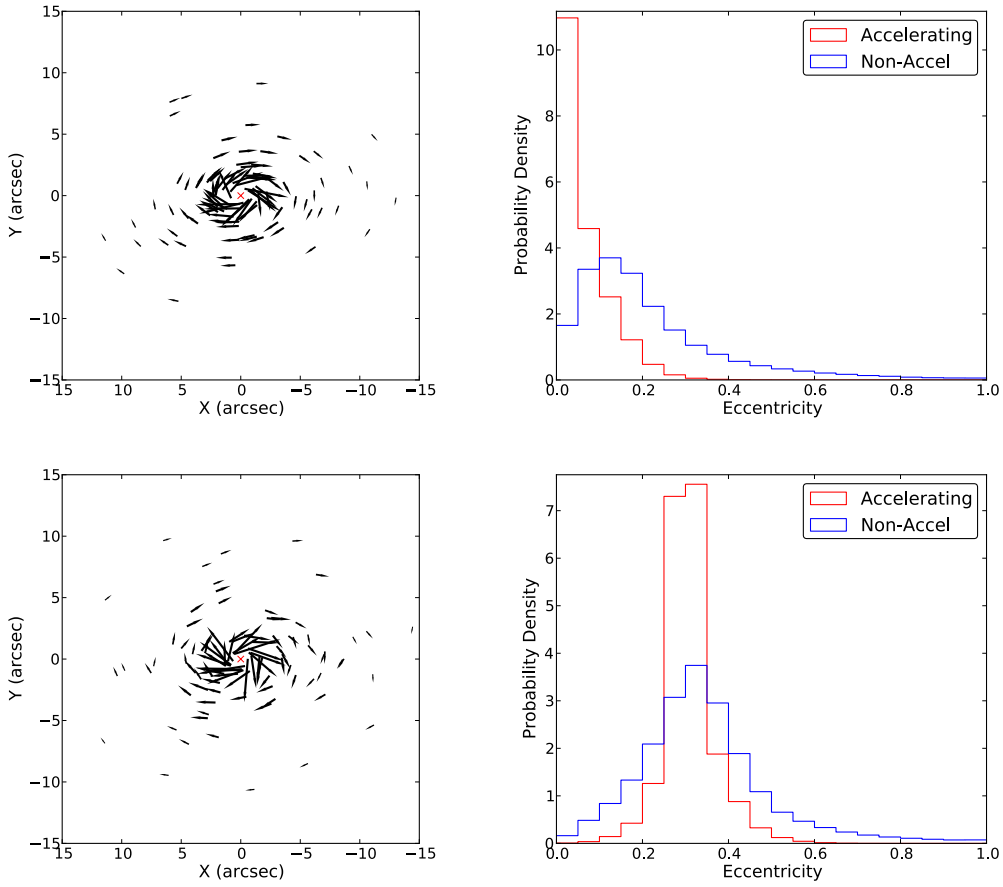

Figure 3.14 Simulated circular (*top*) and eccentric (e=0.3; *bottom*) disks each consisting of 100 stars and with an orbital plane orientation similar to that of the observed disk. (*Left*) Mock data showing the velocity vectors of the disk stars. The location of the black hole is marked as a red x at the center. (*Right*) The eccentricity distributions of the accelerating (*red*) and non-accelerating (*blue*) stars from each simulation. The orbits of the accelerating stars are more accurately determined, as expected. Based on these simulations, the observed eccentricity distribution in Figure 3.11 cannot be a result of measurement bias added to an intrinsically circular disk.

We can also determine the best-fit distribution of eccentricities explicitly by comparing simulated distributions to the observed. We start with mock data for a disk that is formed with some eccentricity, e_0, and with other orbital parameters as described above. A perturbation is introduced as a random velocity kick added to each star's mock data velocities (in each of the three dimensions). The magnitude of the velocity kick is taken as a fraction of the local orbital velocity, f_v, assuming circular orbits and a black hole mass of 4.6×10^6 $M_\odot$.

A grid of models is generated in which we vary both e_0 and f_v. The initial eccentricities and local orbital velocity fraction that are modelled are e_0 = [0.0, 0.1, 0.2, 0.25, 0.27, 0.3, 0.32, 0.35, 0.4, 0.45, 0.5, 0.55, 0.6, 0.65], and f_v = [0.07, 0.08, 0.09, 0.1], respectively, giving a total of 56 separate models. An example of the generated mock data and the corresponding distributions of eccentricity, inclination, and angle to the ascending node for the 100 simulated disk stars are shown in Figure 3.15. These distributions represent the initial spread in the orbital parameters of the disk stars prior to running the MC simulation.

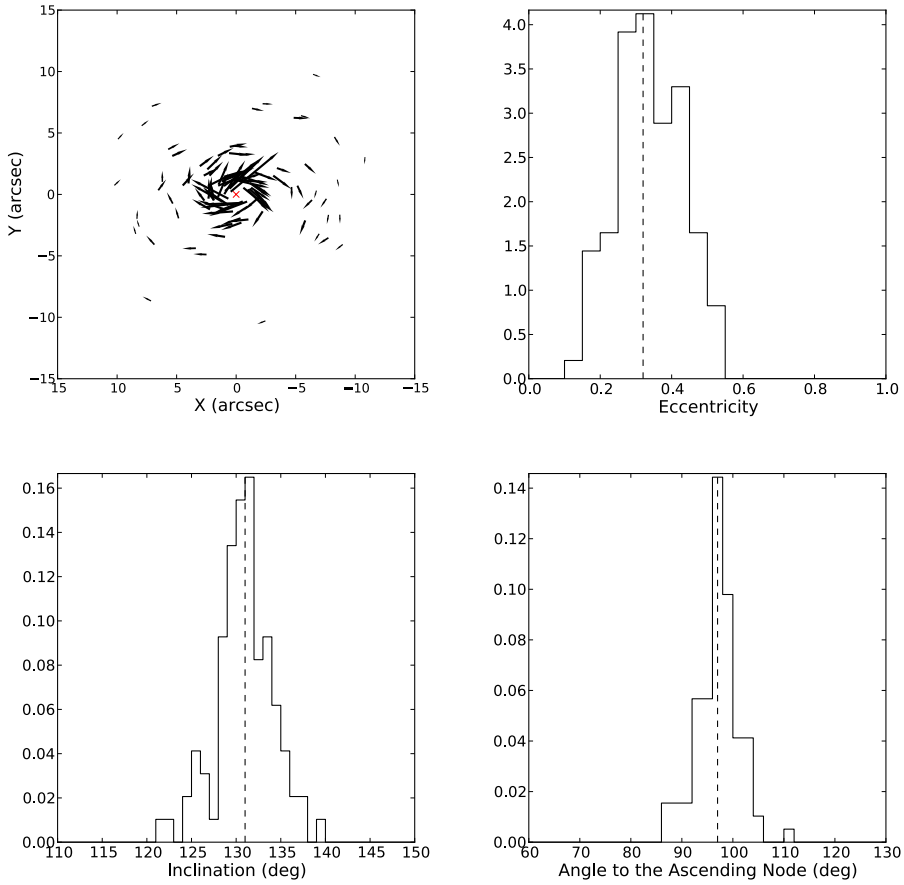

Figure 3.15 (*Upper left*) Example mock velocities for a disk with initial eccentricity ($e_0 = 0.32$) and velocity kick of 7% of the local orbital velocity ($f_v = 0.07$). The eccentricities (*upper right*), inclinations (*lower left*), and angles to the ascending node (*lower right*) for the 100 simulated stars after applying the velocity kick. The dashed line indicates the initial orbital parameters of the stars, before the velocity kick was applied.

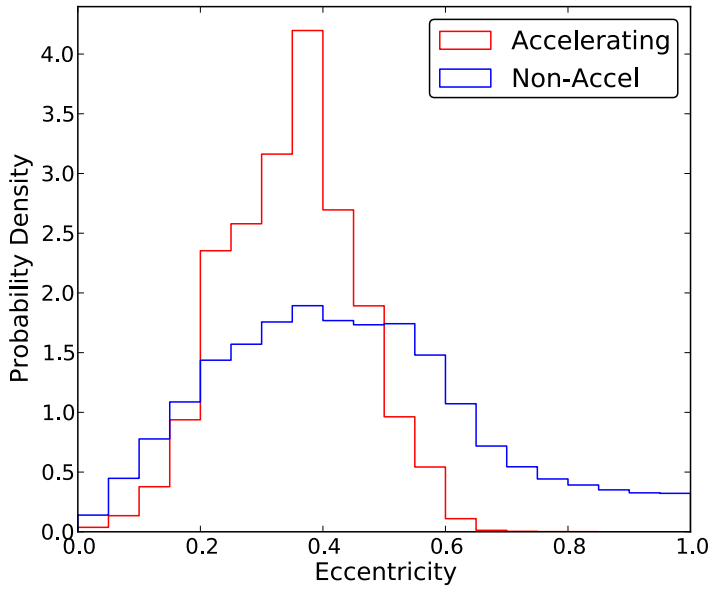

Figure 3.16 The resulting eccentricity distributions for accelerating (*red*) and non-accelerating (*blue*) stars from one of the disk models ($e_0 = 0.32$, $f_v = 0.07$).

From the simulated orbits, mock kinematic data are generated, noise is added to each variable, and the MC simulation is performed. Figure 3.16 shows the resulting eccentricity distribution from one of the disk models ($e_0 = 0.32$, $f_v = 0.07$). We plot the eccentricity distribution separately for the accelerating and non-accelerating stars to demonstrate the power of acceleration measurements in determining the disk stars' true eccentricity. For the accelerating stars, the eccentricity distribution is nearly centered on the input value, with broadening due to the velocity perturbation and eccentricity bias from measurement error. Again, we see both a shift and broadening in the distribution of the non-accelerating stars. Similar distributions are created for all 56 disk models and are compared to that of the observed data.

From the above simulations, we find the best fit eccentricity distribution by minimizing χ^2 between the model and the observations. This is done separately

for the accelerating and non-accelerating stars. In computing χ^2, we assume all errors are unity. Figure 3.17 shows the χ^2 values as a function of initial eccentricity (e_0) and the size of the velocity perturbation applied (f_v). A clear minimum is seen near $e_0 \sim 0.27$ when considering either accelerating or non-accelerating sources. However, there is no discernible difference between the various velocity perturbations used. Regardless, these simulations strengthen the case for non-circular orbits of the candidate disk members and show a likely eccentricity of $e \sim 0.3$.

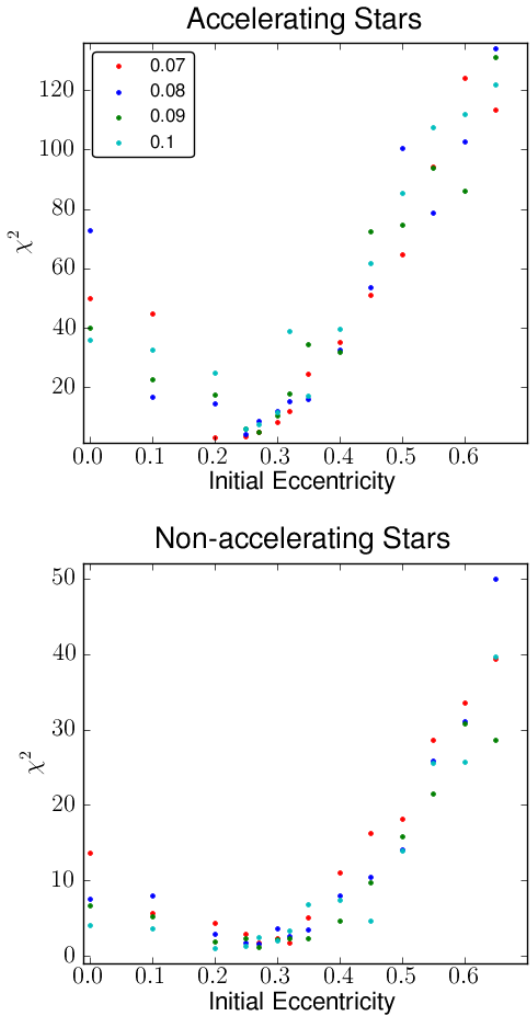

Figure 3.17 χ^2 values as a function of the initial eccentricity (e_0) and the size of the velocity kick applied to the mock data, given as a fraction (f_v) of the local orbital velocity of the star. The χ^2 value was computed by comparing the normalized eccentricity distribution of the simulated disk stars to that of the observed candidate disk stars. The results are shown separately for accelerating stars (*top*) and non-accelerating stars (*bottom*). We find that χ^2 is minimized for a disk with $e_0 = 0.27$ when considering either accelerating or non-accelerating stars, which is encouraging given that the orbits of stars without accelerations are less-constrained. We do not see a difference in the velocity perturbations tested here.

3.6.2 Fraction of Stars in the Disk

Understanding the relative numbers of stars on and off the disk may have implications for both star formation and dynamical evolution scenarios. Here we attempt to quantify the true fraction of disk stars by determining the level of contamination introduced by our disk membership analysis. We create mock data sets that consist of both disk stars and stars with isotropically-distributed orbital planes, and vary the fraction of stars on the disk, f_{disk}. Eleven mock data sets each consisting of 120 stars are generated, with fractions f_{disk} = 5 - 55%, spaced every 5%. For the disk stars, these data are generated for orbits with $i = 130.2°$, $\Omega = 96.3°$, and $e = 0.32$, and a velocity perturbation equivalent to 7% of the local orbital velocity is applied. After applying the velocity kick and recalculating the orbits, the average and standard deviations of the disk parameters are $< e > = 0.32 \pm 0.09$, $< i > = 130.2° \pm 3.0°$, and $< \Omega > = 96.6° \pm 3.9°$, which are similar to the observed distributions.

After running the MC simulations on these mock data, the resulting orbital solutions are examined, and the density of normal vectors, PDF(i, Ω), is computed using the same nearest neighbor analysis (N=6) used on the real data (§3.5.2). Figure 3.18 shows the disk properties obtained for each model, including the peak density of normal vectors and its location, given by inclination and angle to the ascending node, as well as the opening angle of the disk, given by the HWHM. The errors on i and Ω are taken as the HWHM divided by $\sqrt{N_{disk}}$, where N_{disk} is the true number of disk members, which depends on the fraction, f_{disk}, used in a given model. A disk is detected at the input values of i and Ω, within the uncertainties, in all simulations. The peak density of normal vectors, however, is most consistent with the observed density of 0.024 stars deg^{-2} in the $f_{disk} = 20\%$ case. As the relative number of disk to isotropic stars increases, the

observed density is overestimated by up to a factor of $\sim$4. The disk opening angle for the f_{disk}=20% model is 13°, only slightly smaller than the observed value of 15°.

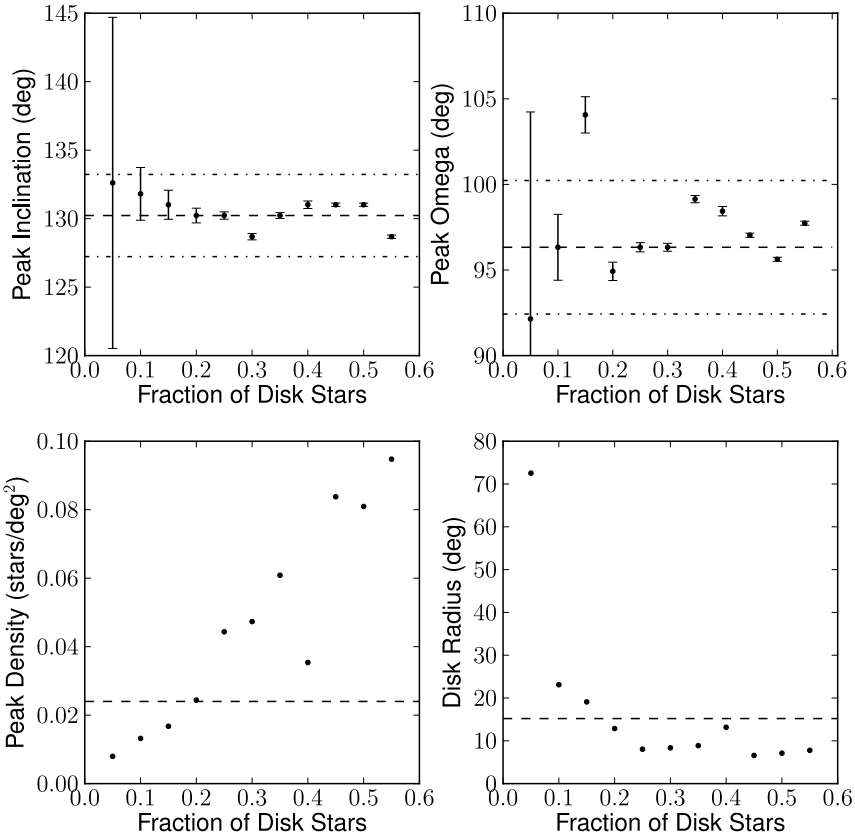

Figure 3.18 Resulting disk properties from the disk fraction simulations in §3.6.2. The peak inclination (*top left*), angle to the ascending node (*top right*), peak density (*bottom left*), and disk opening angle (*bottom right*) are shown as a function of the disk fraction modelled. The 1σ ranges of the initial input angles of the disk are shown as dashed-dotted lines in the top panels for comparison. The observed disk's peak density (0.024 stars deg^{-2}) and opening angle (15.2°) are shown in the bottom panels as dashed lines.

These simulations can be used to test our ability to identify disk stars with the method presented in Lu et al. (2009) and repeated here in §3.5.2. To estimate the level of contamination in each simulation, we rule out stars as disk members using three different significance criteria: $LH_{non-disk} > 0.9973$ (3σ, as used for the real data and described in §3.5.2), $LH_{non-disk} > 0.9545$ (2σ), and $LH_{non-disk} > 0.6827$ (1σ). The remaining stars are considered disk candidates. Figure 3.19 shows the ratio of the estimated number of candidates to the true number of disk members for each model, which reveals the degree of contamination from the non-members. We find that the number of true disk members is overestimated in all models using the 3σ cut. On the other hand, when excluding stars from disk membership at the 1σ level, and therefore considering only the most probable candidates, the level of contamination is minimal or non-existent for all models in which the disk fraction was greater than 20%. We note that a small number of true disk members are missed with this high probability threshold. There is a factor of two overestimation of disk members for the $f_{disk} = 20\%$ model, which is the model that is most consistent with the observations based on the peak density of normal vectors. We therefore conclude that the level of contamination in the observed disk candidates is likely to be $\sim$50%.

3.6.3 Stars on the Line of Nodes

It is not unreasonable to expect some of the stars in the observed disk to have a line-of-sight distance of zero, in which case they are located along the disk's line of nodes. For such stars, how are their orbital solutions affected by our acceleration prior? Unless the star has a detectable acceleration or an upper limit constraining the line-of-sight distance to $|z| > 0$, the line-of-sight distance is determined by randomly sampling from a uniform distribution of accelerations, bounded by the

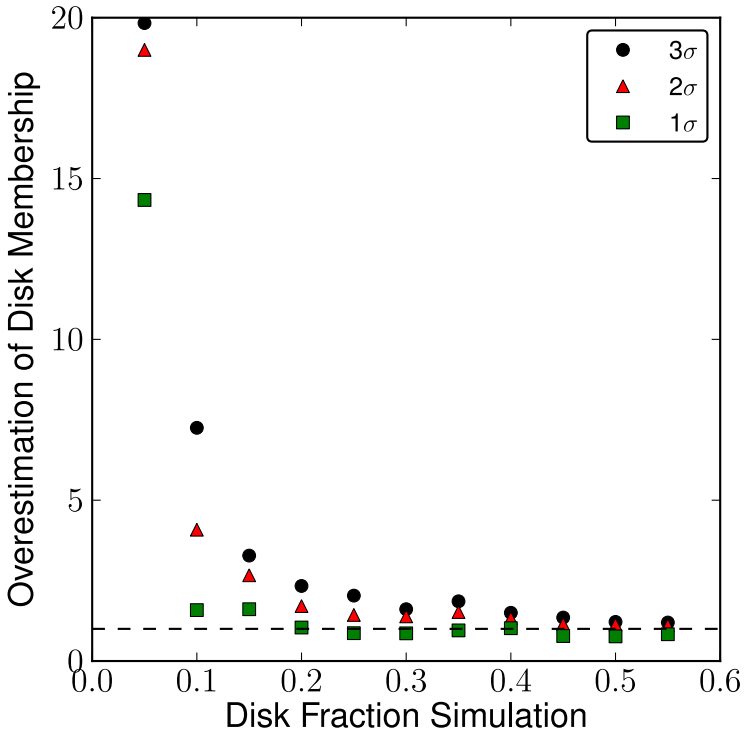

Figure 3.19 The level to which the true number of disk members is overestimated in each disk-fraction model that was run, indicating the level of contamination from non-disk members. Stars with $LH_{non-disk} > 3\sigma$ (*black dots*), 2σ (*red triangles*), and 1σ (*green squares*) are excluded from disk membership, and the remaining stars are considered candidate disk members. Excluding stars at the 3σ level results in significant contamination, while the less stringent cuts give fewer contaminants.

minimum and maximum allowed accelerations. With such a prior, a wide range of z's is allowed, most of which will be non-zero. To investigate the impact of this prior on the orbital solutions, we show in Figures 3.20 and 3.21 the probability distributions of i and Ω for two example mock stars from our simulations in §3.6.2. The mock kinematic data are shown in the top panel, with the star of interest circled. For most stars, the distributions of i and Ω are well-behaved, with nearly Gaussian distributions centered on the input values, and a degenerate set of solutions in Ω due to the sign ambiguity in z (Figure 3.20). The solutions for stars that are situated on or near the line of nodes (Figure 3.21), however, are biased away from the input value. While the distribution of inclinations includes the true value of i, its peak is offset from this value by up to 15° in either direction. The degenerate solutions for Ω are pushed to either side of the true value, by as much as 50° for some stars. This bias can be understood more clearly by plotting Ω as a function of z. As seen in the bottom right panel of Figure 3.21, the true Ω is only recovered for trials in which $z \sim 0$ was sampled. At all other line-of-sight distances $|z| > 0$, Ω is biased away from the true solution. This effect is seen in all simulated disk stars that are located within $\sim 1''$ from the line of nodes in projection, and therefore will appear in the observed distributions of stars that have a line-of-sight distance near zero.

Depending on the fraction of stars located near a nodal point, the biased orbital solutions may affect interpretations of the disk. Figure 3.22 shows the density of normal vectors for a group of 10 simulated stars, all of which have line-of-sight distances of $z \sim 0$. Seven of these stars are disk stars with (i, Ω) = (130.2°, 96.3°) and three stars have randomly-oriented orbits. While the peak density is located at the location of the simulated disk, there is a large spread in both angles, which is a result of disk stars located near a nodal point in their orbit. Excess structure is seen extending from the direction of the disk and can

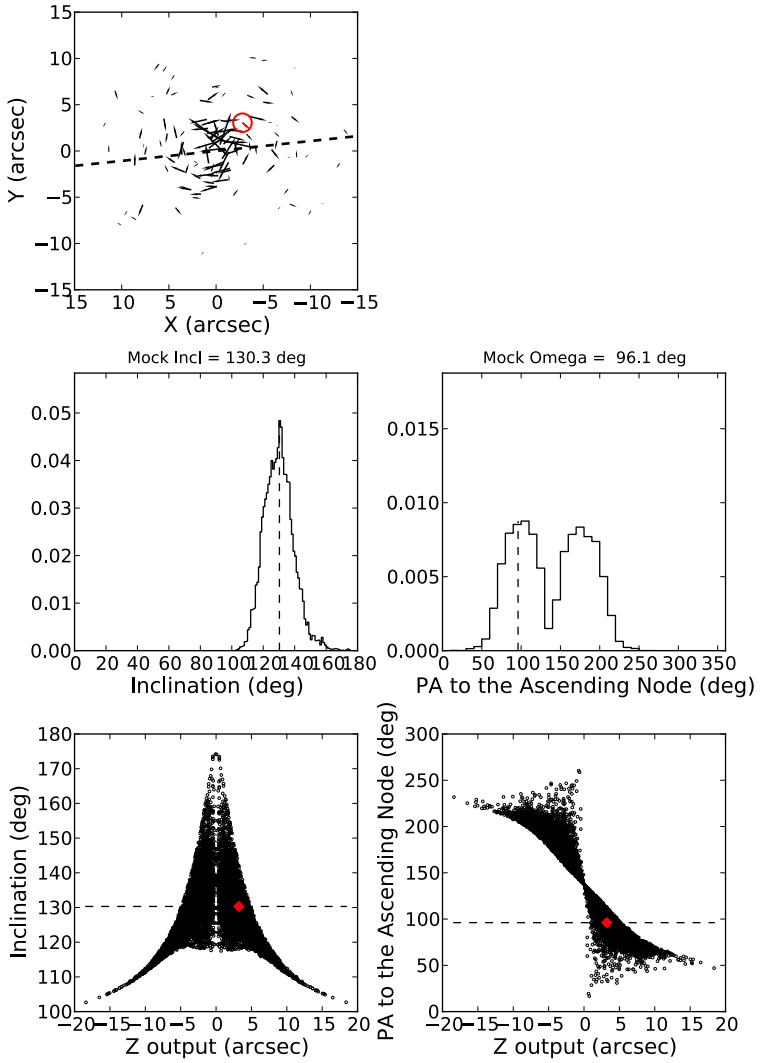

Figure 3.20 Example mock star from the $f_{disk} = 40\%$ simulation. The star, marked with a red circle in the top panel, is a disk star with inclination of 130.3° and angle to the ascending node of 96.1°. The thick dashed line represents the line of nodes. The middle plots show the probability distributions in i (*left*) and Ω (*right*) from the Monte Carlo simulation. The dashed lines indicate the true angles, which are retrieved quite well in the MC simulation. The degenerate set of solutions for Ω is due to the sign ambiguity in the line-of-sight distance, which can be seen in the bottom panels. The true line of sight distance is marked in the bottom panels with a red diamond. These results represent the typical behavior seen for most disk stars.

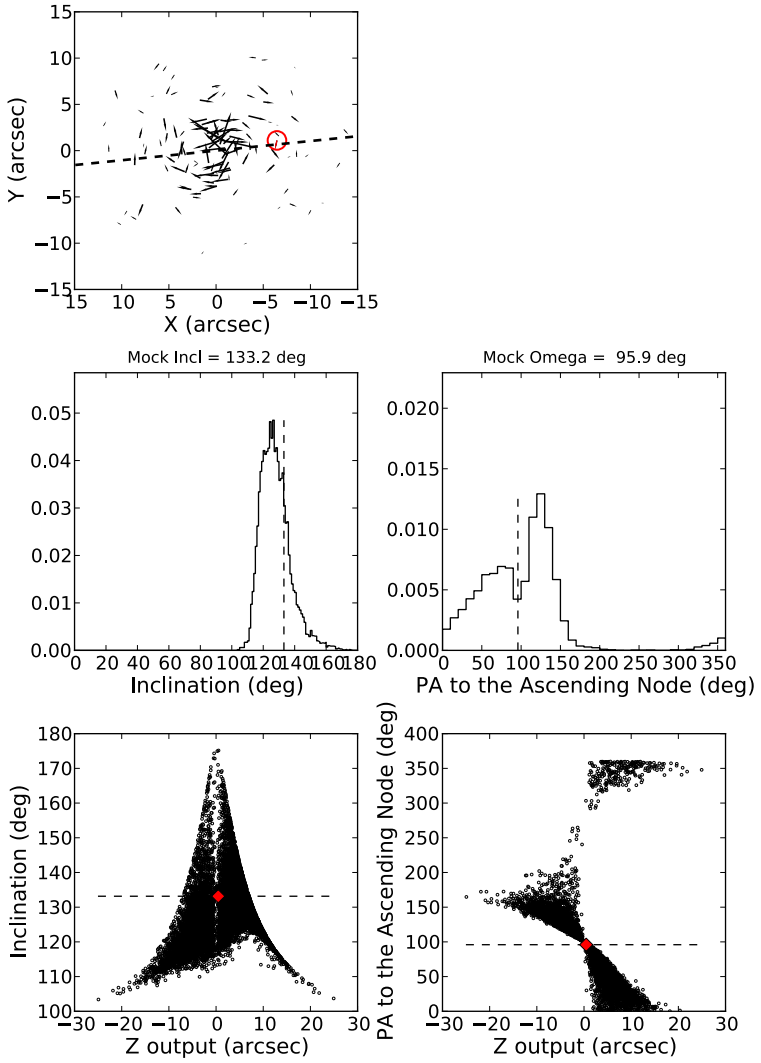

Figure 3.21 Same as Figure 3.20, but for a star located along the line of nodes and therefore with line-of-sight $|z| \sim 0$. The input angles were $i = 133.2°$ and $\Omega = 95.9°$. However, both the inclination and angle to the ascending node from the MC simulations are biased away from the true values. As shown in the bottom panels, Ω is only accurately recovered for $|z| = 0$, while the distribution in i is shifted away from the true value. The red diamonds in the lower panels mark this star's true line of sight distance.

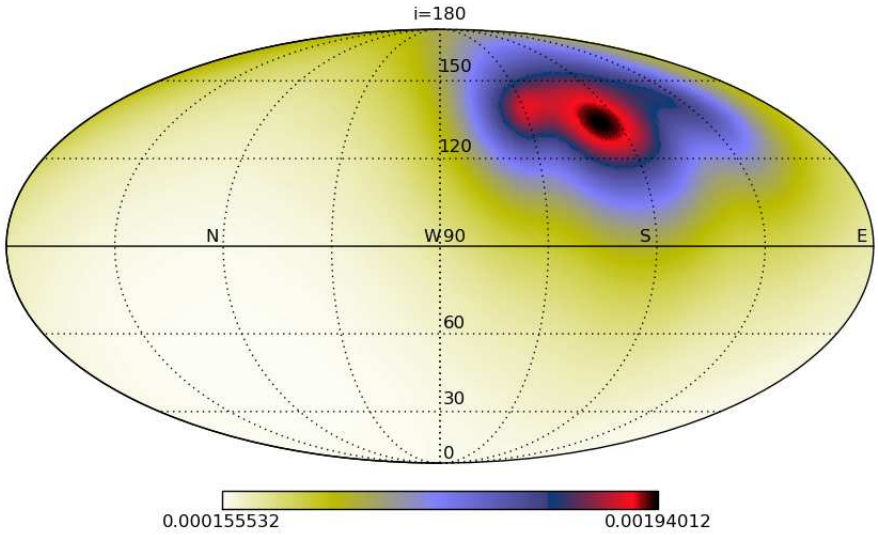

Figure 3.22 Density of normal vectors for 10 simulated stars with line-of-sight distance near zero. Seven of the 10 stars are disk stars and three are part of an isotropic population. While the peak density is located at the location of the simulated disk, $(i, \Omega) = (130.2°, 96.3°)$, there is a large spread in both angles on either side of the disk. The slight density enhancement to the left of the disk location is a result of the line-of-nodes bias described in §3.6.3 and can be mistaken as a real kinematic feature, such as a warped disk.

be mistaken as an additional kinematic feature, such as a warped disk.

In order to properly describe the structure of the disk from our observations, we must identify which, if any, stars suffer from this bias. Figures 3.23 and 3.24 show the PDFs of i and Ω for the young stars within $\sim 1''$ distance from the line of nodes of the clockwise disk ($\Omega = 96.3°$) and that have a projected radius beyond $R = 3\farcs2$. If these stars are members of the disk, they would have small line-of-sight distances as they would be located near either the ascending or descending node of their orbits. While these stars are all on clockwise orbits ($i > 90°$), it is possible that not all are members of the disk. Of the 13 stars plotted, the following nine have qualitatively similar PDFs in i and Ω as the biased, simulated stars: S3-5,

S3-10, S3-190, S4-36, IRS 34W, S4-169, S6-82, S7-161, and S10-32. For many of the stars shown in Figures 3.23 and 3.24, the angle to the ascending node is consistent with that of the disk *only* at $z \sim 0$, and these stars may therefore be disk stars that are affected by this bias. Their inclinations are consistent with the disk at a wider range of z values, but the most probable inclinations are biased away from $i = 130.2°$.

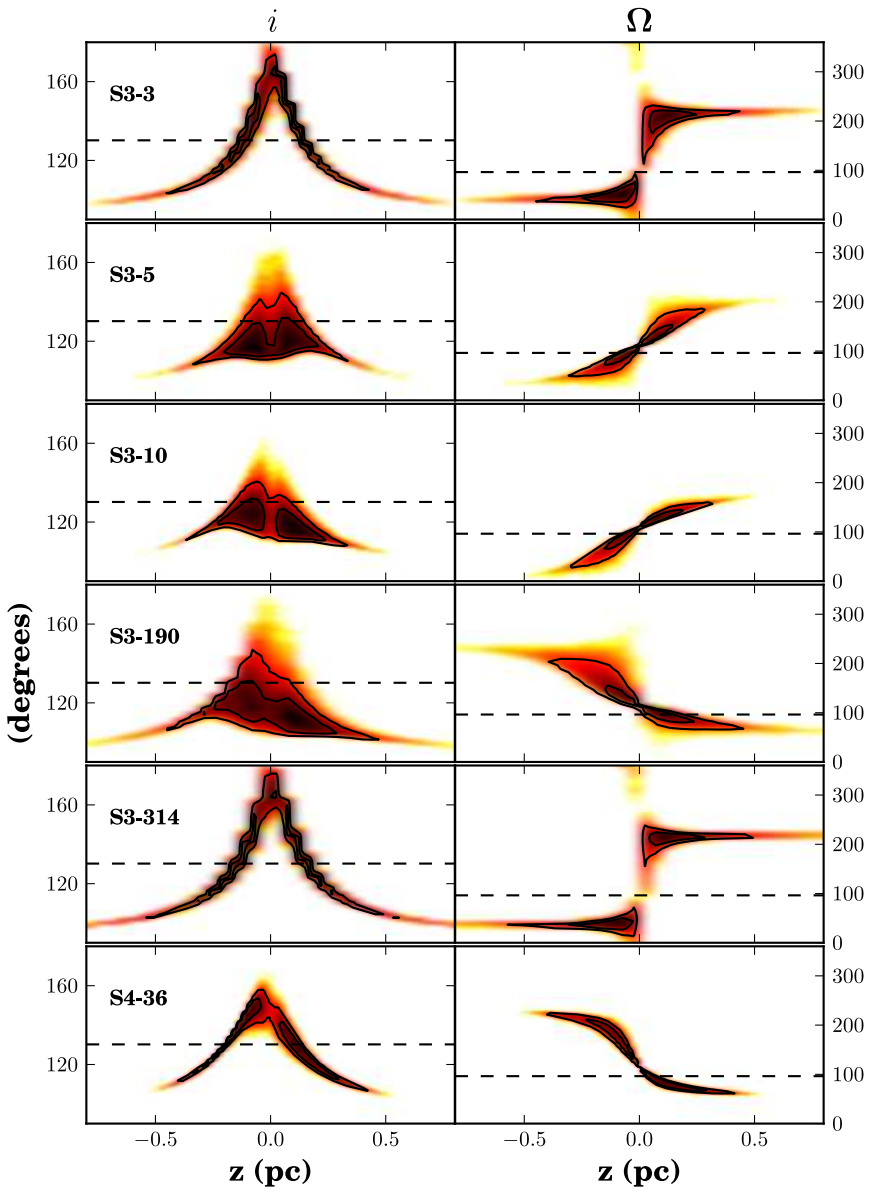

Figure 3.23 Inclinations (*left*) and angles to the ascending node (*right*) as a function of the $|z|$ sampled in the Monte Carlo simulations for the observed stars located within $1''$ of the line of nodes of the clockwise disk ($\Omega = 96.3°$). Stars plotted are S3-3, S3-5, S3-10, S3-190, S3-314, and S4-36, from top to bottom, respectively. Darker regions indicate more probable values, and the 1σ and 2σ contours are overplotted as black lines. The dashed lines denote the orientation of the plane of the disk ($i = 130.2°$, $\Omega = 96.3°$). If these stars are disk members, their line-of-sight distance would be $|z| \sim 0$. The range of z's in the MC simulation, however, is such that most line-of-sight distances sampled are non-zero, leading to a bias in the orbital solutions for these stars.

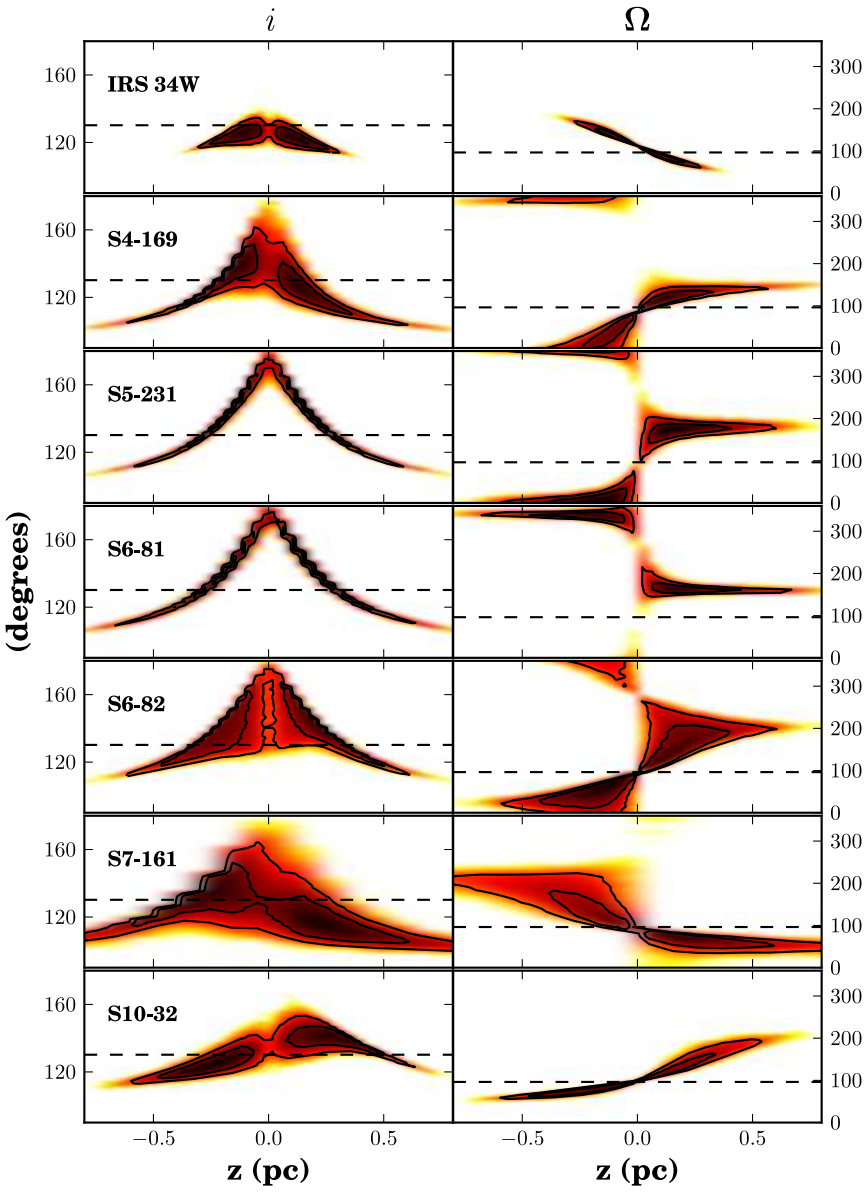

Figure 3.24 Same as Figure 3.23, for IRS 34W, S4-169, S5-231, S6-81, S6-82, S7-161, and S10-32, from top to bottom, respectively.

We investigate how this bias affects the 2D PDF(i, Ω) of the middle radial bin by combining the PDFs of the stars that fall near the line of nodes and at projected radii between R = 3.″2 - 6.″5 (Figure 3.25). These include 10 of the 13 stars plotted in Figures 3.23 and 3.24. A peak density of 1.5 $\times$ 10^{-3} stars deg^{-2} is located at i = 141°, Ω = 113°, which is offset from the location of the main clockwise disk and in the same direction as the excess structure found by Bartko et al. (2009) for the stars in their middle radial bin (see their Figure 11). It is unclear whether the individual stars we have identified here as having biased solutions are the same stars contributing to the excess structure in Bartko et al. (2009), which they have interpreted as a warped disk. However, the excess structure that we see, although not significant, can be explained by the line-of-nodes bias, which is also seen in simulations of a flat disk and is due to a higher frequency of sampling non-zero line-of-sight distances (see Figure 3.22). Our results are therefore consistent with a flat disk. We should also note that if this bias in our analysis did not exist and if these stars were truly disk members, then the density of normal vectors at the location of the main CW disk would be higher than what is seen in the middle panel of Figure 3.12, which would likely increase the significance of the disk at these radii.

3.7 Discussion

We have performed a detailed kinematic analysis on the central parsec young star population using high precision astrometry over a longer time baseline than in any other such study. Combined with radial velocity measurements, we have confirmed the existence of the clockwise stellar disk and shown there is no significant counterclockwise structure, in agreement with Lu et al. (2009). Roughly 50% of the stars in our sample are candidate members of the disk. This is consis-

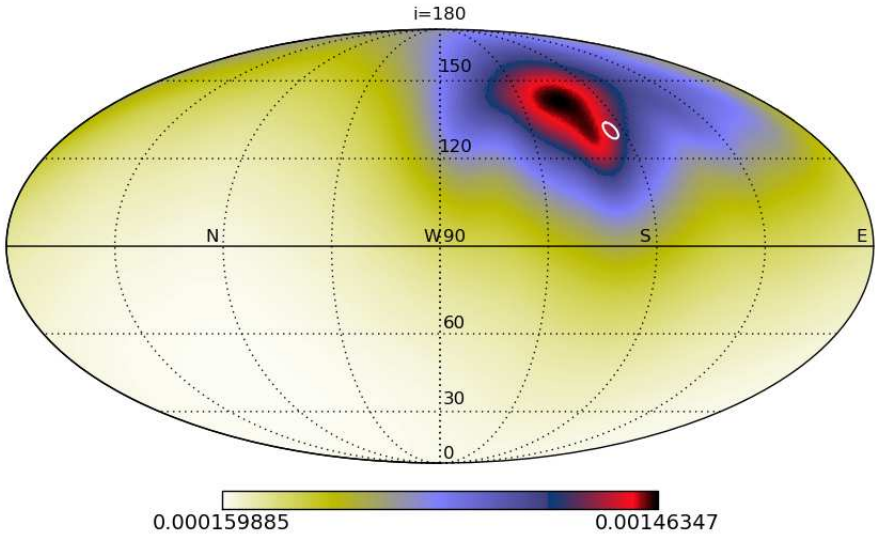

Figure 3.25 Density of normal vectors to the orbital planes for the 10 stars within 1″ in projection from the line of nodes of the clockwise disk and in the middle radial bin ($R = 3\farcs2$-$6\farcs5$). Note that we use a different scaling here as compared to Figure 3.12 in order to show the effect of the bias. The white circle marks the location of the clockwise disk as obtained using the full sample (i, Ω) = (130.2°, 96.3°). These stars contribute to the excess structure extending from the location of the clockwise disk seen in the middle radial bin (middle panel of Figure 3.7). As evident in Figures 3.23 and 3.24, the orbital solutions for many of these sources are biased due to the sampling of non-zero line-of-sight distances. The peak density located at (i, Ω) = (141°, 113°) is not significantly different from the density measured in the opposite direction from the clockwise disk at (i, Ω) = (141°, 81°). Thus, the extension of normal vectors from the clockwise disk is due to biased orbital solutions and not a warp in the disk.

tent with the fraction of disk members found by Lu et al. (2009)[4]. However, our simulations showed that the number of true disk members may be overestimated by up to a factor of two. The candidate disk members are on eccentric orbits, and the orientation of the disk does not change with radius. Here we discuss the implications of these findings.

3.7.1 Eccentricity of Disk Stars

The candidate disk members were found to orbit the SMBH with eccentricities of $e \sim 0.3$. However, as discussed in §3.6.1, one must consider the effects of measurement error on the resulting eccentricity distribution. Our simulations showed that for stars with the best-determined orbits (i.e., those with acceleration measurements), measurement error produces a negligible effect on the expectation value of the eccentricities and adds a dispersion of $\sigma_{e,bias} = 0.06$ to the distribution. For stars without acceleration measurements (i.e., those with larger measurement errors), the expectation value is shifted upwards by roughly 0.12 and the distribution is broadened by $\sigma_{e,bias} = 0.21$. To account for the added spread in the distributions, we subtract the bias term from the standard deviation of the eccentricities in quadrature: $\sigma^2_{e,intrinsic} = \sigma^2_{e,measured} - \sigma^2_{e,bias}$. Our final estimates for the eccentricity distributions for the accelerating and non-accelerating disk sources are $< e > = 0.27 \pm 0.07$ and $< e > = 0.31 \pm 0.12$, respectively. This is the first time the measurement bias has been accounted for in estimates of the eccentricities of stars on the clockwise disk.

The observed eccentricities can be used to constrain formation scenarios for

[4]We note that in Bartko et al. (2009), the properties of the CW disk were described using 30 out of 90 candidate disk stars, which had a minimum angular separation of 10° from the CW disk. However, they quote a fraction of disk membership of 55%, which is inconsistent with the use of 30 out of 90 stars in their analysis of the disk.

the disk. Berukoff & Hansen (2006) showed that the eccentricities of stars deposited into the GC by an infalling cluster will mirror the eccentricity of the cluster's IMBH with a scatter of roughly ± 0.1. While this is consistent with the scatter we find for candidate disk members, the cluster-infall scenario suffers from many theoretical and observational challenges as discussed at the beginning of this chapter.

In the *in situ* formation scenario, an initially circular disk with a normal IMF will reach an rms eccentricity of 0.15 through dynamical relaxation over the population's lifetime (Alexander et al., 2007). Two-body interactions within the disk can excite orbital eccentricities to $e \sim 0.3$ if the disk mass function were top-heavy (Alexander et al., 2007; Haas et al., 2011a), although Löckmann et al. (2009) argue that a canonical IMF would suffice if the stellar cusp is taken into account. However, recent work by Lu et al. (in prep.) shows that the young star population (both on- and off-disk stars) has an initial mass function with a slope of $\Gamma \sim 1.7$ and an age of $\sim$3.7 Myr. Figure 3.26 shows the expected rms eccentricity after dynamical evolution over the lifetime of the population for various mass functions (Alexander et al., private communication). This is a version of Figure 4 of Alexander et al. (2007), where here we show the final eccentricities expected for stars with mass 25 $M_\odot$ after 2.78 Myr, 3.65 Myr, and 4.52 Myr, which spans the 1σ range of the Lu et al. estimates for the age of the population. Given the observed eccentricities here, and the latest mass function slope, our results are consistent with formation in a circular gas disk, as proposed by others (Nayakshin & Sunyaev, 2005; Alexander et al., 2007; Löckmann & Baumgardt, 2009; Löckmann et al., 2009). While simulations of the infall of massive clouds have been able to produce stellar disks with eccentricities as high as $e \sim 0.3$ (Yusef-Zadeh & Wardle, 2008; Wardle & Yusef-Zadeh, 2008; Bonnell & Rice, 2008; Mapelli et al., 2008, 2012), a top-heavy mass function will lead

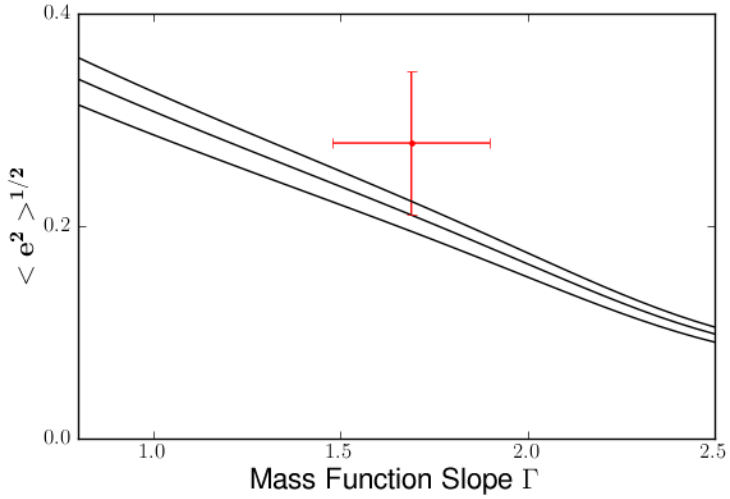

Figure 3.26 Predicted rms eccentricity (*black curves*) of 50 stars, each with mass $M = 25$ $M_\odot$, resulting from 2-body interactions within a stellar disk with various mass function slopes. This is a version of Figure 4 in Alexander et al. (2007), which has been updated to reflect the latest black hole mass estimates (4×10^6 $M_\odot$) and the most recent estimate of the age of the young star population from Lu et al. (in prep.) of 3.65 ± 0.87 Myr. From bottom to top, the three curves represent the rms eccentricity after 2.78 Myr, 3.65 Myr, and 4.52 Myr, respectively. The red point shows the rms eccentricity and estimated uncertainty of our best measured stars ($< e > = 0.28 \pm 0.07$) and the latest estimate of the mass function slope ($\Gamma = 1.69 \pm 0.21$) from Lu et al. (in prep.). The observed values are within 1σ of the predicted values from the Alexander et al. model.

to further excitation of the orbits over the stars' lifetimes. Thus, the present-day eccentricities would be expected to be much higher than what we observe. We note, however, that an additional dynamical mechanism must be invoked to explain the high inclinations of the out-of-disk population.

Finally, the distribution of eccentricities among the candidate disk members was found to have a single peak, lacking the high eccentricity bin ($e > 0.9$) reported by Bartko et al. (2009). We plot only those solutions that are within 15.2° of the disk solution, thereby weighting the distribution by disk membership and minimizing the impact of contamination from non-members. A bimodal

distribution in a stellar disk is difficult to explain, although Madigan et al. (2009) showed that a qualitatively-similar distribution can be produced through coherent torques on the stars' orbits from the underlying stellar cusp. However, the high eccentricity peak ($e = 0.9$ - 1.0) reproduced in the simulations was a result of stars whose inclinations had been excited to such high values that they could no longer be physically associated with the disk (A. M. Madigan, private communication). Furthermore, Bartko et al. (2009) could not rule out that the high-eccentricity peak in their observed distribution was a result of contamination by non-members of the disk.

3.7.2 Flat vs. Warped Disk

In characterizing the structure of the disk, it is critical to properly identify which stars belong to the disk and which stars may be biased by any assumptions made in the analysis. Determining each star's disk membership, however, is not a trivial task and requires an assumption about the disk structure to begin with. We implicitly assumed that the disk has a constant orientation at all radii and we identified the stars that are probably not on the disk to a high statistical significance. The 58 remaining candidate disk members were located at projected radii extending to $r = 11''$ ($\sim$0.44 pc).

To investigate the possibility of a warped disk, we searched for peaks in the normal vector density maps, PDF(i, Ω), in three separate radial bins. The signature of a warped disk would be seen as a continuous change in the location of the density peak as a function of radius. We found that the orientation of the disk's orbital plane does not significantly change from the inner ($0\farcs8$ - $3\farcs2$) to middle ($3\farcs2$ - $6\farcs5$) radial bins. While the *peak* location does not change at these radii, the middle bin does show a feature extending from the location of

the main clockwise disk, consistent with what is seen in Bartko et al. (2009)[5]. We have identified this as a bias in our orbital analysis resulting from the line-of-sight distance prior for those candidate disk stars located near the ascending or descending node of their orbits. The lack of acceleration information and the relatively large velocity uncertainties results in a wide range of sampled line-of-sight distances in our Monte Carlo simulations of the data. Because most of the sampled z's are non-zero, the probability densities are biased away from the disk solution for any star with a true line-of-sight distance near $z = 0$. The bias is most prominent at intermediate radii ($3\farcs2 < r < 6\farcs5$), where it appears that at least nine out of 20 clockwise-moving stars ($i > 90°$) are affected. Interior to this, astrometric uncertainties are much more precise and therefore acceleration constraints on the line-of-sight distance are stronger. This is not only true for the six accelerating stars, but also for the 12 stars with 3σ acceleration upper limits whose line-of-sight distances are constrained to be $|z| > 0$ and are therefore not affected by this bias. Beyond $r = 6\farcs5$, only two out of 23 stars with clockwise orbits are within $1''$ in projection from the disk's line of nodes, and therefore the effect on the PDF(i, Ω) for this radial interval is much less severe.

Could the warp reported by Bartko et al. (2009) be explained by this bias? The line-of-sight distance prior used by these authors assumed a direct translation between the observed projected surface density profile and the three-dimensional density profile. The maximum line-of-sight distance allowed was set by assuming bound orbits, as in our analysis, and of course, the minimum line of sight distance used was $z = 0$. Thus, it is possible that the prior used by Bartko et al. (2009) will

[5]The edges of the three radial bins we use are slightly different than those used by Bartko et al. (2009) since the two studies contain different sample sizes and the radial bins were defined such that they each contained an equal number of stars. In our work, we define the edges of the bins using $R = 0\farcs8$, $3\farcs2$, and $6\farcs5$ and include ∼40 stars per bin, whereas Bartko et al. (2009) use $R = 0\farcs8$, $3\farcs5$, and $7''$ and had ∼30 stars per bin. This fact does not significantly affect the overall results.

also lead to biased orbital solutions for any star that truly is located near a nodal point in its orbit, as the line-of-sight distances sampled will be predominantly non-zero. The feature we see at intermediate radii extending from the main clockwise disk location is consistent with the "excess" structure seen by Bartko et al. (2009). However, it is unclear which stars contribute to their excess feature because the data were not published, and therefore we can only speculate.

Furthermore, the warp in the clockwise disk was reported by these authors to extend to their outer radial bin, where an additional feature in the angular momentum vector density map was seen at $(i, \Omega) = (118^\circ, 179^\circ)$[6]. Bartko et al. (2009) assumed the stars making up this feature were members of the clockwise disk because they computed a locally-averaged angular momentum vector direction and assigned any stars whose orbital planes were within 10° of this average as disk members, thereby assuming a warped disk to begin with. It is the change in the peak location of their angular momentum vectors across the three radial bins that led to the claim of a warped disk. If the orbital solutions of stars at intermediate radii are biased, however, then such a claim may not be valid. While there also appears to be a feature in our density map of stars at large radii (bottom panel of Figure 3.12), it is not a significant overdensity. Thus, we conclude that the clockwise disk is not warped.

The finding that the clockwise disk is flat and that there are no other significant kinematic structures may simplify star formation scenarios in the Galactic center. For instance, Hobbs & Nayakshin (2009) invoked the collision of two giant molecular clouds in order to explain both the proposed warped clockwise disk and the less-coherent counterclockwise (possibly filamentary) structure. While the re-

[6]We note that in Table 3 of Bartko et al. (2009), there is a mistake in the i and Ω angles reported for their outer radial bin. While their reported angles ϕ and θ are consistent with the corresponding plot in their Figure 11, the conversion to i and Ω in Table 3 is incorrect. We report the correct values here.

sulting structures were in qualitative agreement with those reported by Bartko et al. (2009), the masses of stars outside the clockwise disk (and in some of their simulations, within the clockwise disk) were much lower ($\sim$0.1 - 1 $M_{\odot}$) than those observed. Without fine-tuning the initial conditions in such a scenario, it is difficult to explain both a warped clockwise disk and a counterclockwise feature within a single star formation event. Alternatively, one may invoke formation in a single disk followed by subsequent dynamical evolution, as we discuss in the next section.

3.7.3 Off-Disk Stars

The existence of a counterclockwise disk was reported in Paumard et al. (2006), but with updated kinematic measurements, Bartko et al. (2009) find evidence that the disk is less coherent than once thought and may instead be a series of streamers or filaments. While the claim of any CCW structure was refuted by Lu et al. (2009), it was suggested that this was a result of a limited field of view of the *primary* sample ($r < 3\farcs5$), despite the fact that Lu et al. (2009) came to the same conclusion with their *extended* sample using data from Paumard et al. (2006) at larger radii. To address this, we have considerably expanded our field of view using Keck/LGSAO observations and, as shown in §3.5.4, we do not detect any significant structures in the counterclockwise direction. The detection of a single stellar disk provides significant constraints on origin scenarios since only one star formation (or cluster infall) event is required, which is compatible with the observation that all of the stars are approximately the same age (Paumard et al., 2006, Lu et al. in prep.). In fact, if two nearly-orthogonal stellar disks did co-exist, their mutual interactions over 6 Myr would lead to their dissolution, thereby leaving no observable signature (Löckmann & Baumgardt, 2009).

While at least half of the central parsec's young stars do not orbit within the plane of the clockwise disk, the fact that all of the stars appear to have the same age implies that they likely formed together. In the case that all of the young stars formed in a single disk, some dynamical mechanism(s) that can excite the orbits such that they are no longer kinematically associated with the original disk must be invoked. It was shown that 2-body relaxation is not sufficient to explain the high inclinations relative to the clockwise disk (e.g., Cuadra et al., 2008). Yu et al. (2007) suggest that an IMBH or dark star cluster can scatter the outermost stars off of the disk yet leave the innermost disk stars unperturbed. One of the major challenges to this scenario, however, is the lack of evidence for an IMBH at the Galactic center. Alternatively, Šubr et al. (2009) and Haas et al. (2011a), suggest that the original, thin stellar disk dynamically evolved to the currently observed configuration through differential precession due to the surrounding circumnuclear disk. The effects of the CND will be most pronounced at the outermost portions of the stellar disk, erasing any observable disk-like structure at large radii while leaving the innermost orbits untouched. This is qualitatively consistent with the observations reported here, although we must caution that improved kinematic measurements at large radii are needed to make a more quantitative comparison with this scenario.

Without constraints from accelerations, the line-of-sight distance can only be estimated by assuming a star orbits in a particular plane. For candidate disk members of the clockwise disk, this is a reasonable assumption to make in order to describe the properties of the disk. Paumard et al. (2006) found evidence for both a CW and CCW disk, and estimated eccentricities by assuming the stars belonged to one of these disks. They found highly eccentric orbits for stars at larger radii that were on the CCW disk. However, we argue that a CCW disk does not exist and by selecting orbital solutions that place a star on the proposed

CCW disk can give arbitrarily high eccentricities. Indeed, such high eccentricities have proven difficult to explain dynamically (Cuadra et al., 2008; Löckmann & Baumgardt, 2009). As the current data for stars at large radii are less precise than for those at smaller radii, it is not possible at this time to constrain the eccentricities of stars that are not members of the CW disk. Obtaining more imaging data to increase the time baseline of the proper motion measurements as well as improved radial velocity measurements is important for constraining the orbits of stars at these large distances.

3.8 Conclusions

We have analyzed the orbits of 116 young stars in the Galactic center between projected radii $R = 0\farcs8$ - $13''$ ($\sim$0.032 pc - 0.52 pc). Our acceleration uncertainties are, on average, 10 μas yr^{-2} and are a factor of six smaller than in our previous efforts (Lu et al., 2009). We have detected six reliable acceleration measurements outside the central arcsecond and out to $1\farcs5$ ($\sim$0.06 pc), which provides the stars' line-of-sight distances and enables precise orbital parameter estimates. We confirm the existence of the clockwise disk, which has an orbital plane oriented at $(i, \Omega) = (130.2^\circ, 96.3^\circ)$. Based on our simulations, the level of contamination in our disk membership analysis is $\sim$50%. Thus, the number of stars in the disk may be as low as $\sim$30 stars out of our sample of 116. The previously-claimed counterclockwise disk is not detected, despite the fact that we use higher precision astrometric measurements and a larger field of view than in Lu et al. (2009) and Bartko et al. (2009). We find that the clockwise disk has an opening angle of $\sim$15° and the direction of its orbital plane does not change as a function of radius. A bias in the orbital solutions of disk stars near the line of nodes was discovered and leads to an apparent warp in the main clockwise disk. The

eccentricity distribution of the candidate members of the clockwise disk is $< e > \sim 0.3$. Given the recent finding by Lu et al. (in prep.) regarding the initial mass function and the age of the population, which is consistent with earlier work by Paumard et al. (2006), the eccentricities of the disk stars can be explained by dynamical relaxation in an initially circular disk.

Constraining the stars' line-of-sight distances through precise acceleration measurements is key for estimating stellar orbits and removes the need for prior assumptions that may lead to significant biases. Thus, it is critical to increase both the precision and the time baseline of astrometric measurements for stars at large radii from the SMBH. Astrometric measurements of the Galactic center are currently limited by knowledge of the point spread function, which has been assumed to be constant across the image. However, both instrumental and anisoplanatic effects lead to a spatially- and temporally-variable PSF. Accurate modeling of both the instrumental and time-variable PSF using atmospheric profiler data will allow for an improved optical distortion model and a more stable astrometric reference frame. This will be particularly important for orbital parameter estimates of stars at large radii ($R > 6''$), which have higher measurement uncertainties and are predominantly part of the off-disk population.

3.9 Appendix A: Improved Speckle Camera (NIRC) Distortion Solution

The AO images that have new corrections for geometric optical distortion and DAR (Yelda et al., 2010) allow for an improvement in the determination of the geometric optical distortion for the speckle camera (NIRC; Matthews et al., 1996). We use a similar approach to that described in Lu et al. (2009), but here we

Table 3.5. Updated NIRC Reimager Distortion Coefficients

i	$X(a_i)$	$Y(b_i)$
0	1.2972×10^{-2}	-2.1134×10^{-2}
1	9.9726×10^{-1}	-1.1145×10^{-3}
2	-2.2849×10^{-3}	1.0034

map the speckle data to the predicted star list for the 2004 July AO epoch (Appendix 3.11) as opposed to the measured star positions. We note that DAR was inadvertently not corrected in the speckle images. However, over the 5" speckle field of view, DAR amounts to ∼2 mas, in the extreme, and ∼1 mas on average, and is somewhat reduced when the frames are averaged together because the field rotates on the detector throughout the speckle observations (in contrast to the AO observations, which are taken at a fixed position angle). This new solution, given in Table 3.5, results in smaller residuals compared to our earlier solution (2 mas vs. 3 mas, on average).

3.10 Appendix B: Residual Relative Astrometric Error

The inaccuracies in the estimates of the PSF wings lead to an additional source of error that is not accounted for in the estimate of the centroiding error. Following the approach introduced by our group in Clarkson et al. (2012), we include an "additive" noise term for each observational approach. For the AO data, images taken in a consistent setup (N=11 observations at the time of this analysis) to the 2006 June image were aligned. Once in a common reference frame, lines were fit to the positions as a function of time, where the positional uncertainties included the error on the mean from the three subset images for each epoch (σ_{rms}; see §3.3.2) and the alignment errors (σ_{aln}), which were determined by

a half-sample bootstrap (Ghez et al., 2008). Confusion was accounted for, as described in Section 3.3.2.2. Only stars detected in all 11 epochs were used in this analysis. The velocity χ^2 distribution for 1024 stars was then compared to the expected distribution for 9 degrees of freedom (11 measurements - 2 fit parameters). We determined the amount of error to be added to the positional uncertainties in order to minimize, in a least squares sense, the difference between the distributions. This additive noise term for the AO data is $\sigma_{add} = 0.1$ mas, comparable to the centroiding error of bright stars ($K < 15$).

The additive error for the speckle data was determined in a similar fashion, but we aligned all speckle and LGSAO data together and used the 2006 June image as the reference epoch. A line was to the speckle positions as a function of time, where again, the positional uncertainties included σ_{rms} and σ_{aln}. Only stars that were detected in all 27 speckle images and that were not confused in any epoch were included in this analysis. In comparing the resulting χ^2 distribution for 32 stars to that expected for 25 degrees of freedom (27 speckle measurements - 2 fit parameters), a relatively small error (compared to σ_{rms} for speckle measurments, $\sim$1 mas for $K < 15$) of 0.18 mas is necessary to fully account for the positional scatter over time.

3.11 Appendix C: Local Distortion Correction

Of the 19 Galactic center adaptive optics data sets taken at Keck since 2004, all but three have had identical observational setups (e.g., PA=0 in the K' band). We began observing with a consistent setup (PA=0° and same telescope pointings) in 2006 May and therefore refer to this as the "2006-setup". The 2004 July image was taken at PA=200, while the 2005 July image was observed at PA=190. In 2005 June, we observed the GC at PA=0 but at a different starting position than

the 2006-setup (see Ghez et al., 2008; Lu et al., 2009). In Yelda et al. (2010), we found that a data set observed at a non-zero PA can be transformed to the PA=0 (2006-setup) image to ∼0.1 pix. To minimize the impact of this residual distortion when aligning the full GC data set, we applied a local distortion correction to the three images taken in different setups.

The local distortion correction was found by comparing the positions of the stars from the non-2006 epochs to their positions as predicted by their best-fit proper motions. This was done through the following series of steps. First, the 2006-setup star lists (taken through 2010) were transformed to the 2006 June epoch using a 2nd order polynomial. This epoch was chosen as the reference epoch as it is one of our highest quality images and is also the reference frame used in our main analysis (§3.3.2). The additive error term of 0.1 mas for AO data derived in Appendix 3.10 was included in the error measurements in these lists. Once the positions were placed in a common reference frame, proper motions were estimated by fitting a line to the positions as a function of time. Stars with proper motion errors >1.5 mas yr^{-1} or proper motions >10 mas yr^{-1} were excluded from this analysis, as they may be mis-matched sources. Based on these proper motions, we created "predicted" star lists for each of the three non-2006-setup epochs.

We next transformed all of the AO data (through 2010), including the three epochs that were taken with a different setup, to the 2006 June image. The transformed stellar positions for the three non-2006-setups were then compared to their predicted positions based on the previous step. The differences in these positions represents the residual distortion in the images. The positional differences measured over the detector for each non-2006 epoch were smoothed into a local distortion map in the following way. For each pixel on the detector, the

median positional difference of the 5 nearest stars was taken as the correction for that pixel. We note that the two data sets taken at a non-zero PA did not overlap completely with the 2006 June field, and we assigned the pixels with no overlap a value of zero. Similarly, we made a local distortion error map by taking the standard deviation of the positional differences for the 5 nearest neighbors to each pixel.

We verified that this method reduced the residuals in the the transformation of the PA=200 to PA=0 images from 2004 July. We applied this local distortion correction to the positions in the star lists created by *StarFinder* (Diolaiti et al., 2000), and added the local distortion error in quadrature to the centroiding errors for the three non-2006 epochs.

CHAPTER 4

Conclusions

A substantial leap forward in our understanding of the Galactic center has been made with the advent of laser guide star adaptive optics, which has allowed for 1) the spectroscopic identification of early- versus late-type stars, 2) micro-arcsecond astrometric precision, 3) relatively large field of view observations, with the ability to mosaic, and 4) the detection of stars 4 magnitudes fainter than in previous speckle observations. With these data, we have the ability to estimate the motions and in many cases, the orbits of individual stars throughout the central parsec, measurements that can help constrain theories of star formation and stellar dynamics in the hostile environment of a supermassive black hole.

With the sub-milliarcsecond astrometric precision provided by the Keck adaptive optics system, systematic sources of error that were once unrecognized in speckle imaging must now be considered. Two sources addressed in this thesis that were limiting Galactic center astrometry are differential atmospheric refraction and geometric optical distortion. After accounting for these effects, an improved Galactic center astrometric reference frame was established with Sgr A*-radio at rest to within 0.6 mas and 0.1 mas yr^{-1} in position and velocity space, respectively. The stability of the GC reference frame is critical for detecting post-Newtonian effects on stellar orbits, in particular the prograde relativistic precession. Further improvements in the stability of the reference frame are expected with 1) more infrared and radio observations of the central parsec's SiO masers

with time, and 2) better modelling of the spatially- and temporally-dependent PSF, which will in turn improve the optical distortion solution.

With a 16-year baseline of high resolution imaging, the plane-of-the-sky velocities and accelerations of the young stars within a Galactocentric radius of $R = 6''$ ($\sim$0.24 pc) are measured with a precision of 0.03 mas yr^{-1} ($\sim$1.2 km s^{-1}) and 10 μas yr^{-2} ($\sim$0.4 km s^{-1} yr^{-1}), respectively. These measurements match, and for many stars, exceed the highest astrometric precision of the young stars to date (Gillessen et al., 2009b). These data, combined with wide-field mosaicked AO images and spectroscopy, have allowed for precise orbital parameter estimates of 116 young stars throughout the central parsec. We confirm the existence of the clockwise stellar disk and find that less than half of the population has orbits that are consistent with this common plane. We do not detect any significant features in the counterclockwise direction, which is in agreement with Lu et al. (2009) and contrary to previous claims by others (Genzel et al., 2003; Paumard et al., 2006; Bartko et al., 2009), despite the fact that we include stars at large radii where the CCW disk was reported to exist. The off-disk population's orbital planes are randomly-distributed, and it is plausible that these stars were originally members of the CW disk and were scattered by a massive perturber. While the CW disk's thickness is $\sim$15.2°, the orientation of its orbital plane does not change with radius. In fact, a bias in the orbital solutions stemming from the lack of line-of-sight distance information was identified as a reason for previous claims of a warped disk (Bartko et al., 2009). The eccentricity distribution of the candidate members of the disk is $< e > \sim 0.3$. Given the recent finding by Lu et al. (in prep.) regarding the initial mass function and the age of the population, which is consistent with earlier work by Paumard et al. (2006), the eccentricities of the disk stars can be explained by dynamical relaxation in an initially circular disk.

Improvements in our knowledge about the formation and dynamical evolution of the young stars can be made through increased astrometric precision, especially for stars at relatively large radii. As shown in this thesis, the detection of accelerations in the plane of the sky is critical for constraining the line-of-sight distances and removes the need to make *a priori* assumptions that can lead to biases, as shown with various simulations in this thesis. Without constraints on the line-of-sight distances through accelerations, one must fully understand the impact that the prior assumptions have on the results. Future directions for improving astrometric precision, which will in turn lead to more acceleration measurements, include better modeling of the spatially- and temporally-variable point spread function in Galactic center images. A more accurate PSF model will allow for an improved optical distortion solution, which has the biggest impact on positional measurements of stars at large Galactocentric radii, where we currently have no acceleration information.

Much of the observational and theoretical focus over the last decade has been on the central parsec of the Galaxy. Systematic searches for young stars throughout the central few parsecs are critical for fully understanding how star formation proceeds in the vicinity of a supermassive black hole. Such a survey is currently underway by Nishiyama et al. (in prep.), who have found >60 candidate young stars out to $R \sim 2.5$ pc. If confirmed, this may challenge existing theories of star formation at the Galactic center. Ultimately, our understanding of the stellar processes in the Galactic center will shed light on the workings of other galactic nuclei containing young star clusters, such as M31 (Bender et al., 2005).

Bibliography

Alexander, R. D., Begelman, M. C., & Armitage, P. J. 2007, ApJ, 654, 907

Alexander, T. 2007, ArXiv e-prints

Allen, D. A., Hyland, A. R., & Hillier, D. J. 1990, MNRAS, 244, 706

Anderson, J. 2005, in The 2005 HST Calibration Workshop Proceedings, ed. A. Koekemoer, P. Goudfrooij, & L. L. Dressel, 11–20

Anderson, J. 2007, Variation of the Distortion Solution, Tech. rep.

Anderson, J., & King, I. R. 2006, PSFs, Photometry, and Astronomy for the ACS/WFC, Tech. rep.

Anderson, J., Sarajedini, A., Bedin, L. R., King, I. R., Piotto, G., Reid, I. N., Siegel, M., Majewski, S. R., Paust, N. E. Q., Aparicio, A., Milone, A. P., Chaboyer, B., & Rosenberg, A. 2008, AJ, 135, 2055

Anderson, J., & van der Marel, R. P. 2010, ApJ, 710, 1032

Bartko, H., Martins, F., Fritz, T. K., Genzel, R., Levin, Y., Perets, H. B., Paumard, T., Nayakshin, S., Gerhard, O., Alexander, T., Dodds-Eden, K., Eisenhauer, F., Gillessen, S., Mascetti, L., Ott, T., Perrin, G., Pfuhl, O., Reid, M. J., Rouan, D., Sternberg, A., & Trippe, S. 2009, ApJ, 697, 1741

Bartko, H., Martins, F., Trippe, S., Fritz, T. K., Genzel, R., Ott, T., Eisenhauer, F., Gillessen, S., Paumard, T., Alexander, T., Dodds-Eden, K., Gerhard, O., Levin, Y., Mascetti, L., Nayakshin, S., Perets, H. B., Perrin, G., Pfuhl, O., Reid, M. J., Rouan, D., Zilka, M., & Sternberg, A. 2010, ApJ, 708, 834

Beloborodov, A. M., Levin, Y., Eisenhauer, F., Genzel, R., Paumard, T., Gillessen, S., & Ott, T. 2006, ApJ, 648, 405

Bender, R., Kormendy, J., Bower, G., Green, R., Thomas, J., Danks, A. C., Gull, T., Hutchings, J. B., Joseph, C. L., Kaiser, M. E., Lauer, T. R., Nelson, C. H., Richstone, D., Weistrop, D., & Woodgate, B. 2005, ApJ, 631, 280

Berukoff, S. J., & Hansen, B. M. S. 2006, ApJ, 650, 901

Binney, J., & Tremaine, S. 2008, Galactic Dynamics: Second Edition (Princeton University Press)

Blum, R. D., Depoy, D. L., & Sellgren, K. 1995, ApJ, 441, 603

Bonnell, I. A., & Rice, W. K. M. 2008, Science, 321, 1060

Cameron, P. B., & Kulkarni, S. R. 2007, in Bulletin of the American Astronomical Society, Vol. 38, Bulletin of the American Astronomical Society, 996–+

Christopher, M. H., Scoville, N. Z., Stolovy, S. R., & Yun, M. S. 2005, ApJ, 622, 346

Clarkson, W. I., Ghez, A. M., Morris, M. R., Lu, J. R., Stolte, A., McCrady, N., Do, T., & Yelda, S. 2012, ApJ, 751, 132

Cuadra, J., Armitage, P. J., & Alexander, R. D. 2008, MNRAS, 388, L64

Dale, J. E., Davies, M. B., Church, R. P., & Freitag, M. 2009, MNRAS, 393, 1016

Davies, M. B., Blackwell, R., Bailey, V. C., & Sigurdsson, S. 1998, MNRAS, 301, 745

Davies, M. B., & King, A. 2005, ApJL, 624, L25

Dierckx, P. 1995, Curve and Surface Fitting with Splines (Oxford University Press)

Diolaiti, E., Bendinelli, O., Bonaccini, D., Close, L., Currie, D., & Parmeggiani, G. 2000, A&AS, 147, 335

Do, T., Ghez, A. M., Morris, M. R., Lu, J. R., Matthews, K., Yelda, S., & Larkin, J. 2009a, ApJ, 703, 1323

Do, T., Ghez, A. M., Morris, M. R., Yelda, S., Meyer, L., Lu, J. R., Hornstein, S. D., & Matthews, K. 2009b, ApJ, 691, 1021

Dupuy, T. J., Liu, M. C., & Ireland, M. J. 2008, ArXiv e-prints

Eckart, A., & Genzel, R. 1996, Nature, 383, 415

—. 1997, MNRAS, 284, 576

Eisenhauer, F., Genzel, R., Alexander, T., Abuter, R., Paumard, T., Ott, T., Gilbert, A., Gillessen, S., Horrobin, M., Trippe, S., Bonnet, H., Dumas, C., Hubin, N., Kaufer, A., Kissler-Patig, M., Monnet, G., Ströbele, S., Szeifert, T., Eckart, A., Schödel, R., & Zucker, S. 2005, ApJ, 628, 246

Eisenhauer, F., Schödel, R., Genzel, R., Ott, T., Tecza, M., Abuter, R., Eckart, A., & Alexander, T. 2003, ApJL, 597, L121

Figer, D. F. 2008, in IAU Symposium, Vol. 250, IAU Symposium, ed. F. Bresolin, P. A. Crowther, & J. Puls, 247–256

Figer, D. F., Gilmore, D., Kim, S. S., Morris, M., Becklin, E. E., McLean, I. S., Gilbert, A. M., Graham, J. R., Larkin, J. E., Levenson, N. A., & Teplitz, H. I. 2003, ApJ, 599, 1139

Fragile, P. C., & Mathews, G. J. 2000, ApJ, 542, 328

Fritz, T., Gillessen, S., Trippe, S., Ott, T., Bartko, H., Pfuhl, O., Dodds-Eden, K., Davies, R., Eisenhauer, F., & Genzel, R. 2010, MNRAS, 401, 1177

Fruchter, A. S., & Hook, R. N. 2002, PASP, 114, 144

Genzel, R., Eisenhauer, F., & Gillessen, S. 2010, Reviews of Modern Physics, 82, 3121

Genzel, R., Pichon, C., Eckart, A., Gerhard, O. E., & Ott, T. 2000, MNRAS, 317, 348

Genzel, R., Schödel, R., Ott, T., Eisenhauer, F., Hofmann, R., Lehnert, M., Eckart, A., Alexander, T., Sternberg, A., Lenzen, R., Clénet, Y., Lacombe, F., Rouan, D., Renzini, A., & Tacconi-Garman, L. E. 2003, ApJ, 594, 812

Genzel, R., Thatte, N., Krabbe, A., Kroker, H., & Tacconi-Garman, L. E. 1996, ApJ, 472, 153

Gerhard, O. 2001, ApJL, 546, L39

Ghez, A. M., Becklin, E., Duchjne, G., Hornstein, S., Morris, M., Salim, S., & Tanner, A. 2003, Astronomische Nachrichten Supplement, 324, 527

Ghez, A. M., Hornstein, S. D., Lu, J. R., Bouchez, A., Le Mignant, D., van Dam, M. A., Wizinowich, P., Matthews, K., Morris, M., Becklin, E. E., Campbell, R. D., Chin, J. C. Y., Hartman, S. K., Johansson, E. M., Lafon, R. E., Stomski, P. J., & Summers, D. M. 2005a, ApJ, 635, 1087

Ghez, A. M., Klein, B. L., Morris, M., & Becklin, E. E. 1998, ApJ, 509, 678

Ghez, A. M., Morris, M., Becklin, E. E., Tanner, A., & Kremenek, T. 2000, Nature, 407, 349

Ghez, A. M., Salim, S., Hornstein, S. D., Tanner, A., Lu, J. R., Morris, M., Becklin, E. E., & Duchêne, G. 2005b, ApJ, 620, 744

Ghez, A. M., Salim, S., Weinberg, N. N., Lu, J. R., Do, T., Dunn, J. K., Matthews, K., Morris, M. R., Yelda, S., Becklin, E. E., Kremenek, T., Milosavljevic, M., & Naiman, J. 2008, ApJ, 689, 1044

Gillessen, S., Eisenhauer, F., Fritz, T. K., Bartko, H., Dodds-Eden, K., Pfuhl, O., Ott, T., & Genzel, R. 2009a, ApJL, 707, L114

Gillessen, S., Eisenhauer, F., Trippe, S., Alexander, T., Genzel, R., Martins, F., & Ott, T. 2009b, ApJ, 692, 1075

Goodman, J. 2003, MNRAS, 339, 937

Górski, K. M., Hivon, E., Banday, A. J., Wandelt, B. D., Hansen, F. K., Reinecke, M., & Bartelmann, M. 2005, ApJ, 622, 759

Gubler, J., & Tytler, D. 1998, PASP, 110, 738

Gürkan, M. A., & Rasio, F. A. 2005, ApJ, 628, 236

Haas, J., Šubr, L., & Kroupa, P. 2011a, MNRAS, 412, 1905

Haas, J., Šubr, L., & Vokrouhlický, D. 2011b, MNRAS, 416, 1023

Hansen, B. M. S., & Milosavljević, M. 2003, ApJL, 593, L77

Hays, W. L. 1994, Statistics (Harcourt Brace College Publishers)

Hobbs, A., & Nayakshin, S. 2009, MNRAS, 394, 191

Hopman, C., & Alexander, T. 2006, ApJ, 645, 1152

Hornstein, S. D. 2007, PhD thesis, University of California, Los Angeles

Jackson, J. M., Geis, N., Genzel, R., Harris, A. I., Madden, S., Poglitsch, A., Stacey, G. J., & Townes, C. H. 1993, ApJ, 402, 173

Jaroszyński, M. 1998, Acta Astronomica, 48, 413

—. 1999, ApJ, 521, 591

Kim, S. S., Figer, D. F., & Morris, M. 2004, ApJL, 607, L123

Kolykhalov, P. I., & Syunyaev, R. A. 1980, Soviet Astronomy Letters, 6, 357

Konopacky, Q. M., Ghez, A. M., Duchêne, G., McCabe, C., & Macintosh, B. A. 2007, AJ, 133, 2008

Krabbe, A., Genzel, R., Drapatz, S., & Rotaciuc, V. 1991, ApJL, 382, L19

Krabbe, A., Genzel, R., Eckart, A., Najarro, F., Lutz, D., Cameron, M., Kroker, H., Tacconi-Garman, L. E., Thatte, N., Weitzel, L., Drapatz, S., Geballe, T., Sternberg, A., & Kudritzki, R. 1995, ApJL, 447, L95+

Kraniotis, G. V. 2007, ArXiv e-prints

Larkin, J., Barczys, M., Krabbe, A., Adkins, S., Aliado, T., Amico, P., Brims, G., Campbell, R., Canfield, J., Gasaway, T., Honey, A., Iserlohe, C., Johnson, C., Kress, E., Lafreniere, D., Magnone, K., Magnone, N., McElwain, M., Moon, J., Quirrenbach, A., Skulason, G., Song, I., Spencer, M., Weiss, J., & Wright, S. 2006, New Astron. Rev., 50, 362

Lee, H. M. 1996, in IAU Symposium, Vol. 174, IAU Symposium, ed. P. Hut & J. Makino, 293

Levin, Y. 2007, MNRAS, 374, 515

Levin, Y., & Beloborodov, A. M. 2003, ApJL, 590, L33

Li, J., An, T., Shen, Z., & Miyazaki, A. 2010, ApJL, 720, L56

Lin, D. N. C., & Pringle, J. E. 1987, MNRAS, 225, 607

Liu, M. C., Dupuy, T. J., & Ireland, M. J. 2008, ApJ, 689, 436

Löckmann, U., & Baumgardt, H. 2009, MNRAS, 394, 1841

Löckmann, U., Baumgardt, H., & Kroupa, P. 2009, MNRAS, 398, 429

Lu, J. R. 2008, PhD thesis, University of California, Los Angeles

Lu, J. R., Ghez, A. M., Hornstein, S. D., Morris, M., & Becklin, E. E. 2005, ApJL, 625, L51

Lu, J. R., Ghez, A. M., Hornstein, S. D., Morris, M. R., Becklin, E. E., & Matthews, K. 2009, ApJ, 690, 1463

Madigan, A., Levin, Y., & Hopman, C. 2009, ApJL, 697, L44

Mapelli, M., Hayfield, T., Mayer, L., & Wadsley, J. 2008, ArXiv e-prints

—. 2012, ApJ, 749, 168

Marois, C., Macintosh, B., Barman, T., Zuckerman, B., Song, I., Patience, J., Lafrenière, D., & Doyon, R. 2008, Science, 322, 1348

Martins, F., Gillessen, S., Eisenhauer, F., Genzel, R., Ott, T., & Trippe, S. 2008, ApJL, 672, L119

Matthews, K., Ghez, A. M., Weinberger, A. J., & Neugebauer, G. 1996, PASP, 108, 615

Matthews, K., & Soifer, B. T. 1994, Experimental Astronomy, 3, 77

Max, C. E., Canalizo, G., Macintosh, B. A., Raschke, L., Whysong, D., Antonucci, R., & Schneider, G. 2005, ApJ, 621, 738

Montero-Castaño, M., Herrnstein, R. M., & Ho, P. T. P. 2009, ApJ, 695, 1477

Morris, M. 1993, ApJ, 408, 496

Morris, M., & Serabyn, E. 1996, ARAA, 34, 645

Najarro, F., Krabbe, A., Genzel, R., Lutz, D., Kudritzki, R. P., & Hillier, D. J. 1997, AAP, 325, 700

Nayakshin, S. 2006, MNRAS, 372, 143

Nayakshin, S., & Sunyaev, R. 2005, MNRAS, 364, L23

Nucita, A. A., De Paolis, F., Ingrosso, G., Qadir, A., & Zakharov, A. F. 2007, PASP, 119, 349

Paumard, T., Genzel, R., Martins, F., Nayakshin, S., Beloborodov, A. M., Levin, Y., Trippe, S., Eisenhauer, F., Ott, T., Gillessen, S., Abuter, R., Cuadra, J., Alexander, T., & Sternberg, A. 2006, ApJ, 643, 1011

Perets, H. B., Gualandris, A., Kupi, G., Merritt, D., & Alexander, T. 2009, ApJ, 702, 884

Rafelski, M., Ghez, A. M., Hornstein, S. D., Lu, J. R., & Morris, M. 2007, ApJ, 659, 1241

Rauch, K. P., & Tremaine, S. 1996, New Astronomy, 1, 149

Reid, M. J., & Brunthaler, A. 2004, ApJ, 616, 872

Reid, M. J., Menten, K. M., Genzel, R., Ott, T., Schödel, R., & Eckart, A. 2003, ApJ, 587, 208

Reid, M. J., Menten, K. M., Trippe, S., Ott, T., & Genzel, R. 2007, ApJ, 659, 378

Rubilar, G. F., & Eckart, A. 2001, AAP, 374, 95

Sabha, N., Witzel, G., Eckart, A., Buchholz, R. M., Bremer, M., Gießübel, R., García-Marín, M., Kunneriath, D., Muzic, K., Schödel, R., Straubmeier, C., Zamaninasab, M., & Zernickel, A. 2010, AAP, 512, A2+

Salim, S., & Gould, A. 1999, ApJ, 523, 633

Sanders, R. H. 1992, Nature, 359, 131

—. 1998, MNRAS, 294, 35

Schödel, R., Merritt, D., & Eckart, A. 2009, AAP, 502, 91

Schödel, R., Ott, T., Genzel, R., Eckart, A., Mouawad, N., & Alexander, T. 2003, ApJ, 596, 1015

Schödel, R., Ott, T., Genzel, R., Hofmann, R., Lehnert, M., Eckart, A., Mouawad, N., Alexander, T., Reid, M. J., Lenzen, R., Hartung, M., Lacombe, F., Rouan, D., Gendron, E., Rousset, G., Lagrange, A.-M., Brandner, W., Ageorges, N., Lidman, C., Moorwood, A. F. M., Spyromilio, J., Hubin, N., & Menten, K. M. 2002, Nature, 419, 694

Shlosman, I., & Begelman, M. C. 1987, Nature, 329, 810

Stolte, A., Ghez, A. M., Morris, M., Lu, J. R., Brandner, W., & Matthews, K. 2008, ApJ, 675, 1278

Tamblyn, P., Rieke, G. H., Hanson, M. M., Close, L. M., McCarthy, Jr., D. W., & Rieke, M. J. 1996, ApJ, 456, 206

Trippe, S., Gillessen, S., Gerhard, O. E., Bartko, H., Fritz, T. K., Maness, H. L., Eisenhauer, F., Martins, F., Ott, T., Dodds-Eden, K., & Genzel, R. 2008, AAP, 492, 419

Šubr, L. ., Schovancová, J., & Kroupa, P. 2009, AAP, 496, 695

van der Marel, R. P., Anderson, J., Cox, C., Kozhurina-Platais, V., Lallo, M., & Nelan, E. 2007, Calibration of ACS/WFC Absolute Scale and Rotation for Use in creation of a JWST Astrometric Reference Field, Tech. rep.

Wardle, M., & Yusef-Zadeh, F. 2008, ApJL, 683, L37

Weinberg, N. N., Milosavljević, M., & Ghez, A. M. 2005, ApJ, 622, 878

Will, C. M. 2008, ApJL, 674, L25

Yelda, S., Lu, J. R., Ghez, A. M., Clarkson, W., Anderson, J., Do, T., & Matthews, K. 2010, ApJ, 725, 331

Yu, Q., Lu, Y., & Lin, D. N. C. 2007, ApJ, 666, 919

Yusef-Zadeh, F., & Wardle, M. 2008, in Astronomical Society of the Pacific Conference Series, Vol. 387, Massive Star Formation: Observations Confront Theory, ed. H. Beuther, H. Linz, & T. Henning, 361

Zucker, S., & Alexander, T. 2007, ApJL, 654, L83